DARK MATTER AND DARK ENERGY IN THE EARLY UNIVERSE

Carisa A. Miller

A dissertation submitted to the faculty of the University of North Carolina at Chapel Hill in partial fulfillment of the requirements for the degree of Doctor of Philosophy in the Department of Physics and Astronomy.

Chapel Hill
2020

Approved by:

Adrienne Erickcek

Jon Engel

Charles Evans

Sheila Kannappan

Jack Ng

ABSTRACT

Carisa A. Miller: Dark Matter and Dark Energy in the Early Universe
(Under the direction of Adrienne Erickcek)

Less than 5% of the current energy content of the Universe is contained in Standard Model (SM) particles; the remaining 95% is made up of dark matter and dark energy. Both dark matter and dark energy have only been detected through their gravitational interactions, and their properties require the introduction of new, beyond-SM physics. A promising regime to search for new physics is in high-energy environments like that of the Universe's first second. We investigate how a theory of modified gravity that aims to explain dark energy behaves in the early Universe and how the production method of dark matter in the early Universe could effect the formation of structure. The dark energy model we consider is chameleon gravity, in which a light scalar field that couples to the trace of the stress-energy tensor in such a way that its mass depends on the ambient density, and makes it difficult to detect in high-density environments. We consider a chameleon field with a quartic potential and show that the scale-free nature of this potential allows the chameleon to avoid the problems encountered by other chameleon theories during the Universe's first second. We then determine how producing dark matter particles with relativistic velocities via the decay of heavier particles impacts the dark matter velocity distribution function and the growth of structure. We find that the free streaming of these dark matter particles can prevent structure formation on subgalactic scales. Therefore, current observations of small-scale structure put an upper limit on the velocity of the dark matter particles at their creation. Finally, we investigate whether these limits can be relaxed in the presence of scattering interactions between the dark matter and SM particles.

TABLE OF CONTENTS

LIST OF FIGURES

LIST OF ABBREVIATIONS AND SYMBOLS

a	Scale factor
$\tilde{a}$	Jordan frame scale factor
a_*	Einstein frame scale factor
a_0	Scale factor today
a_D	Scale factor at a dark matter particle's production
a_i	Scale factor at time t_i
$a_{\rm RH}$	Scale factor at reheating
b	Number of dark matter particle produced per scalar decay
BBN	Big Bang Nucleosynthesis
c	Speed of Light
CDM	Cold Dark Matter
C.L.	Confidence Level
$\langle E \rangle$	Average energy per dark matter particle
EFT	Effective Field Theory
EMDE	Early Matter-Dominated Era
$F(x_1, x_2)$	Elliptic integral of the first kind
f	Fraction of scalar field energy transferred to dark matter
$f(x)$	Distribution function of variable x
G	Gravitational constant
g_*	Chapter 2: Determinant of the metric $g^*_{\mu\nu}$
$g_*(T)$	Number of relativistic degrees of freedom at temperature T
$g_{*S}(T)$	Number of relativistic degrees of freedom in the entropy density at temperature T
$g^*_{\mu\nu}$	Metric that solve the Einstein equations
$\tilde{g}_{\mu\nu}$	Metric that governs geodesic motion
H	Hubble Parameter
H_*	Einstein frame Hubble Parameter
h	Hubble fudge factor: $H(a_0) = 100h$ km/s/Mpc
$\hbar$	Reduced Planck constant

K	Kinetic energy of the chameleon field
k	Chapter 2: Comoving wavenumber of a chameleon field plane-wave perturbation
k	Chapter 3&4: Comoving wavenumber of a perturbation mode with length λ
k_B	Boltzmann constant
$k_{\rm fs}$	Comoving free-streaming wavenumber (with $a = 1$ today)
$k_{\rm hm}$	Half-mode scale
$k_{\rm phys}$	Physical wavenumber of a chameleon field plane-wave perturbation
M	Mass scale of a chameleon runaway potential
$M_\odot$	Solar mass
m	Mass
MCMC	Markov Chain Monte Carlo
$M_{\rm hm}$	Half-mode mass
$M_{\rm Pl}$	Planck mass
MW	Milky Way
m_χ	Dark matter mass
n	An integer
nCDM	nonCold Dark Matter
$N_{\rm eff}$	Effective number of neutrinos
n_k	Occupation number
$\hat{n}_\phi$	Comoving number density of ϕ particles
$\hat{n}_\chi$	Comoving number density of dark matter particles
P	Pressure
P_*	Einstein frame pressure
$P(k)$	Matter Power Spectrum
p	Chapter 2: $p \equiv \ln(a_*/a_{*,i})$
p	Chapter 3&4: Momentum
$p^{\rm akd}$	Dark matter particle momentum long after kinetic decoupling
$p_{\rm f}$	"Floor" of the dark matter momentum
$P_{\rm CDM}$	Matter Power Spectrum in the standard CDM scenario

$P_{\rm nCDM}$	Matter Power Spectrum in a scenario with non-cold dark matter
q	Comoving momentum scaled by the comoving momentum of a typical dark matter particle
QCD	Quantum Chromodynamics
R_*	Ricci Scalar
SM	Standard Model
T	Radiation temperature
t	Proper time
$T_{\rm eq}$	Temperature at matter-radiation equality
t_i	Initial proper time
T_J	Jordan frame radiation temperature
$T_{\rm kd}$	Kinetic decoupling temperature
$T_{\rm RH}$	Reheat temperature
$T_{*}^{\mu}{}_{\nu}$	Stress Energy Tensor in the Einstein frame
$\tilde{T}^{\mu}{}_{\nu}$	Stress Energy Tensor in the Jordan frame
T_ν	Neutrino temperature
T_χ	Dark matter temperature
$T^2(k)$	Transfer function
$V(\phi)$	Potential of the chameleon field
v	Velocity
v_D	Velocity imparted to a dark matter particle at its production
$V_{\rm eff}$	Effective potential
w	Equation of state parameter
WDM	Warm Dark Matter
w_χ	Dark matter equation of state parameter
X	$\gamma_D v_D$
Y	$(\gamma_D v_D a_D)^2$
z	Redshift
α	Fitting parameter for the dark matter transfer function
β	Chapter 2: Chameleon coupling constant

β	Chapter 3&4: Fitting parameter for the dark matter transfer function
Γ_ϕ	Scalar field decay rate
γ	Fitting parameter for the dark matter transfer function
γ	Lorentz factor
γ_D	Lorentz factor of velocity v_D
$\delta\phi$	Perturbation to the chameleon field
ε	Fraction of dark matter particles
κ	Chameleon self-interaction constant
λ	Comoving wavelength
ΛCDM	Λ Cold Dark Matter
$\lambda_{\rm fs}$	Comoving free-streaming length
$\lambda_{\rm fs,0}^{\rm phys}$	Physical free-streaming length today
$\lambda_{\rm hor}$	Horizon size
μ	$\gamma_D v_D a_{\rm RH}/a_0$
π	Delicious
ρ	Energy density
$\tilde{\rho}$	Jordan frame energy density
ρ_*	Einstein frame energy density
$\rho_{\rm crit}$	Critical energy density
ρ_k	Energy density in perturbations
ρ_r	Radiation energy density
ρ_ϕ	Scalar field energy density (chameleon or otherwise)
ρ_χ	Dark matter energy density
Σ	Chapter 2: The kick function
Σ	Chapter 4: Momentum transfer rate
σ	Initial momentum transfer rate
$\langle\sigma_{\rm an}v\rangle$	Dark matter velocity-averaged annihilation cross section
$\langle\sigma_{\rm sc}v\rangle$	Dark matter velocity-averaged scattering cross section
τ	Conformal time

ϕ	Scalar field (chameleon or otherwise)
φ	Dimensionless chameleon field: $\phi/M_{\rm Pl}$
χ	Dark matter particle
$\Omega_{\rm DM}$	Fraction of the critical density in dark matter
ω_k	Effective mass of a chameleon field plane-wave perturbation

CHAPTER 1
Introduction

Two of the most pursued questions in cosmology are the nature and composition of what we appropriately call dark energy and dark matter. Dark energy is the term for the force that drives the current accelerated expansion of the Universe and makes up $68.89 \pm 0.56\%$ (68% C.L.) of the total energy density today [1]. Dark matter accounts for a remaining $26.07 \pm 0.53\%$ [1] and thus far has only been detected only by its gravitational interactions. The first definitive evidence that our Universe was not only expanding, but expanding at an accelerated rate, was provided by observations of Type Ia supernovae [2, 3]. More recently, observations of baryon acoustic oscillations and clustering in large scale structure provide another measurement of the current expansion rate [4]. The original evidence for dark matter came from the discrepancies in observations of dynamical and luminous mass of galaxies and clusters; the mass inferred from observed motion was much larger than the mass accounted for by luminous objects. The use of the term "dark matter" is attributed to Fritz Zwicky who estimated the mass of the Coma cluster using the radial velocity of galaxies within the cluster, and found it to be much larger than the mass inferred from the number and brightness of the galaxies, leading him to conclude the presence of additional, nonluminous matter [5]. Further evidence came when Vera Rubin and collaborators used spectrography to measure, in M31, the radial velocities of stars and gas at varying distance from the galactic center and found a flat rotation curve implying the presence of additional mass [6]. The presence of dark matter has also been inferred by using gravitational lensing to obtain the mass of clusters, rather than dynamical motion [7]. Dark matter is also necessary to explain the observed structure growth from measurements of anisotropies in the Cosmic Microwave Background (CMB) [8, 9].

In order to explain the Universe's current phase of accelerated expansion using general relativity, one must consider an additional energy component having a negative pressure so that its energy density remains nearly constant as the Universe expands. Conforming with other cosmological observations, however, requires this constant value of the energy density to be extremely small, $\rho_\Lambda = 2.5 \times 10^{-47}$ GeV^4 $\sim 10^{-123} M_{\rm Pl}^4$ (in natural units, where $M_{\rm Pl}$ is the Planck mass)[1]. While QFT predicts the existence of a vacuum energy, one would expect the value of the energy density to be $\sim M_{\rm Pl}^4$; this is the cosmological constant problem.

Alternatively, one can introduce new physics by introducing a new scalar field or by modifying general relativity. Popular modifications to gravity often take the form of $f(R)$-theories in which the Einstein-Hilbert action becomes a general function of the Ricci scalar R [10, 11, 12], and/or scalar-tensor theories in which there is an additional scalar field which couples non-minimally to the curvature [13]. The simple inclusion of an uncoupled scalar field can also give rise to cosmic acceleration if the field is presently confined to a near constant energy value, $e.g.$ by evolving along a flat region of its potential [14].

Beyond being nonluminous, evidence of dark matter further indicates that it is a type of matter entirely apart from baryons and leptons. Prior to recombination, baryons[1] and photons remain in a tightly coupled plasma. This plasma will initially infall into overdense regions in the early Universe, but as the density increases, radiation pressure builds until the plasma is forced outward. After the plasma is ejected from the overdense region, the radiation pressure decreases, and the infall begins again. This oscillatory motion is imprinted in the anisotropies of the Cosmic Microwave Background(CMB). In contract, dark matter does not interact with baryons or photons, and continues to accumulate in overdense regions. From the comparative amplitude of the first infall and first rebound, the contribution of both baryonic and nonbaryonic matter to the total energy density can be calculated. It is from this that we know that $4.90 \pm 0.09\%$ of the energy density in our Universe is baryonic matter, while another $26.07 \pm 0.53\%$ is nonbaryonic, dark matter [1]. Further confirmation of such a small fraction of ordinary baryonic matter comes from the abundances of light elements predicted by Big Bang Nucleosynthesis (BBN) [15, 16]. The CMB also eliminates neutrinos as a significant component of the dark matter, as neutrinos are relativistic at the time of recombination and are able to freely stream from overdense regions. Thus, we are again required to look to new physics beyond the SM in order to adequately explain cosmological observations.

The variety of theories and models invoked to explain dark matter and dark energy is extensive, and in this work we present our explorations of single, well-motivated scenarios within each subject. The nature of dark matter and dark energy are both highly pursued questions, and thus far investigations into each have communicated the clear need for new, undiscovered physics, likely at energy scales not yet probed by experiments. Such energy scales are reached in the high temperatures of the early Universe, and our explorations use this period as a theoretical laboratory to study dark matter and dark energy.

[1]Throughout this work we will define baryons to include not only protons and neutrons, but electrons as well, despite the fact that they are leptons.

To start these explorations we first lay down the basic cosmological framework that we will be considering. A Universe that is homogeneous, isotropic, and expanding can be most generally described by the Friedmann-Lemaître-Robertson-Walker space-time metric:

$$ds^2 = -dt^2 + a^2(t)dx^2. \tag{1.1}$$

The expansion is characterized by $a(t)$, a dimensionless scale factor that increases with time, t. If we consider two stationary objects in an expanding cosmology as two fixed points on an expanding grid, the distance between the two can be described by the differences in their coordinates, which is fixed, or by the measured distance between them, which increases as the grid size increases. We refer to these distances as the comoving and physical distances, respectively, and they can be related at a given time by $d_{\rm phys} = a(t)d_{\rm comov}$. Clearly, the comoving and physical distance are equal when the scale factor equals 1, and, while it is standard to define today, t_0, as the point at which $a_0 = a(t_0) = 1$, it is an arbitrary choice and we will often choose to set $a = 1$ at another time through out this work. The rate at which the scale factor changes with time is known as the Hubble rate:

$$H(t) \equiv \frac{da/dt}{a} = \frac{\dot{a}}{a} \tag{1.2}$$

If we assume the energy content of the Universe can be described by a perfect fluid which energy density ρ and pressure P, then, in a flat space-time, the Einstein field equations give us the first and second Friedmann equations, which govern cosmological dynamics:

$$H^2 = \frac{8\pi G}{3}\rho, \tag{1.3}$$

$$\frac{\ddot{a}}{a} = -\frac{4\pi G}{3}(\rho + 3P). \tag{1.4}$$

Using the above equations one can derive the equation for energy conservation for a perfect fluid in an expanding Universe:

$$\frac{d\rho}{dt} = -3H(\rho + P), \tag{1.5}$$

which can be rewritten using the equation of state parameter, $w \equiv P/\rho$, as

$$\rho = \rho(t_0)a^{-3(1+w)}. \tag{1.6}$$

Thus we can see that for matter and other pressureless ($w = 0$) fluids, their energy density decreases with time according to $\rho \propto a^{-3}$, and we say the energy density "redshifts away" as a^{-3}. For radiation, the equation of state parameter is $w = 1/3$ and so $\rho \propto a^{-4}$.

If a substance has a negative pressure and an equation of state $w < -1/3$, then, according to the second Friedmann equation (Eq. 1.4), $\ddot{a}$ is positive and the expansion rate is accelerating if this substance is the dominant energy competent of the Universe. If the equation of state is $w = -1$ then ρ is constant and the energy density of such a substance is not diluted by the expansion of the Universe. Current observations provide bounds on the present value of the dark energy equation of state parameter: $w = -1.03 \pm 0.03$ [1, 17]. One such substance that could exhibit this behavior is a scalar field dominated by its potential energy. The total energy density of a scalar field, ϕ, is given by the sum of its kinetic and potential energies $\rho = K + V$, whereas its pressure can be given by $P = K - V$, and the equation of state for a potential-dominated field is $w \simeq -1$. Allowing the field's potential energy to dominate often requires these scalar fields to be light, $m < H$

While many explanations for the current accelerated expansion of the Universe posit the existence of a new light scalar field, these fields are usually coupled to matter and so can mediate long-range forces, often of gravitational strength. Not only are scalar fields, such as these, cosmologically motivated, but they are also pervasive in high-energy physics and string theory. However, stringent experimental bounds imply tight constraints on any new fifth forces mediated by scalar fields [18, 19, 20, 21, 22]. These constraints require the scalar's coupling to matter to be tuned to unnaturally small values in order to avoid detection. Another approach is to employ a screening mechanism, which suppresses effects of the field locally, allowing consistency with successful tests of general relativity.

One of the few known screening mechanisms capable of reconciling the predictions of scalar-tensor gravitational theories and experimental constraints is the chameleon mechanism [23, 24]. In chameleon gravity theories, the scalar field's potential function and its coupling to the stress-energy tensor sum into an effective potential (See Figure 1.1) whose shape and minimum is dependent on the matter density of its environment. Consequently, the effective mass of the chameleon field, which depends on the curvature of the

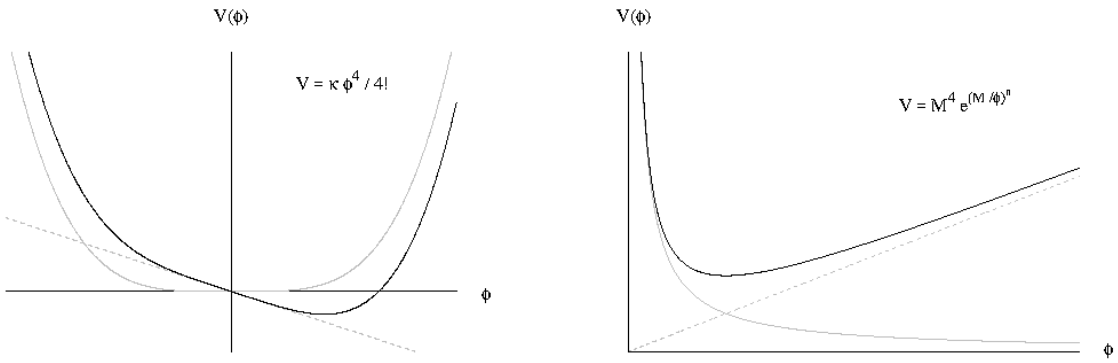

Figure 1.1: Depiction of how the chameleon potential (grey, solid) and its coupling to matter (grey, dotted) combine into an effective potential (black) in two models: the exponential (right) and quartic (left) potentials. The slope of the matter contribution becomes steeper in areas of higher density. In both potentials the minimum is pushed toward lower values of ϕ and the curvature around the minimum increases as density increases.

potential around its minimum,

$$m^2 = \left.\frac{d^2V}{d\phi^2}\right|_{\phi=\phi_{\rm min}}, \tag{1.7}$$

is also dependent on the environment, increasing enough in regions of high density to suppress the field's ability to mediate a long-range force. Because of this ability to hide within its environment, the chameleon can couple to matter with gravitational strength and still evade experimental detection in laboratory and Solar System tests of gravity.

The vast majority of cosmological investigations of chameleon gravity have considered potentials of the runaway form, such as the exponential $V(\phi) = M^4 \exp[(M/\phi)^n]$ and power-law $V(\phi) = M^{4+n}\phi^{-n}$ potentials. In order to evade Solar System tests of gravity, M has to be set to a value of $\sim 10^{-3}$ eV, which is the energy scale of dark energy [24]. This coincident energy scale gave the chameleon a lot of attention early on as a possible explanation for cosmic acceleration. However, it was shown in Ref. [25] that the chameleon field cannot account for the accelerated expansion of the Universe without including a constant term in its potential. Nevertheless, light scalar fields arise in many theories that consider physics beyond the Standard Model (SM), and the chameleon mechanism remains one of the most-studied approaches to screening the unwanted forces mediated by these fields.

Many laboratory experiments have been conducted to search for forces mediated by chameleon fields. Experiments that use atom [26] and neutron [27, 28] interferometry and those that use μm-sized test masses

[29] have already placed constraints on chameleon theories. Additional experiments have been proposed: one aims to measure the interactions between parallel plates to search for new forces [30] and another suggests using atom interferometry between parallel plates of different densities to detect density-dependent chameleon forces [31]. Laboratory searches for chameleon particles converted from photons in the presence of a magnetic field via the Primakov effect have placed constraints on the chameleon-photon coupling [32, 33]. The CERN Axion Solar Telescope searched for chameleons created in the Sun by this effect [34] and is currently conducting more sensitive searches [35] to detect solar chameleons via their radiation pressure [36]. Chameleon theories have also been constrained by their effects on the pulsation rate of Cepheids [37] and comparisons of x-ray and weak-lensing profiles of galaxy clusters [38, 39]. There have also been efforts to constrain the parameters of chameleon models by their effects on the cosmic microwave background [40, 41], though these analyses focus specifically on potentials of the power-law form. Given the tremendous experimental effort under way to detect or constrain chameleons, it is troubling that the most widely studied chameleon models have been shown to suffer a breakdown in calculability in the early Universe due to the discrepancy between the chameleon mass scale and that of the SM particles [42, 43].

In Chapter 2, we aim to identify a chameleon potential that can avoid the computational breakdown suffered by runaway models. We analyze a class of potential not often considered in chameleon theories: the quartic potential, $V(\phi) = \kappa\phi^4/4!$. Prevalent in high-energy theories, the quartic potential is also viable as a chameleon model because the self-interaction of this potential is sufficient to ensure that the field will be adequately screened in high-density environments [44]. The scale-free property of the quartic model is potentially beneficial as it can avoid the hierarchy of energy scales that arises due to the low-energy scale of the runaway potentials, and we investigate whether it is able to remain well-behaved in the early Universe.[2]

Following our investigations in Chapter 2 into chameleon gravity, in Chapter 3 we turn our attention to dark matter. While we do not yet know the nature or composition of dark matter, our wealth of cosmological investigations allows us to put constraints on its origins. One of the most common origin stories for dark matter is to assume that it was once in thermal equilibrium with SM particles in the early Universe. As the SM plasma cooled, thermal production of dark matter ceased while annihilations continued. The dark matter abundance thus began decreasing with the expansion until its annihilation rate equaled the Hubble rate, at

[2]Another proposed way to avoid the detrimental effect of the kicks is to include DBI-inspired corrections to the chameleon's Lagrangian that weaken the chameleon's coupling to matter at high energies. This modification effectively introduces a second screening mechanism analogous to a Vainshtein screening in which derivative interactions weaken the effect of the kicks [45].

which point annihilations also ceased, and the dark matter abundance became constant. A second common assumption is that this process, what we call dark matter freeze-out, occurred during a period in which the energy density of the Universe was dominated by radiation. These assumptions allow one to calculate the annihilation rate that generates the currently observed dark matter abundance. The required annihilation cross section is "miraculously" of the electroweak scale [46]. However, as we continually place more stringent bounds on dark matter properties, while failing to receive signals from any direct [47, 48, 49] or indirect [50, 51, 52, 53, 54, 55] searches, interest in alternatives to this commonly considered scenario grows.

Alternatives to the common scenario often challenge the assumptions that dark matter was in thermal equilibrium with SM particles and that it froze out during an era of radiation domination, both of which, while tenable, are not strictly necessary. A period of radiation domination is required at temperatures below $\sim$3 MeV in order to be consistent with the successful predictions of light element abundances from BBN [56, 57, 58]. Inflation, however, is believed to occur at energy scales that greatly exceed this temperature, and the thermal history of the Universe between the two periods is entirely unconstrained. In the simplest scenario, the inflaton decays into relativistic particles that come to dominate the energy density of the Universe, and an era of radiation domination begins [59, 60]. The transition to a radiation-dominated era, known as reheating, is usually assumed to occur at temperatures many orders of magnitude above 3 MeV. It is not necessary, however, that this be the case - the reheating of the Universe can occur at any temperature between 3 MeV and the energy scale of inflation, and it can be caused by a number of different mechanisms.

In many models, inflation ends when the scalar field that drives inflation begins oscillating in its potential minimum before decaying. If these oscillations occur in a quadratic potential, the field behaves as pressureless fluid, and the Universe is effectively matter dominated [61]. Similar scenarios occur when one considers the scalar (moduli) fields that are a common component of string theories [62, 63, 64, 65, 66, 67, 68, 69]. These oscillating fields naturally come to dominate the energy density of the Universe following the decay of the inflaton, providing another viable mechanism to produce an effectively matter-dominated era. Hidden-sector theories, in which the dark matter does not couple directly to the SM, can also alter the thermal history [70, 71, 72, 73, 74, 75], providing yet another means to achieve a period of matter domination prior to BBN. Thus, an early matter-dominated era (EMDE) arises in many theories of the early Universe.

The occurrence of an EMDE can profoundly affect dark matter phenomenology, notably its resulting relic abundance [76, 77, 78, 79, 80, 81, 82, 83, 84, 85, 86, 87, 88, 89, 90, 91, 92]. The entropy generated by the decay of the dominant matter component during the EMDE dilutes the relic abundance of existing particles;

if dark matter thermally decoupled during the EMDE, a smaller annihilation cross section $\langle \sigma_{\rm an} v \rangle$ is required to compensate for this dilution and provide the observed dark matter abundance. Contrarily, if dark matter is a decay product of the dominating component, its abundance can be significantly enhanced, requiring a larger $\langle \sigma_{\rm an} v \rangle$ to compensate for the excess, a scenario already under pressure by γ-ray observations [93, 94]. The correct relic abundance can almost always be obtained with the appropriate combinations of $\langle \sigma_{\rm an} v \rangle$, dark matter branching ratio, and temperature at reheating [80, 81, 85, 90]. In many scenarios, the dominant production mechanism for dark matter is by decay, rather than thermal production.

Another interesting consequence of an EMDE is the growth of small-scale structure. Subhorizon density perturbations in dark matter grow linearly with the scale factor during an EMDE, as opposed to the much slower logarithmic growth experienced during a radiation-dominated era [95, 96, 97]. This linear growth can provide an enhancement to dark matter structure on extremely small scales ($\lambda \lesssim 30$ pc for temperature at reheating > 3 MeV), providing observable consequences to this scenario if dark matter is a cold thermal relic [97, 98, 99].

However, if the dark matter is relativistic at reheating, the perturbation modes that enter the horizon during the EMDE will be wiped out by the free streaming of dark matter particles [95, 96]. For this reason, Ref. [95] assumed that the dark matter particles were born from the decay process with nonrelativistic velocities or had a way of rapidly cooling in order for the enhancement to substructure to be preserved. Assuming a nonrelativistic initial velocity for the dark matter requires a small, finely tuned mass splitting between the parent and daughter particles, and it is more natural to assume any daughter particles are produced relativistically.

Reference [96] claimed that the large free-streaming length of dark matter produced relativistically from scalar decay would washout any enhancement to structure growth. However, Ref. [96] reached this conclusion by assuming that all dark matter particles were created at reheating, neglecting those particles created during the EMDE. The momenta of particles born prior to reheating decreased throughout the EMDE. Consequently, particles born earlier will be slower at reheating. In Chapter 3, we investigate the extent to which the redshifting of the particles' momenta affects their velocity distribution at reheating, focusing on the average particle velocity and the fraction of particles below a given velocity, to determine under what conditions the EMDE enhancement to structure growth can be preserved.

We further consider, in 3.3, under what conditions the free streaming of relativistically produced dark matter could suppress the structures we observe. The Lyman-α forest provides information on the matter

power spectrum at the smallest observable scales, $0.5\mathrm{Mpc}/h < \lambda < 20\mathrm{Mpc}/h$ [100, 101, 102] by measuring the line-of-sight distribution of hydrogen gas clouds through their absorption of $\mathrm{Lyman}-\alpha$ photons from distant quasars. The Milky Way's (MW) satellite galaxies also constrain the small-scale power spectrum [103]. Preventing the suppression of power at these scales provides us with constraints on the allowed dark matter velocity at its production for a given reheat temperature.

In Chapter 4 we consider how including scattering interactions between the dark matter and SM particles could effect our constraints. If dark matter can efficiently transfer momentum to SM particles it has a way to rapidly cool after its production. In Chapter 3, however, we show the vast majority of particles are produced near reheating. Thus if the dark matter decouples from the SM early in the EMDE, very few dark matter particles are ever able to interact with the SM and results from the noninteracting case are still largely applicable. If dark matter remains coupled to the SM well after reheating, then the dark matter acquires the standard thermal velocity distribution and all record of its nonthermal history is lost. Interactions between dark matter and the SM only leave a distinctive impact on the dark matter velocity distribution function when the decoupling occurs at or near reheating. In Chapter 4, we explore to what extent our constraints can be relaxed if these interaction are included.

Throughout this work we will use $M_{\mathrm{Pl}} = (8\pi G)^{-1/2}$, natural units $c = \hbar = k_B = 1$, and the metric convention $(-,+,+,+)$.

CHAPTER 2

Dark Energy: Quartic Chameleons

[1]In the commonly-considered runaway chameleon models, the field rolls to some value far from the minimum of its effective potential after inflation and remains stuck there during the radiation-dominated era due to Hubble friction. The chameleon's coupling to the trace of the stress-energy tensor makes it sensitive to the energy density, ρ, and pressure, P, of the radiation bath through the quantity $\Sigma \equiv (\rho - 3P)/\rho$. While the Universe is radiation dominated, Σ is nearly zero and the chameleon is light enough that Hubble friction is able to prevent it from rolling toward its potential minimum. However, as the temperature of the radiation bath cools, particle species in thermal equilibrium become nonrelativistic and Σ momentarily becomes nonzero. The chameleon then gains mass, is able the overcome Hubble friction, and is seemingly "kicked" toward the minimum of its effective potential [104].

Originally, the kicks were seen as an auspicious way to bring runaway chameleons to their potential minimum prior to Big Bang Nucleosynthesis (BBN).[2] However, they impart such a high velocity to the field that the chameleon rebounds off the other side of its effective potential back to field values further from the potential minimum than where it was stuck when the kick began [105]. However, Ref. [105] also showed that the inclusion of a coupling between the chameleon and the electromagnetic field offers a solution. The chameleon's coupling to a primordial magnetic field allows the chameleon to overcome Hubble friction and begin oscillating about its potential minimum prior to the kicks. For a sufficiently rapidly oscillating field, the kicks then have little effect on the chameleon's evolution.

These kicks further jeopardized chameleon theories by throwing into question their validity as a classical field theory [42, 43]. The effective potential in runaway models is minimized when $\phi \sim M$, and at field values $\phi \lesssim M$, the extremely steep slope of the bare potential leads to rapid changes in the chameleon's effective

[1]The contents of this chapter have been published as an article in Physical Review D. The original citation is as follows: Carisa Miller and Adrienne Erickcek. Quartic Chameleons: Safely Scale-Free in the Early Universe. *Phys. Rev.* D94:104049, 2016.

[2]A consequence of the chameleon's coupling to matter is that any variation in the chameleon field can be recast as a variation in particle masses in the Jordan frame. As we know particle masses differed very little between BBN and the present day, this constrains the chameleon to be at or near the minimum of its potential prior to the onset of BBN [104].

mass for small field displacements. Thus, the GeV-scale velocity with which the chameleon approaches its meV-scale minimum after the kicks causes nonadiabatic changes in the mass that excite extremely energetic fluctuations and lead to the quantum production of particles [42, 43]. Quantum corrections due to particle production then invalidate the classical treatment of the chameleon field and the particles' trans-Planckian energies cast doubt on the chameleon's viability as an Effective Field Theory (EFT) at the energy scale of BBN.

We will show that the quartic potential is able to avoid these problems due to its scale-free nature. In the early Universe, a chameleon field in a quartic potential oscillates rapidly with a large amplitude far beyond the minimum of its effective potential. In the classical treatment, the chameleon would continue this behavior until the end of radiation domination and still be oscillating far outside its minimum at the onset of BBN. A quantum treatment of the chameleon's motion shows that these oscillations will create particles, albeit with much less energy than those created during the rebounds off runaway potentials. The same quantum effects that were catastrophic to previous chameleon models will cause the field to lose energy and bring the quartic chameleon to its potential minimum prior to the onset of the kicks. Consequently, for the quartic chameleon, these kicks do not have as significant an influence on the field's evolution as in models with runaway potentials. Depending on the value of κ, the rate at which the field loses energy can vary significantly. For large values of κ, the field can lose all of its initial energy to particle production within the first oscillation and fall to its minimum. However when κ is closer to unity only a small percentage of the energy is lost during each oscillation, but the total effect accumulates over many oscillations to introduce a decay factor to the amplitude that still allows the field to reach its potential minimum before the kicks.

We begin with a brief review of chameleon gravity and then analyze the evolution of a classical chameleon field in a quartic potential in Section 2.1. Then, in Section 2.2, we consider the effects of quantum particle production on the field and investigate how the energy lost to this process is affected by the choice of κ. Section 2.3 explores how the kicks affect the field, and we follow up with concluding remarks in Section 2.4.

2.1 Classical Chameleons

In theories of chameleon gravity, the action can be written as

$$S = \int d^4x\sqrt{-g_*}\left[\frac{M_{\rm Pl}^2}{2}R_* - \frac{1}{2}(\nabla_*\phi)^2 - V(\phi)\right] + S_m\left[\tilde{g}_{\mu\nu}, \psi_m\right], \tag{2.1}$$

where g_* is the determinant of the metric $g^*_{\mu\nu}$ that solves the Einstein equations, R_* is its Ricci scalar, and $V(\phi)$ is the potential of the chameleon field, ϕ. The spacetime metric $\tilde{g}_{\mu\nu}$ that appears in the action for the matter fields, S_m, governs geodesic motion and is conformally coupled to the Einstein metric by

$$\tilde{g}_{\mu\nu} = e^{-2\beta\phi/M_{\rm Pl}}\, g^*_{\mu\nu}, \tag{2.2}$$

where β is a positive, dimensionless coupling constant assumed to be of order unity.[3] This coupling implies that the Einstein-frame stress-energy tensor of the matter fields is $T^{\mu}_{*\ \nu} = e^{-4\beta\phi/M_{\rm Pl}}\tilde{T}^{\mu}{}_{\nu}$. With this relationship between $T^{\mu}_{*\ \nu}$ and $\tilde{T}^{\mu}{}_{\nu}$, the Einstein and Jordan frame energy density and pressure can be related by $\rho_*/\tilde{\rho} = P_*/\tilde{P} = e^{-4\beta\phi/M_{\rm Pl}}$. It follows that any quantity that is a ratio of elements of the stress energy tensor, such as Σ or $w \equiv P/\rho$, is the same in both frames and can be evaluated using either Einstein- or Jordan- frame quantities.

Varying the action with respect to $g^*_{\mu\nu}$ implies that $T^{\mu}_{*\ \nu}$ is not conserved in the Einstein frame, as energy is exchanged between matter and the chameleon field. However, as the scalar and matter fields do not interact in the Jordan frame, the Jordan-frame stress-energy tensor is conserved: $\tilde{\nabla}_{\mu}\tilde{T}^{\mu}{}_{\nu} = 0$. In a Friedmann-Robertson-Walker spacetime, the scale factors in the Jordan and Einstein frames are related by $\tilde{a} = e^{-\beta\phi/M_{\rm Pl}}a_*$ and the proper times are related by $d\tilde{t} = e^{-\beta\phi/M_{\rm Pl}}dt_*$. Since the Einstein-frame matter density is not conserved, it does not follow the usual a_*^{-3} scaling. Radiation, however, still follows the expected a_*^{-4} behavior. To show this, we begin by writing the conservation equation in the Jordan frame,

$$\tilde{\rho} \propto \tilde{a}^{-3(w+1)}. \tag{2.3}$$

[3] In most other chameleon theories, the bare potential and the matter coupling term must slope in opposite directions in order to produce the required minimum in the effective potential, and the coupling is generally given with a positive exponential. However, for the quartic potential, the coupling may slope in either direction and still produce a minimum, so in following with Ref. [44] we will use this form of the coupling, which essentially gives a coupling constant β that is negative compared to most theories.

Exchanging the Jordan frame quantities for those of the Einstein frame, we have

$$\begin{aligned}
\rho_* e^{4\beta\phi/M_{\rm Pl}} &\propto \left(a_* e^{-\beta\phi/M_{\rm Pl}}\right)^{-3(w+1)}, \\
\rho_* e^{4\beta\phi/M_{\rm Pl}} &\propto a_*^{-3(w+1)} e^{3\beta\phi/M_{\rm Pl}(w+1)}, \\
\rho_* e^{\beta\phi/M_{\rm Pl}(1-3w)} &\propto a_*^{-3(w+1)}.
\end{aligned} \tag{2.4}$$

For matter we have $w = 0$ and Eq. (2.4) becomes

$$\rho_{*m} e^{\beta\phi/M_{\rm Pl}} \propto a_*^{-3}. \tag{2.5}$$

Clearly, the Einstein-frame energy density in matter, ρ_{*m}, does not scale as a_*^{-3}. This follows from our earlier statement that the stress-energy tensor that is conserved in the Einstein frame is not $T_*^{\mu}{}_{\nu}$, but the sum of $T_*^{\mu}{}_{\nu}$ and the stress-energy tensor of the chameleon field. Often it has been the practice to define the left-hand side Eq. (2.5) as the matter density as it is the quantity that follows the conservation equation in the Einstein frame [24, 104].

For radiation, however, $w = 1/3$ and we find from Eq. (2.4) that

$$\rho_{*R} \propto a_*^{-4}. \tag{2.6}$$

In both frames the energy density in radiation is proportional to a_*^{-4}, and it follows that $H_* \propto a_*^{-2}$. Throughout the remainder of the work we will drop the $*$ subscript on the scale factor when discussing how quantities scale in the Einstein frame.

The relationship between $T_*^{\mu}{}_{\nu}$ and $\tilde{T}^{\mu}{}_{\nu}$ also implies that the Jordan-frame temperature, T_J, depends on ϕ. As entropy is conserved in the Jordan frame, $g_{*S}\left(T_J\right)\tilde{a}^3 T_J^3$ is constant, and the expression for T_J in terms of ϕ and a_* is

$$T_J \left[g_{*S}\left(T_J\right)\right]^{1/3} = \left[g_{*S}\left(T_{J,i}\right)\right]^{1/3} T_{J,i} e^{-\beta(\phi_i-\phi)/M_{\rm Pl}} \frac{a_{*,i}}{a_*}. \tag{2.7}$$

where $a_{*,i}$ is the initial value of a_*, $\phi_i = \phi(a_{*,i})$, and $T_{J,i} = T_J(a_{*,i})$.

2.1.1 Chameleon Cosmology

Varying the action with respect to the field ϕ gives the equation of motion for the chameleon:

$$\ddot{\phi} + 3H_*\dot{\phi} = -\frac{dV}{d\phi} - \frac{\beta}{M_{\rm Pl}} T^{\mu}_{*\,\mu}; \tag{2.8}$$

$$= -\frac{dV}{d\phi} + \frac{\beta}{M_{\rm Pl}}(\rho_* - 3P_*), \tag{2.9}$$

where the dot denotes a derivative with respect to proper time t_* in the Einstein frame and $H_* \equiv \dot{a}_*/a_*$.

The effective potential that controls the evolution of the chameleon field is

$$V_{\rm eff}(\phi) = V(\phi) - \frac{\beta\phi}{M_{\rm Pl}}(\rho_* - 3P_*); \tag{2.10}$$

$$= \frac{\kappa}{4!}\phi^4 - \frac{\beta\phi}{M_{\rm Pl}}\Sigma\rho_*, \tag{2.11}$$

where κ is a dimensionless constant, and we have used the definition $\Sigma \equiv (\rho_* - 3P_*)/\rho_*$. Quantum loop corrections to the classical potential and limits on fifth forces constrain β and κ. The chameleon mechanism depends on an increase in the chameleon's effective mass in order to hide its effects, however quantum corrections to its potential also increase with its mass. Maintaining the reliability of fifth-force predictions requires that these corrections remain small compared to the classical potential and places an upper limit on the chameleon mass that implies $\kappa \lesssim 100$ [106]. Laboratory searches for fifth forces, in turn, have already placed lower bounds on the chameleon mass, which can to used to constrain κ from below for given β [107]. In order for κ to be of order unity, the chameleon coupling must be $\beta \lesssim 10^{-1}$. Conversely, in order for β to be of order unity, κ must be $\gtrsim 50$.

The minimum of this effective potential,

$$\phi_{\rm min} = \left(\frac{6\beta\Sigma\rho_*}{\kappa M_{\rm Pl}}\right)^{1/3}, \tag{2.12}$$

is dependent on ρ_* and on P_* through the definition of Σ, and so, too, is the chameleon's effective mass $m^2 = d^2V/d\phi^2\big|_{\phi=\phi_{\rm min}}$. The mass increases with ρ_*, making the chameleon heavier in regions of high density and unable to mediate a long-range force.

When evaluating the chameleon equation of motion, we work with a dimensionless scalar field $\varphi \equiv \phi/M_{\rm Pl}$, as well as with $p \equiv \ln(a_*/a_{*,i})$. Primes will now denote differentiation with respect to this new time

variable p and the first Friedmann equation is

$$H_*^2 = \frac{\rho_* + V}{3M_{\rm Pl}^2\left[1-(\varphi')^2/6\right]}. \tag{2.13}$$

Using the above equation and the fact that $\Sigma \ll 1$ during radiation domination and $V(\phi) \ll \rho_*$, the chameleon equation of motion, Eq. (2.9), can be written as

$$\frac{\rho_* + V}{\left[1-(\varphi')^2/6\right]}\varphi'' = -\varphi'\left(\rho_* + 3V\right) - 3\left(\frac{dV}{d\varphi} - \beta\Sigma\rho_*\right). \tag{2.14}$$

We will use this equation in order to explore the evolution of a chameleon field in a quartic potential throughout the radiation-dominated era.

The initial conditions for Eq. (2.14) follow from the field's dynamics prior to reheating. During inflation, the equation of state parameter w is approximately -1, and the comparatively large value of the kick function, $\Sigma = (1-3w) \simeq 4$, sets the value of $\phi_{\rm min}$ drastically greater than it is during radiation domination. The mass of the field at its minimum is

$$m^2 = \frac{\kappa}{2}\phi_{\rm min}^2 = \left(\frac{9}{2}\kappa\beta^2\right)^{1/3}\left(\frac{\Sigma\rho_*}{M_{\rm Pl}}\right)^{2/3}. \tag{2.15}$$

When $\Sigma \gtrsim 1$, the response time of the field m^{-1} is much shorter than the Hubble time H_*^{-1} as long as $\rho_* \ll M_{\rm Pl}^4$,

$$\frac{m^2}{H_*^2} \simeq 3\left(\frac{9}{2}\kappa\beta^2\right)^{1/3}\left(\frac{\Sigma^2 M_{\rm Pl}^4}{\rho_*}\right)^{1/3}. \tag{2.16}$$

Therefore, the field is massive enough to roll to its minimum prior to the onset of radiation domination. The fact that $m^2 \gg H^2$ also implies that the chameleon field is massive enough during inflation that quantum effects do not generate superhorizon perturbations in its value.

During reheating, the energy density ρ_* (be it of the inflaton or another oscillating scalar field) is converted into radiation. The value of the kick function then drops to $\Sigma \ll 1$, and $\phi_{\rm min}$ is pushed to significantly smaller field values; see Eq. (2.12). For all reheat temperatures much less than $M_{\rm Pl}$ we can assume that the chameleon begins at rest with ϕ equal to the value of $\phi_{\rm min}$ just prior to the drop in Σ, because $m^2 \gg H^2$, as shown in Eq. (2.16). At temperatures greater than a TeV, the QCD trace anomaly implies that the value of Σ

is 0.001 [108]. Σ then maintains this value until $T_J \simeq 600$ GeV when contributions from massive particles become comparable. As the temperature decreases, Σ begins to increase as $\Sigma \propto m_t^2/T^2$, where m_t is the mass of the most massive SM particle species: the top quark [108].

At $T_J \simeq 200$ GeV the process that gives the kick function its name begins. As the temperature of the radiation bath decreases, the energy density and pressure of massive particles decay at slightly different rates, allowing Σ to reach non-negligible values. This happens as each SM particle becomes nonrelativistic, but contributions from some species merge together, and the entire process results in four distinct kicks. The contributions from each particle are suppressed by a factor of $g_*(T_J)^{-1}$, where $g_*(T_J)$ is the effective degrees of freedom. As the temperature cools, $g_*(T_J)$ decreases, and each kick becomes larger than the last with the final kick due to the electrons reaching a value of $\Sigma \simeq 0.1$. For a detailed calculation of the kick function Σ, see Appendix A of Ref. [43].

2.1.2 Quartic Chameleons

For the runaway potentials usually considered in chameleon gravity, the value of $V(\phi)$ approaches infinity as $\phi \to 0$ and drops off rapidly as ϕ increases. The effective potential is then dominated by $V(\phi)$ near $\phi = 0$ and by the linear matter-coupling term at field values greater than $\phi_{\rm min}$. During inflation, the large value of Σ makes the slope of the matter-coupling term in Eq. (2.10) steeper, and the chameleon sits in a potential minimum at a small ϕ value. When inflation ends and Σ decreases, the slope of the matter contribution to $V_{\rm eff}$ becomes shallow and the minimum of the effective potential moves to larger values of ϕ. The chameleon then rolls down its bare potential, past the minimum, and out to where the effective potential is dominated by the matter-coupling term. The field then becomes stuck due to Hubble friction until it is kicked back toward the minimum of its effective potential.

The quartic chameleon, however, feels the effects of its bare potential on both sides of the minimum of its effective potential. As previously discussed, the comparatively large value of Σ prior to reheating fixes $\phi_{\rm min}$ at a large value far from zero. Throughout this analysis, we use the subscript i to indicate the value of a quantity just prior to the onset of radiation domination, which we take to occur at a Jordan-frame temperature $T_{J,i} = 10^{16}$ GeV. The value of $\phi_{\rm min}$ is then

$$\phi_i \simeq 0.0062 M_{\rm Pl} \left(\frac{\beta}{\kappa}\right)^{1/3}. \tag{2.17}$$

We have also assumed an era of inflation prior to radiation domination and have therefore used $\Sigma_i = 4$. However, nonstandard histories can easily be accounted for by changing this value in Eq. (2.12). We will show that the values of Σ_i and $T_{J,i}$, only set the initial oscillation amplitude of the field, to which the subsequent evolution is largely insensitive.

When the value of Σ drops from 4 to 0.001 at the end of inflation, the value of $\phi_{\rm min}$ decreases by a factor of $(0.001/4)^{1/3} \simeq 0.06$. The chameleon then rolls rapidly down its bare potential toward this new minimum. In its decent to its potential minimum, the chameleon gains sufficient energy that the slight tilt at the bottom of the quartic well due to the now small matter coupling does very little to affect its motion as it passes through $\phi_{\rm min}$ and climbs up the other side of its bare potential. It climbs to almost the same potential value as it started before turning around and falling again with nearly the same energy. It continues in this fashion, oscillating back and forth, all but oblivious to the matter coupling.

The oscillation amplitude decreases as Hubble friction causes the energy in the chameleon field to redshift away as a^{-4}. This behavior can be understood easily by the virial theorem. For a general power-law potential of the form $V(\phi) = C\phi^n$, the virial theorem relates the rapidly oscillating field's average kinetic and potential energies, K and V, by

$$2\bar{K} = n\bar{V}. \tag{2.18}$$

The equation-of-state parameter w is then

$$w = \frac{\bar{P}}{\bar{\rho}} = \frac{\frac{1}{2}\dot{\phi}^2 - V}{\frac{1}{2}\dot{\phi}^2 + V} = \frac{n-2}{n+2}. \tag{2.19}$$

Using this value of w, we can determine how the chameleon energy will scale with expansion by using the conservation equation:

$$\begin{aligned} \rho &= \rho_0 a^{-3(1+w)}; \\ &= \rho_0 a^{-3(\frac{2n}{n+2})}. \end{aligned} \tag{2.20}$$

For a quartic potential, $n = 4$ and the last line implies that the energy scales as a^{-4}. As we have already seen, radiation will also scale as $\rho_{*R} \propto a^{-4}$, and so $\rho_\phi/\rho_{*R} \sim V_i/T_{J,i}^4 \ll 1$. Technically, the chameleon's energy does not exactly obey Eq. (2.20) because there is a small amount of energy exchanged between the field and

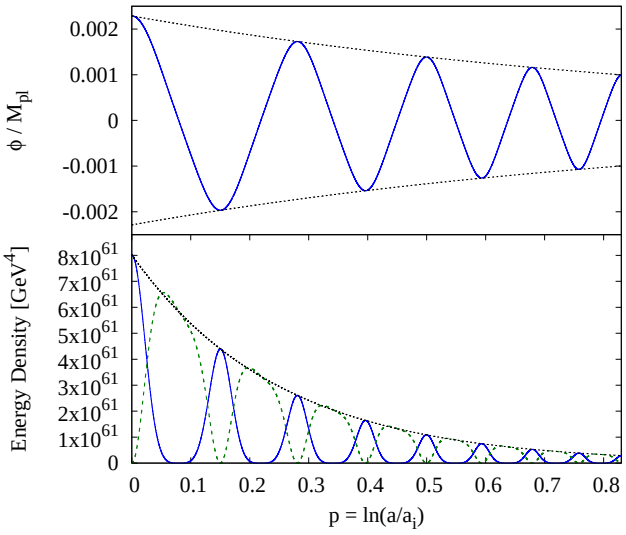

Figure 2.1: Top: The value of φ (blue, solid) and the values of its minima and maxima, $-\varphi_i a^{-1}$ and $\varphi_i a^{-1}$, respectively (black, dotted) over the course of four oscillations. Bottom: The kinetic (green, dashed) and potential (blue, solid) energies of the chameleon and their amplitude, $V_i a^{-4}$ (black, dotted). The potential energy reaches a maximum twice during each complete oscillation when $|\varphi|$ is at a maximum. The kinetic energy reaches its maxima both times φ passes through $\varphi_{\rm min}$. At all times the chameleon energy density is much less than that of the radiation $\rho_{*R} \sim (T_{J,i} a^{-1})^4 = 10^{64} a^{-4}$GeV (In this and all figures $\beta = 0.1$ and $\kappa = 2$.)

matter. However, we will show later in Section 2.2.2 that the corrections to the evolution of the chameleon's energy density are negligible.

As the energy in the chameleon field is the sum of its kinetic and potential energies, the maximum values of both of these quantities during each oscillation will scale as a^{-4}. The potential energy of the field when it reaches the peak of each oscillation, $V_{\rm max}$, and its kinetic energy each time the field passes through the minimum of its potential, $K_{\rm max} = \dot{\phi}^2_{\rm max}/2$, are both related to the field's initial potential energy by $V_{\rm max} = K_{\rm max} = V_i a^{-4}$. The quartic relation between ϕ and V implies that the amplitude of the ϕ oscillations decays as a^{-1}, so the value of ϕ at the peak of each oscillation is $\phi_{\rm max} = \phi_i a^{-1}$. Both of these behaviors can be seen in Figure 1, which shows the value of φ in the top panel and the kinetic and potential energy of the field in the bottom panel plotted over the course of several oscillations. These plots are generated from the numerical solution to Eq. (2.14) assuming $\varphi_i' = 0$ and $\varphi_i = \phi_i / M_{\rm Pl}$ with $\beta = 0.1$ and $\kappa = 2$.

The fact that the quartic chameleon begins at $\phi_i \ll M_{\rm Pl}$ and does not exceed this value is an interesting difference compared to runaway models. The field value at which runaway models become stuck due to

friction can be nearly equal to $M_{\rm Pl}$ [104]. If the field remains stuck at such values until BBN, the large variation of ϕ from its potential minimum can be interpreted as a larger variation in particle masses than we know to be allowed. Quartic chameleons, however, are already at field values much less than $M_{\rm Pl}$ before the end of inflation and oscillate with a decreasing amplitude. While we will show that the field still finds its minimum prior to the kicks, it is not strictly necessary to avoid endangering the success of BBN.

Equation (2.12) implies that $\phi_{\rm min}$ is proportional to the cube root of the energy density in radiation and so will decay as $a^{-4/3}$. Thus, $\phi_{\rm min}$ will decrease faster than the oscillation amplitude by a factor of $a^{-1/3}$, implying that the value of ϕ at the maximum of its oscillations will always exceed the minimum of its effective potential. Therefore, our classical treatment of the chameleon's behavior suggests that it would spend most of its time in regions dominated by its bare potential far from the minimum of its effective potential (though not far enough to significantly effect particle masses), allowing the oscillations to continue indefinitely while the Universe is radiation dominated. The high-energy oscillations of the field prevent it from becoming stuck due to Hubble friction or falling into and tracking its minimum. However, as the problems with other chameleon models demonstrate, the quantum effects associated with rapid changes in the chameleon field can significantly alter this classical behavior.

2.2 Quantum Chameleons

In chameleon models with runaway potentials, the only instances of rapid changes of the chameleon field after inflation occur when the chameleon is kicked toward its potential minimum with a very high velocity and rebounds off its steep bare potential. The rapid changes in the mass of the chameleon during this rebound excite high-energy perturbations that, in a naive, classical evaluation, exceed the energy initially available to the chameleon field. Considerations of the backreaction of particle production on the field showed that quantum corrections significantly alter the form of the potential experienced by the chameleon field. These corrections radically change the chameleon's evolution throughout the rebound, causing it to turn around long before it would have exhausted the kinetic energy it possessed going into the rebound, which keeps the occupation numbers of the excited modes extremely small [43].

In this section we show that every oscillation of the quartic chameleon excites perturbations, but with small enough energies that the energy lost to particle production does not exceed the initial energy of the field. For increasing values of κ we find that the limit at which this is no longer the case coincides with the

results Ref. [106], which also used quantum corrections to place an upper bound on κ. For the relatively large values of κ near this limit, the field can lose all of its initial energy to particles before it completes an oscillation, and it simply falls to its potential minimum. For smaller values ($\kappa \lesssim \mathcal{O}(1)$), the energy lost is only a small fraction of the field's energy at the start of an oscillation, and the evolution of the field over a single oscillation is not significantly altered. Instead, this energy loss accumulates over many oscillations and introduces an additional decay factor to the oscillation amplitude causing it to decay faster and reach its potential minimum.

2.2.1 Particle Production

We first summarize how rapid changes in the chameleon's effective mass excite perturbations [109]; for a more detailed review of this process, see Appendix C of Ref. [43]. We begin by decomposing the field into its spatial average $\bar{\phi}(t)$ and the perturbation $\delta\phi$:

$$\phi(t, \mathbf{x}) = \bar{\phi}(t) + \delta\phi(t, \mathbf{x}). \tag{2.21}$$

The linearized perturbation equation that governs the evolution of $\delta\phi$ is

$$\left[\partial_t^2 + 3H\partial_t - \frac{\nabla^2}{a^2} + V''_{\text{eff}}(\bar{\phi})\right] \delta\phi = 0. \tag{2.22}$$

Throughout this section we will not be using the variable p, and primes will denote differentiation with respect to the argument of the function.

To quantize the perturbations, we introduce the creation and annihilation operators $\hat{a}^\dagger_{\mathbf{k}}$ and $\hat{a}_{\mathbf{k}}$, respectively, which obey the standard commutation relations,

$$\left[\hat{a}_{\mathbf{k}}, \hat{a}^\dagger_{\mathbf{k}'}\right] = (2\pi)^3 \delta^{(3)}\left(\mathbf{k} - \mathbf{k}'\right). \tag{2.23}$$

The annihilation operator annihilates the vacuum state: $\hat{a}_{\mathbf{k}}|0\rangle = 0$. Using $\hat{a}^\dagger_{\mathbf{k}}$ and $\hat{a}_{\mathbf{k}}$ we can then express $\delta\phi(\tau)$ as

$$\hat{\delta\phi}(\tau, \mathbf{x}) = \int \frac{d^3k}{(2\pi)^3} \left[\hat{a}_{\mathbf{k}} \frac{\phi_k(\tau)}{a(\tau)} e^{i\mathbf{k}\cdot\mathbf{x}} + \hat{a}^\dagger_{\mathbf{k}} \frac{\phi^*_k(\tau)}{a(\tau)} e^{-i\mathbf{k}\cdot\mathbf{x}}\right], \tag{2.24}$$

where τ is conformal time. Inserting this decomposition of $\delta\phi$ into Eq. (2.22), we find

$$\phi_k''(\tau) + \omega_k^2(\tau)\phi_k = 0; \tag{2.25}$$

$$\omega_k^2(\tau) = k^2 + a^2 V_{\rm eff}''(\bar{\phi}) - \frac{a''(\tau)}{a}, \tag{2.26}$$

where $\omega_k^2(\tau)$ is the effective mass of a plane-wave perturbation in the chameleon field with a comoving wavenumber k.

During radiation domination $a''(\tau) = 0$, and

$$\omega_k^2 = k^2 + a_*^2 V_{\rm eff}''\left(\bar{\phi}\right) \simeq k^2 + \frac{\kappa}{2}(a_*\phi)^2, \tag{2.27}$$

where in the last equality we have dropped the bar over ϕ as we will be working exclusively with the spatially averaged field. We also neglect the matter coupling because it is subdominant to the bare potential throughout most of the oscillation. When $\omega_k'(\tau)/\omega_k^2 \gtrsim 1$, perturbations in the field are excited. Taking the derivative of this effective mass with respect to τ, we find

$$\begin{aligned}\omega_k'(\tau) &= \frac{a_*^3}{2\omega_k}\left[2H_* V''(\phi) + V'''(\phi)\dot{\phi}\right]; \\ &= \frac{a_*^3}{2\omega_k}\left[\kappa H_*\phi^2 + \kappa\phi\dot{\phi}\right].\end{aligned} \tag{2.28}$$

We can simplify the last line of the equation by noting that not only is $H_*\phi^2$ initially smaller than $\phi\dot{\phi}$, it also redshifts away faster. This can be seen by recalling the relations $\phi_{\rm max} = \phi_i a^{-1}$, $\dot{\phi}_{\rm max} = \sqrt{2K_{\rm max}} = \sqrt{2V_i a^{-4}}$, and using the fact that, during radiation domination, H_* decreases as a^{-2}. With these results, the maximum value of the first term during each oscillation is $H_*\phi_{\rm max}^2 \simeq H_{*,i}\phi_i^2 a^{-4}$. The second term, however, is a product of two oscillating functions that reach their maxima at different times. From the approximately sinusoidal nature of ϕ, we can determine that the product of ϕ and its derivative $\dot{\phi}$ will behave as the product of their amplitudes and another sinusoidal function, thus, $(\phi\dot{\phi})_{\rm max}$ is proportional to $\phi_{\rm max}\dot{\phi}_{\rm max}$. The constant of proportionality can be numerically determined and is $\approx$0.6 for all β and κ. The amplitude of the second term is then $(\phi\dot{\phi})_{\rm max} \sim \phi_{\rm max}\dot{\phi}_{\rm max} \simeq \phi_i a^{-1}\sqrt{2K_{\rm max}} \simeq \sqrt{\kappa/12}\phi_i^3 a^{-3}$. We can see that $H_*\phi^2 \propto a^{-4}$ will decay away faster than $\phi\dot{\phi} \propto a^{-3}$. Thus, if $H_*\phi^2$ is initially the smaller of the two terms, we can neglect it.

During radiation domination, $H_*^2 \simeq \rho_{*R}/(3M_{\rm Pl}^2)$, and from Eq. (2.12), we know that $\phi_i = [24\beta\rho_{*R,i}/(\kappa M_{\rm Pl})]^{1/3}$. Assuming that $T_i = 10^{16}$ GeV, the relative contribution between the two terms is $\sqrt{12/\kappa}H_{*,i}/(0.6\phi_i) \simeq 0.05(\kappa\beta^2)^{-1/6}$. Thus, as long as $\kappa\beta^2 > 1.56 \times 10^{-8}$, which is true provided that neither β nor κ is unreasonably small, this ratio is less than 1 and we can neglect the $H_*\phi^2$ term in Eq. (2.28).

By setting the ratio $\omega_k'(\tau)/\omega_k^2$ equal to 1, we can find the physical wavenumbers, $k_{\rm phys} = k/a_*$, of the perturbations that are excited during the oscillations. Using Eqs. (2.27) and (2.28), we now have

$$\begin{aligned}\frac{\omega_k'(\tau)}{\omega_k^2(\tau)} &\simeq \frac{a_*^3}{2\omega_k^3}\left(\kappa\phi\dot{\phi}\right), \\ &= \frac{a_*^3}{2}\frac{\kappa\dot{\phi}\phi}{\left[k^2 + \frac{\kappa}{2}(a_*\phi)^2\right]^{3/2}}, \\ &= \frac{\kappa\dot{\phi}\phi}{2\left[k_{\rm phys}^2 + \frac{\kappa}{2}\phi^2\right]^{3/2}}. \end{aligned} \tag{2.29}$$

Setting this ratio equal to 1, and solving the last line for $k_{\rm phys}$, we get

$$k_{\rm phys}^2 = \left(\frac{\kappa}{2}\phi\dot{\phi}\right)^{2/3} - \frac{\kappa}{2}\phi^2. \tag{2.30}$$

This expression reaches its maximum value four times during a single oscillation, as shown in Figure 2.2.

To evaluate $k_{\rm phys}$ we again use how the maxima of the contributing quantities are related to the initial field value and corresponding initial potential energy. Already we have established that, for the first term, $(\phi\dot{\phi})_{\rm max} = A\phi_{\rm max}\dot{\phi}_{\rm max}$, where $A \simeq 0.6$. It is also important to note that the terms in Eq. (2.30) do not reach their maxima at the same time $k_{\rm phys}$ is at its maxima. To account for these proportionalities we introduce the numerical parameters B and C to relate the maxima of the two terms to their values when $k_{\rm phys}$ is at its

maxima. The maximum value of $k_{\rm phys}$ during an oscillation is then

$$\begin{aligned}
\left(k_{\rm phys}^{\rm max}\right)^2 &= B\left(\frac{\kappa}{2}A\phi_{\rm max}\dot{\phi}_{\rm max}\right)^{2/3} - C\frac{\kappa}{2}\phi_{\rm max}^2 \\
&= A^{2/3}B\left(\frac{\kappa}{2}\phi_i a^{-1}\sqrt{\frac{\kappa}{12}\phi_i^4 a^{-4}}\right)^{2/3} - C\frac{\kappa}{2}\phi_i^2 a^{-2} \\
&= \frac{\kappa}{2}\left[\left(\frac{A^2}{6}\right)^{1/3}B - C\right]\phi_i^2 a^{-2} \\
k_{\rm phys}^{\rm max} &= D\sqrt{\frac{\kappa}{2}}\phi_i a^{-1} \qquad (2.31) \\
&= D(6\kappa)^{1/4}V_i^{1/4}a^{-1}. \qquad (2.32)
\end{aligned}$$

For $\beta = 0.1$ and $\kappa = 2$, $B \simeq 0.6$, $C \simeq 0.1$, and as it is defined in the last equation, $D \simeq 0.4$. Changing β or κ by two orders of magnitude does not significantly effect the value of A, B, C, or D.

As well as being proportional to the oscillation amplitude, the a^{-1} behavior of $k_{\rm phys}^{\rm max}$ implies that it also scales with the temperature. Starting from Eq. (2.31), the relationship between $k_{\rm phys}^{\rm max}$ and the Jordan-frame temperature becomes apparent when ϕ_i is determined by evaluating Eq. (2.12) using $\Sigma = 4$ and $\rho_{*,i} = (\pi^2/30)g_*(T_{J,i})T_{J,i}^4$. After combining all numerical factors, we find that

$$\begin{aligned}
k_{\rm phys}^{\rm max} &\simeq 2.67(\kappa\beta^2)^{1/6}\left(\frac{(T_{J,i})^4}{M_{\rm Pl}}\right)^{1/3}a^{-1}, \\
&\simeq 2.67(\kappa\beta^2)^{1/6}\left(\frac{T_{J,i}}{M_{\rm Pl}}\right)^{1/3}T_J, \qquad (2.33)
\end{aligned}$$

where we have used the fact $T_J \propto a^{-1}$ during radiation domination.[4] For $T_{J,i} = 10^{16}$ GeV, $\beta = 0.1$, and $\kappa = 2$, the ratio of $k_{\rm phys}$ to the temperature is $k_{\rm phys}^{\rm max}/T_J \simeq 0.23$, as shown in Figure 2.

The fact that the energy of the modes excited in quartic models is dependent only on the initial value of the field is another important contrast to runaway models. The energy of excited modes in such models is dependent on the velocity with which the chameleon approaches the minimum, $\dot{\phi}_M$, which is of order GeV^2. Reference [43] found that for a power-law potential of the form

$$V(\phi) = M_v^4\left[1 + \left(\frac{M_s}{\phi}\right)^n\right], \qquad (2.34)$$

[4]Though the temperature does depend on ϕ, variations in the field have a negligible effect on the temperature as long as $\phi \ll M_{\rm Pl}$, as the lack of deviation from the expected a^{-1} behavior in the temperature plotted in Figure 2.2 shows.

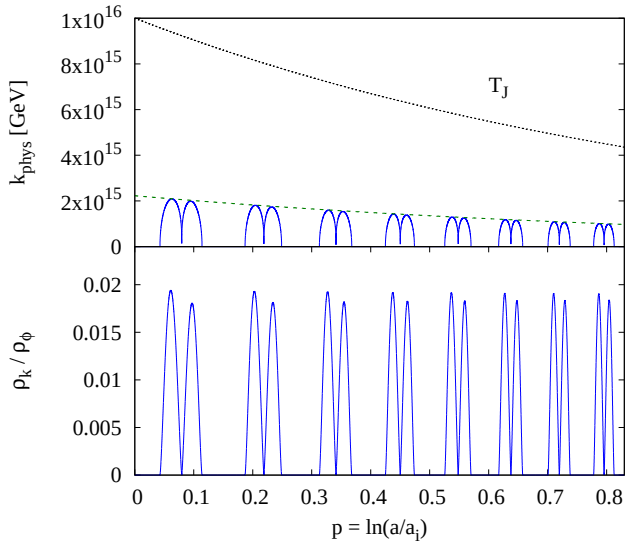

Figure 2.2: Top: The value of $k_{\rm phys}$ (blue, solid) over four oscillations. During each oscillation, $k_{\rm phys}$ reaches a maximum four separate times at approximately the middle of the climb and decent on each side of the potential. The value of this maximum, $k_{\rm phys}^{\rm max}$ (green, dashed), is on the order of the temperature and decays as a^{-1}. Bottom: The ratio of the energy in the perturbations to the energy in the chameleon field over four oscillations. Each oscillation sees approximately a total 0.08 fractional loss of energy.

the most energetic mode that is excited has a physical wave number

$$k_{\rm phys} = \frac{(n+2)}{2\sqrt{2}} \frac{|\dot{\phi}_M|}{M_s} \left(\frac{M_s}{\bar{\phi}_{\rm ta}} \right). \tag{2.35}$$

where $\bar{\phi}_{\rm ta} \lesssim M_s$ is the value of ϕ at which the field turns around. Since $M_s \sim$ meV, the ratio of $\dot{\phi}_M \sim T_J^2$ and M_s results in the excitation of extremely energetic modes even at low temperatures: $k_{\rm phys} \gg \sqrt{\dot{\phi}_M} \sim T_J$. For the quartic chameleon, however, highly energetic modes are only excited at high temperatures: $k_{\rm phys} \lesssim T_J$.

Using our value of $k_{\rm phys}$, we can evaluate the energy density in the perturbations:

$$\begin{aligned} \rho_k = \frac{k^3 n_k \omega_k}{2\pi^2 a^4} &\simeq \frac{k_{\rm phys}^3}{2\pi^2} \sqrt{k_{\rm phys}^2 + V''(\phi)}, \\ &= \frac{k_{\rm phys}^3}{2\pi^2} \sqrt{\left(\frac{\kappa}{2} \dot{\phi} \phi \right)^{2/3} - \frac{\kappa}{2}\phi^2 + \frac{\kappa}{2}\phi^2}, \\ &= \frac{k_{\rm phys}^3}{2\pi^2} \left(\frac{\kappa}{2} |\phi \dot{\phi}| \right)^{1/3}, \end{aligned} \tag{2.36}$$

where $n_k \sim 1$ is the mode occupation number. In the same way that we found $k_{\rm phys}^{\rm max}$ by relating the maxima of the quantities in Eq. (2.30) to the initial potential energy, we can find the maximum of ρ_k during each

oscillation,

$$\rho_k^{\max} = \frac{D^3}{2\pi^2} 6^{5/6} \kappa V_i a^{-4}. \tag{2.37}$$

From Section 2.1 we know that the chameleon's energy density equals $V_i a^{-4}$. Therefore, the maximum of the ratio of ρ_k and the chameleon energy density ρ_ϕ is constant, as we can see in the bottom panel of Figure 2.2. The ratio of these two quantities is dependent on κ: $\rho_k^{\max}/\rho_\phi \simeq 0.01\kappa$. To ensure our quantum corrections are kept under control, this ratio must be < 1, and we must have $\kappa \lesssim 100$. This is the same bound found by Ref. [106], which used another approach to limit quantum corrections. Runaway models could only keep this ratio less than 1 if the occupation number was extremely small, $n_k \lll 1$, which required altering the classical evolution of the field.

For $\kappa \gtrsim \mathcal{O}(10)$ the chameleon field will lose all of its energy before it has a chance to complete its first oscillation, at which point it will settle into its potential minimum. For smaller values of κ, however, the depreciation in the field's energy is not as dramatic, and the small fractional loss of energy does not significantly affect the field's evolution during a single oscillation. Instead, the effect accumulates over many oscillations, as we explore in the next section.

2.2.2 Effects of Particle Production for $\kappa \lesssim \mathcal{O}(1)$

While the fraction of the energy lost in each oscillation is constant, the length of each oscillation period, Δp, is not, as can be seen in Figure 2. The duration of the oscillations scales as follows:

$$\begin{aligned} \Delta p &\simeq \frac{4\varphi_{\max}(p)}{\varphi'_{\text{avg}}}, \\ &\simeq \frac{4\varphi_i e^{-p}}{\varphi'_{\text{avg}}}, \end{aligned} \tag{2.38}$$

where φ'_{avg} is the average value of φ' over a single oscillation and once again primes denote differentiation with respect to p. To more clearly see the behavior of Δp, we first remark on the quantity $\varphi' = \dot{\phi}/(M_{\text{Pl}} H_*)$. Radiation domination implies that H_* will decrease as a^{-2}, and the fact that the maximum kinetic energy of the chameleon during an oscillation, $\dot{\phi}^2_{\max}/2$, is proportional to a^{-4} implies that $\dot{\phi}_{\max}$ also decreases as a^{-2}. Therefore, the amplitude of the φ' oscillations is a constant value: $\varphi'_{\max}$. Since $\varphi'_{\max}$ is constant, so too is its average, and Δp decays with the amplitude of φ. The two values φ'_{avg} and $\varphi'_{\max}$ can be related by a constant

scaling factor found numerically to be $q \equiv \varphi'_{\rm avg}/\varphi'_{\rm max} \simeq 0.76$, and is highly insensitive to changes in β and κ of up to 2 orders of magnitude.

When considering the energy lost during each oscillation, it is useful to consider how the quantities $\varphi_{\rm max}$ and $\varphi'_{\rm avg}$ are related to the energy at the start of each oscillation, $\rho(p)$:

$$\varphi_{\rm max}(p) = \left(\frac{4!}{\kappa}\frac{\rho(p)}{M_{\rm Pl}^4}\right)^{1/4} \tag{2.39}$$

$$\varphi'_{\rm max}(p) = \frac{\dot{\phi}_{\rm max}}{H_* M_{\rm Pl}} = \frac{\sqrt{2\rho(p)}}{H_* M_{\rm Pl}} = \sqrt{\frac{\kappa}{12}}\frac{M_{\rm Pl}}{H_*}\varphi^2_{\rm max}(p), \tag{2.40}$$

where we have used the fact that the maximum kinetic energy that occurs during each oscillation, $\dot{\phi}^2_{\rm max}/2$, is equal to the potential energy at the start of each oscillation.

In Section 2.1.2 we used the canonical definitions of the energy density and pressure of a scalar field, namely $\rho_\phi = \dot{\phi}^2/2 + V$ and $P_\phi = \dot{\phi}^2/2 - V$, to determine its equation of state, w. However, when defining w in this way, because the field's coupling to matter allows it to exchange energy with the matter fields, the chameleon does not follow the conservation equation,

$$\frac{\dot{\rho}_\phi}{\rho_\phi} - 3H_*^2(1+w) \neq 0. \tag{2.41}$$

With Eq. (2.40) we are now equipped to revisit this assumption. If we instead introduce a new pressure,

$$P_n = \frac{1}{2}\dot{\phi}^2 - V - \frac{1}{3H_*}\dot{\phi}\frac{\beta}{M_{\rm Pl}}\Sigma\rho_* \tag{2.42}$$

we can see that with this new definition, the field now obeys the conservation equation,

$$\begin{aligned}
&\dot{\rho}_\phi + 3H_*(\rho_\phi + P_n) = \\
&= \dot{\phi}\ddot{\phi} + \frac{dV}{d\phi}\dot{\phi} + 3H_*\left(\frac{\dot{\phi}^2}{2} + V + \frac{\dot{\phi}^2}{2} - V - \frac{1}{3H_*}\dot{\phi}\frac{\beta}{M_{\rm Pl}}\Sigma\rho_*\right) \\
&= \dot{\phi}\left(\ddot{\phi} + 3H_*\dot{\phi} + \frac{dV}{d\phi} - \frac{\beta}{M_{\rm Pl}}\Sigma\rho_*\right).
\end{aligned} \tag{2.43}$$

The terms in parentheses in the last line make up the chameleon's equation of motion, Eq. (2.9), and the entire quantity in parentheses is indeed equal to 0. While we used the canonical form of the pressure in

Section 2.1.2, we also took its average value over many oscillations, and the term which we have added to the potential is not positive-definite, and will average to 0.

Not only will it average to 0, but we can also show that the additional contribution to the new pressure is negligible compared to the usual terms. Using the relation $\dot{\phi} = H_* M_{\rm Pl} \varphi'$, we can rewrite P_n as

$$\begin{aligned} P_n &= \frac{1}{2}(H_* M_{\rm Pl}\varphi')^2 - V - \frac{1}{3}\varphi'\beta\Sigma\rho_* \\ &= \frac{1}{6}\rho_*\varphi'^2 - V - \frac{1}{3}\varphi'\beta\Sigma\rho_*. \end{aligned} \tag{2.44}$$

The maximum values of the first two terms, the kinetic and potential energies of the field, are equal and so to compare the relative contribution of the last term, we will look specifically at how it compares the kinetic energy. The maximum value reached by φ', given in Eq. (2.40), can be broken down further using the initial values of the field and H_*,

$$\begin{aligned} \varphi'_{\rm max} &= \sqrt{\frac{\kappa}{12}}\sqrt{\frac{3}{\rho_{*,i}}}\left(\frac{6\beta\Sigma_i\rho_{*,i}}{\kappa M_{\rm Pl}}\right)^{2/3} \\ &\simeq \left(\frac{\beta^4}{\kappa}\right)^{1/6}\left(\frac{81}{4}\Sigma_i^4\frac{\rho_{*R,i}}{M_{\rm Pl}^4}\right)^{1/6}. \end{aligned} \tag{2.45}$$

Combining numerical factors and using $T_{J,i} = 10^{16}$ GeV we have

$$\varphi'_{\rm max} = 0.19\left(\frac{\beta^4}{\kappa}\right)^{1/6}. \tag{2.46}$$

The relative contribution of the two terms is then $\beta\Sigma/\varphi'_{\rm max} \sim 0.005(\kappa\beta^2)^{1/6}$, which for even some of the larger values of κ and β allowed ($\kappa = 100$, $\beta = 1$) is still much less than 1. Therefore, the additional term is a negligible contribution to the canonical pressure, and our use of the conservation equation, Eq. (2.20), is valid.

Using Eqs. (2.39) and (2.40) and the scaling constant q, Eq. (2.38) then becomes

$$\begin{aligned} \Delta p &= \frac{4}{q}\sqrt{\frac{12}{\kappa}}\frac{H_*}{M_{\rm Pl}}\varphi_{\rm max}^{-1}, \\ &= \frac{4}{q}\left(\frac{6}{\kappa}\right)^{1/4} H_i e^{-2p}\rho^{-1/4}, \qquad (2.47) \\ &= \frac{1}{Q}e^{-2p}\rho^{-1/4}, \qquad (2.48) \end{aligned}$$

where H_i is the initial Hubble value at the end of inflation and in the last line we have condensed all the constants into one constant, Q^{-1}.

Over the course of each oscillation, the energy of the chameleon field decreases by a factor of $e^{-4\Delta p}$ due the expansion of the Universe, as well as by an additional factor due to the creation of particles. If we take $f \lesssim 1$ as the fraction of energy left after the field has lost energy due to the production of particles during one oscillation, we can write the change in energy over one oscillation period as

$$\begin{aligned} \frac{\Delta\rho}{\Delta p} &= \frac{f\rho_{\rm init}e^{-4\Delta p} - \rho_{\rm init}}{\Delta p}, \\ &\simeq \frac{f\rho_{\rm init}(1-4\Delta p) - \rho_{\rm init}}{\Delta p}. \end{aligned} \tag{2.49}$$

If $f = 1$ we recover the original $\rho \propto e^{-4p}$ evolution. Using Eqs. (2.48) and (2.49) we can write a differential equation for the energy loss including particle production,

$$\begin{aligned} \frac{d\rho}{dp} &= -\rho\left[\frac{1-f}{\Delta p} + 4f\right] \\ &= -Q(1-f)e^{2p}\rho^{5/4} - 4f\rho \end{aligned} \tag{2.50}$$

The second term in Eq. (2.50) gives the classical $\rho \propto a^{-4}$ evolution and dominates at small p. But the e^{2p} factor in the first term allows it to quickly dominate over the second term. If we consider the regime in which the second term has become negligible, we can integrate Eq. (2.50) and see that the energy will follow an entirely different behavior at late times:

$$\begin{aligned} \frac{d\rho}{dp} &= -Q(1-f)e^{2p}\rho^{5/4} \\ \int \frac{d\rho}{\rho^{5/4}} &= -Q(1-f)\int e^{2p}dp \\ \rho &= \left[\frac{Q(1-f)}{8}e^{2p} + C\right]^{-4} \end{aligned} \tag{2.51}$$

where C is a constant of integration. At large values of p, when this behavior is relevant, the exponential term will dominate over the constant and the energy will scale as e^{-8p}. The two regimes and behavior of ρ can be seen in Figure 2.3. The p value at which the e^{-8p} behavior begins to take over is determined by κ, with larger values of κ leading to an earlier change in regimes.

When the e^{-8p} term begins to dominate, the amplitude of the oscillations will then decay as e^{-2p}. This is faster than its original e^{-p} behavior and, more importantly, faster than the $e^{-4p/3}$ decay of the minimum of its effective potential. The oscillation amplitude will then decrease below the value of $\phi_{\rm min}$ and the field will fall into its minimum.

We have seen that the oscillatory motion of the chameleon in a quartic well creates large variations in the field's mass. Particle production must be considered, but the inclusion of these quantum effects does not result in the catastrophic effects experienced by other chameleon potentials. Instead the energy of excited modes is comparable to the temperature and the fraction of the initial energy lost to particle production is always less than 1 as long as $\kappa \lesssim 100$. Next we investigate whether quartic chameleons can also avoid the problems runaway models encounter when facing the kicks.

2.3 Kicking the Quartic Chameleon

After the depletion of energy to particle production takes the chameleon field to or near the minimum of its effective potential, we can show that it will track its minimum until the onset of the kicks. The characteristic time scale for the evolution of the minimum is $\phi_{\rm min}/\dot{\phi}_{\rm min}$, whereas the characteristic time scale of the response of the field is given by m^{-1}. When the field is in the minimum of its effective potential,

$$m^2 = \left.\frac{d^2V}{d\phi^2}\right|_{\phi=\phi_{\rm min}} = \frac{\kappa}{2}\phi_{\rm min}^2 = \left(\frac{9}{2}\kappa\right)^{1/3}\left(\frac{\beta\Sigma}{M_{\rm Pl}}\rho_*\right)^{2/3}. \tag{2.52}$$

If $m \gg \dot{\phi}_{\rm min}/\phi_{\rm min}$, the field will adiabatically track its minimum. To compare these values, first we must determine $\dot{\phi}_{\rm min}$:

$$\begin{aligned}
\dot{\phi}_{\rm min} &= H\frac{d\phi_{\rm min}}{dp}, \\
&= \frac{2\beta}{\kappa M_{\rm Pl}}\frac{H}{\phi_{\rm min}^2}\left(\rho_{*R}\frac{d\Sigma}{dT} + \Sigma\frac{d\rho_{*R}}{dT}\right)\frac{dT}{dp}, \\
&\simeq \frac{2\beta}{\kappa M_{\rm Pl}}\frac{H}{\phi_{\rm min}^2}\rho_{*R}\left(\frac{d\Sigma}{dT} + 4\frac{\Sigma}{T}\right)(-T), \\
&= -\frac{1}{3}H\phi_{\rm min}\left(4 + \frac{T}{\Sigma}\frac{d\Sigma}{dT}\right),
\end{aligned} \tag{2.53}$$

where we have used the definition of $\phi_{\rm min}$ given by Eq. (2.12), the fact that $\rho_* \propto T^4 \propto a^{-4}$, and that $\phi \ll M_{\rm Pl}$ implies $T \simeq T_J$. If Σ is constant, the second term in parentheses drops out, and we recover

the $\phi_{\rm min} \propto a^{-4/3}$ behavior we determined in Section II. Thus, when Σ is constant, the evolution of the minimum is set by the expansion rate, and the characteristic time scale is approximately the Hubble time H^{-1}. Comparing this to the mass of the field in its minimum, we have

$$\begin{aligned}\frac{m^2}{\left(\frac{\dot{\phi}_{\rm min}}{\phi_{\rm min}}\right)^2} = \frac{4}{3}\frac{m^2}{H^2} &= \frac{4}{3}\left(\frac{9}{2}\kappa\right)^{1/3}\left(\frac{\beta\Sigma}{M_{\rm Pl}}\rho_*\right)^{2/3}\left(\frac{3M_{\rm Pl}^2}{\rho_*}\right), \\ &= 4\left(\frac{9}{2}\kappa\beta^2\right)^{1/3}\left(\frac{\Sigma^2 M_{\rm Pl}^4}{\frac{\pi^2}{30}g_* T^4}\right)^{1/3}. \end{aligned} \tag{2.54}$$

We can see that, for reasonable values of κ and β, the mass of the field at its potential minimum is much greater than H for all $T \ll M_{\rm Pl}$ while Σ is constant.

Only if the field is positioned in a very small interval ($|\Delta\phi| \ll \phi_{\rm min}$) around $\phi = 0$ is the effective mass less than H. However, even in this region, the constant nature of Σ due to the QCD trace anomaly does not allow the field to become stuck due to Hubble friction. In this small region the effective potential is dominated by the matter coupling; if we neglect the driving term from the bare potential and use the fact that $V \ll \rho_{*R}$, we can simplify Eq. (2.14) to

$$\varphi'' = -\varphi' - 3\beta\Sigma. \tag{2.55}$$

Integrating this equation for a chameleon initially at rest gives

$$\varphi' \simeq 3\Sigma\beta\left(1 - e^{-p}\right). \tag{2.56}$$

From this we see that φ' will increase toward a constant value until the field approaches its potential minimum and the bare potential can no longer be neglected. Thus, even if the chameleon begins at rest in a region where it has a low effective mass, Hubble friction will not prevent it from reaching its potential minimum. We have just shown in Eq. (2.54) that once it reaches this minimum it will then track it adiabatically.

Having established that the chameleon oscillates about its minimum at the onset of the kicks, we can now look at how they will affect the field's evolution. Comparing m and $\dot{\phi}_{\rm min}/\phi_{\rm min}$ when Σ is no longer

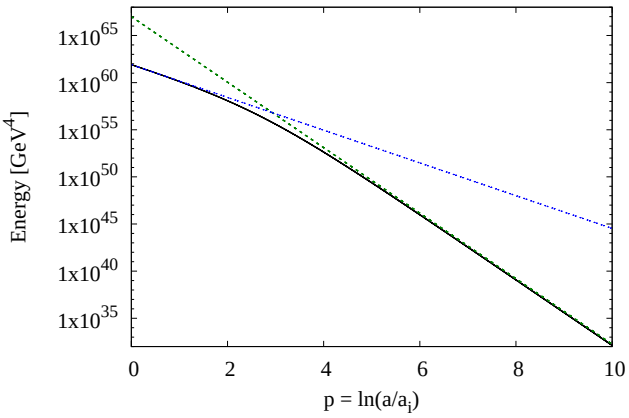

Figure 2.3: The energy in the chameleon field at the peak of each oscillation (black, solid), showing the effect of particle production on the energy decay, found by numerically solving Eq. (2.50). While the energy begins redshifting as a^{-4} (blue, dotted), particle production eventually dominates the energy loss and the energy decays as a^{-8} (green, dashed).

constant, we have

$$\frac{m^2}{\left(\frac{\dot{\phi}_{\rm min}}{\phi_{\rm min}}\right)^2} = \frac{m^2}{H^2}\frac{9}{\left(4+\frac{T}{\Sigma}\frac{d\Sigma}{dT}\right)^2}. \tag{2.57}$$

The kick function Σ displays two different types of behavior: at the beginning of the kicks when the temperature is greater than the mass of the particle species, m_i, $\Sigma \propto m_i^2/T^2$, and at the end of the kicks, when $T < m_i$, Boltzmann suppression makes $\Sigma \propto e^{-m_i/T}$. We can estimate the ratio in Eq. (2.57) using these two behaviors and the ratio m^2/H^2 given by Eq. (2.54). At the beginning of the kicks, when $d\Sigma/dT = -2\Sigma/T$,

$$\begin{aligned}\frac{m^2}{\left(\frac{\dot{\phi}_{\rm min}}{\phi_{\rm min}}\right)^2} &= \frac{m^2}{H^2}\frac{9}{4} \\ &\simeq \left(\frac{\Sigma M_{\rm Pl}^2}{T^2}\right)^{2/3}.\end{aligned} \tag{2.58}$$

Even though $\Sigma \ll 1$, the quantity $(M_{\rm Pl}/T)^2$ is more than sufficient to make this ratio $\gg 1$. At the end of the kicks, however, when $d\Sigma/dT = -m_i\Sigma/T^2$,

$$\frac{m^2}{\left(\frac{\dot{\phi}_{\rm min}}{\phi_{\rm min}}\right)^2} = \frac{m^2}{H^2}\frac{9}{\left(4+\frac{m_i}{T}\right)^2} \simeq \left(\frac{\Sigma T M_{\rm Pl}^2}{m_i^3}\right)^{1/3}, \tag{2.59}$$

which is only > 1 as long as $M_{\rm Pl}^2/m_i^3 > (\Sigma T)^{-1}$. This is true up until the end of the electron-positron kick, when the temperature and the value of Σ continue to decrease past the point that $M_{\rm Pl}^2/m_e^3$ can no longer compensate for their increasingly small values. For $\beta = 0.1$ and $\kappa = 2$, this occurs at approximately a temperature of 39 keV, when $\phi_{\rm min} \sim 10^{-33} M_{\rm Pl}$.

Figure 2.4 shows the value of $\phi_{\rm min}$ as a function of the temperature. The solid line shows the minimum under the influence of the kicks, while the dashed line shows the minimum following the $a^{-4/3}$ decay when Σ is constant. The effect of the kicks for the most part is to slow the decrease in the minimum of the effective potential compared to this decay, until the very end of the kicks when Boltzmann suppression drastically decreases the value of Σ. In Figure 2.5 we have plotted the exact value of the ratio in Eq. (2.57), and we can see that the ratio is indeed much greater than 1 until after the last kick. Therefore the chameleon will track its minimum adiabatically until then. When this occurs, even if we assume the field becomes entirely stuck while the potential minimum continues to decrease toward zero, the deviation of the field from its minimum cannot exceed the value at which it was stuck: $\sim 10^{-33} M_{\rm Pl}$. This is clearly $\ll M_{\rm Pl}$ and any implied variation in the particle masses would be completely negligible. When the Universe later becomes matter dominated and $\Sigma = 1$, the field will once again be able to track the minimum of its effective potential.

2.4 Discussion

Since the chameleon model was first proposed as an alternative to dark energy [24, 23], its cosmological impacts have been studied extensively. While it has been shown that chameleon theories cannot account for the expansion of the Universe without the addition of a constant term to its potential [25], the field's sensitive dependence on its environment gives it remarkable properties that are of great interest. However, for most chameleon models, the same matter coupling that gives it its unique phenomenology leads these theories into trouble in the early Universe. The meV mass scale of runaway potentials is at odds with the GeV

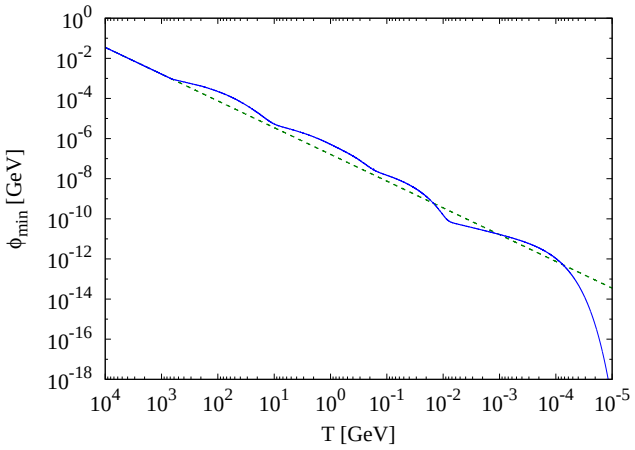

Figure 2.4: The value of $\phi_{\rm min}$ during the kicks (blue, solid) and the extrapolation of the $e^{-4p/3}$ behavior experienced during the period when Σ is constant (green, dashed). The value of $\phi_{\rm min}$ during the kicks actually decreases at a slower rate than it did when Σ was constant until the end of the last kick.

mass scale of SM particles, which accelerate the chameleon field to very high velocities when they become nonrelativistic. The hierarchy between these two energy scales leads to the quantum production of particles that radically alters the field's evolution. Without very weak couplings or highly tuned initial conditions these chameleon models cannot be trusted as effective field theories at the time of BBN [42, 43].

In this work, we have considered the quartic chameleon potential, which is not often studied in theories of chameleon gravity. A significant feature of this model is the fact that there is no mass scale in the potential: the chameleon's self-interaction is enough to ensure adequate screening. We have shown that this scale-free property of the potential allows the quartic chameleon to avoid the catastrophic effects of the small energy scales within runaway models.

After inflation, the quartic chameleon oscillates in its potential well. The amplitude of its oscillations are damped due to Hubble friction. In the classical treatment, the minimum of the field's effective potential decreases faster than the oscillation amplitude throughout radiation domination. Consequently, the field cannot reach its potential minimum before BBN, though the oscillation amplitude is always sufficiently small that the variation of the field from this minimum does not imply an unacceptable variation from known particle masses.

The rapid oscillations of the chameleon field cause changes in its effective mass that excite perturbations and lead to particle production. The effects of quantum particle production ensure that the field does reach its potential minimum while the Universe is radiation dominated. For large values ($\gtrsim 10$) of the self-interaction constant κ, the fractional loss of energy to these particles can be large, in which case the field loses all its

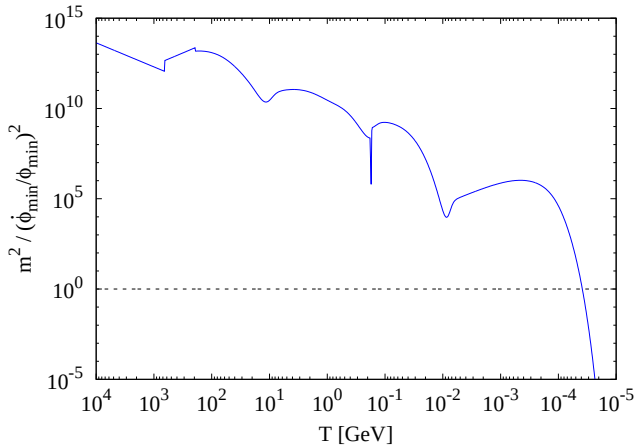

Figure 2.5: The numerical evaluation of the ratio in Eq. (2.57), which is significantly greater than 1 throughout the kicks. It becomes less than 1 when $T \simeq 3.9 \times 10^{-4}$GeV.

energy in the course of a single oscillation. For smaller κ, the energy lost to particles constitutes only a small fraction of the field's energy. This much slower energy loss accumulates over multiple oscillations and introduces an additional decay term to the oscillation amplitude which allows the field to catch its minimum after many oscillations. At this point, the field will adiabatically track its potential minimum. It will track this minimum until the very tail end of the kicks, when the Boltzmann suppression of Σ decreases the value of $\phi_{\rm min}$ faster than the field can follow. The value of the field at this point is sufficiently small that any deviation of particle masses implied by the deviation of the field from its potential minimum are entirely negligible.

The energy of the modes that are excited in the quartic model are on order of the temperature: highly energetic modes are only excited at high temperatures. This is an important contrast to runaway models, which experience extremely energetic fluctuations at relatively low temperatures and can no longer be treated as EFTs during BBN. While quantum corrections lead to extremely energetic fluctuations in the field and a breakdown in calculability for runaway models, quantum corrections to the quartic potential are comparatively small and are, in fact, necessary to ensure the field can reach its minimum. Once it reaches the minimum of its effective potential the chameleon can then adiabatically track this minimum even throughout the kicks. Thus, the quartic chameleon's scale-free nature means is not susceptible to problems arising from a hierarchy of scales and can remain a well-behaved effective field theory throughout the evolution of the early Universe.

CHAPTER 3

Dark Matter: Impact of Nonthermal Production on the Matter Power Spectrum

[1]As previously mentioned, it is commonly assumed that dark matter is thermally produced in the early universe during a period of radiation domination. The continuing lack of detection of particles which can fit this model has prompted many interesting modifications, notably the inclusion of a matter-dominated era following inflation and prior to the on set of radiation domination, during which decay of the dominating particle is the primary source of production of dark matter and standard model (SM) radiation. A typical assumption in analyses which consider this scenario is that the dark matter is produced nonrelativistically from the decay process. A more natural assumption, which does not require fine-tuning between the masses of the parent and daughter particles, is that both the dark matter and the SM particles are born relativistic. We investigate in this chapter the effects of imparting dark matter particles with relativistic velocities, and their implications for structure growth.

This chapter is organized as follows. We begin in Section 3.1 by introducing our model for reheating and nonthermal dark matter production and the resulting evolution of the average dark matter velocity. In Section 3.2 we derive a distribution function for the dark matter and use it to examine the fraction of dark matter that is nonrelativistic at reheating and the fraction whose velocity is sufficiently low to preserve the EMDE-enhanced structure formation. In Section 3.3 we examine conditions under which the dark matter velocity is high enough to run afoul of constraints from $\mathrm{Lyman}-\alpha$ forest observations and observed MW satellites. We conclude in Section 3.4. Any overlap in variable use between this chapter and the chameleon analysis, should be disregarded; all variables will be (re)defined and should not be confused with those of the previous chapter.

[1]The contents of this chapter have been published as an article in Physical Review D. The original citation is as follows: Carisa Miller,Adrienne Erickcek, and Riccardo Murgia. Constraining Nonthermal Dark Matter's Impact on the Matter Power Spectrum. *Phys. Rev.* D100:123520, 2019.

3.1 Nonthermal Production of Dark Matter

In the scenario we consider, the energy density of the Universe is dominated by an oscillating scalar field (or a massive particle species). As previously mentioned, for sufficiently rapid oscillations within a quadratic potential, the field's energy density scales as $\rho_\phi \propto a^{-3}$, and it exhibits the same dynamics and perturbation evolution as a pressureless fluid [61, 110, 111]. The Universe experiences an early "matter"-dominated era until the expansion rate equals the decay rate of the field, $H \simeq \Gamma_\phi$, at which point the Universe transitions from scalar to radiation domination. We use this transition to define the reheat temperature, $T_{\rm RH}$:

$$\sqrt{\frac{4\pi^3 G}{45} g_{*,\rm RH} T_{\rm RH}^4} = \Gamma_\phi, \tag{3.1}$$

where G is the gravitational constant and $g_{*,\rm RH}$ is the number of relativistic degrees of freedom at $T_{\rm RH}$. For a scalar field that decays into both dark matter and relativistic particles, the equations for the evolution of the energy densities of the scalar field ρ_ϕ, relativistic SM particles ρ_r, and dark matter ρ_χ are given by

$$\begin{aligned} \dot{\rho}_\phi &= -3H\rho_\phi - \Gamma_\phi \rho_\phi, \\ \dot{\rho}_r &= -4H\rho_r + (1-f)\Gamma_\phi \rho_\phi, \\ \dot{\rho}_\chi &= -3H(1+w_\chi)\rho_\chi + f\Gamma_\phi \rho_\phi. \end{aligned} \tag{3.2}$$

Here dots represent differentiation with respect to proper time, f is the fraction of the scalar's energy that is transferred to the dark matter, and w_χ is the dark matter equation-of-state parameter.

3.1.1 Dark Matter Abundance

In the above system of equations, we do not allow for scattering interactions between the dark matter and SM particles. Also, we neglect both the thermal production and self-annihilation of dark matter particles, effectively assuming that the velocity-averaged annihilation cross section is small enough that any amount of dark matter lost to annihilations is negligible and any produced thermally is negligible compared to that produced from scalar decay. However, if dark matter annihilations are s-wave, neglecting annihilations does not change the results of our conclusions because we are interested in the *average* dark matter velocity and the *fraction* of dark matter that has lost sufficient momentum to participate in structure formation.

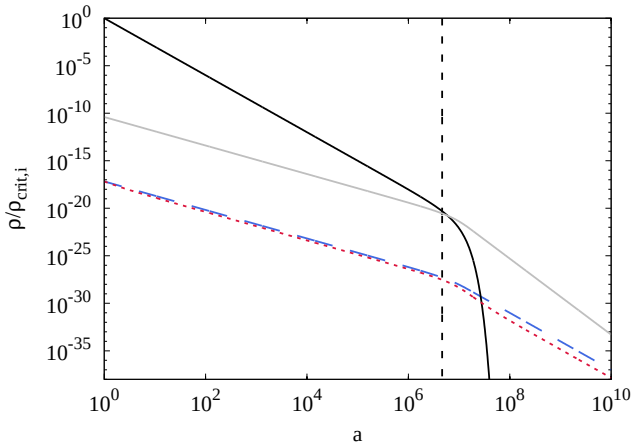

Figure 3.1: The energy densities of the scalar (black, solid), radiation (grey, solid), and dark matter for particles born relativistic ($v_D = 0.99$; red, dotted) and nonrelativistic ($v_D = 0.1$; blue, dashed). During the EMDE, both the dark matter and radiation densities scale as $a^{-3/2}$ while they are being sourced by the decaying scalar field. Here $f = 10^{-7}$ and the scalar decay rate is $\tilde{\Gamma}_\phi = \Gamma_\phi / H_i = 10^{-10}$. Reheating is marked by the thin vertical dashed line at $a_{\rm RH} = \tilde{\Gamma}_\phi^{-2/3}$.

These quantities are dependent on the velocity distribution of dark matter. For s-wave annihilations, the velocity-averaged cross section is independent of particle velocity, and the distribution of particle velocities would be unaffected by the inclusion of annihilations.

Without annihilations, constraining the reheat temperature to be above 3 MeV, as required by BBN, leads to a direct constraint on the fraction of the scalar's energy imparted to the dark matter: $f \lesssim 10^{-7}$ [95] for nonrelativistic dark matter. This branching ratio is quite small and it would be more natural to expect the energy imparted in the decay of the scalar to be more evenly allocated to both the dark matter and the SM. The inclusion of annihilations, however, significantly reduces the ratio of dark matter to radiation. This can allow for a more balanced transfer of energy, $f \sim 0.5$, while still achieving a sufficiently small dark matter abundance through annihilations [96, 80]. For relativistic dark matter, its abundance is also dependent on the velocity imparted to the particles at decay (v_D).

In our model, we consider the scenario in which the dark matter is produced via a two-body decay so that all dark matter particles are born with the same velocity, v_D. The energy density and decay rate of the scalar then govern the evolution of the equation of state w_χ for the dark matter particles during the EMDE. The rates at which new particles are produced and the momentum of existing particles redshifts away determine

the average energy per particle of the dark matter:

$$\langle E \rangle = \frac{\int_1^a \sqrt{m_\chi^2 + (\gamma m_\chi v(a, a_D))^2} \frac{d\hat{n}_\chi}{da_D} da_D}{\int_1^a \frac{d\hat{n}_\chi}{da_D} da_D}, \tag{3.3}$$

where $\hat{n}_\chi$ is the comoving number density of the dark matter particles, $v(a, a_D)$ is the velocity at a of a dark matter particle created at a_D, and we integrate over a_D with $a = 1$ setting the onset of dark matter production.

When evaluating Eq. (3.3) we use the fact that the comoving number density of the dark matter evolves according to

$$\frac{d\hat{n}_\chi}{dt} = b\Gamma_\phi \hat{n}_\phi, \tag{3.4}$$

where $\hat{n}_\phi$ is the comoving number density of ϕ particles, and b is the number of dark matter particles produced per scalar decay. We can then (following a procedure similar to that in Ref. [112]) express the term $d\hat{n}_\chi/da_D$ as

$$\frac{d\hat{n}_\chi}{da_D} = \frac{d\hat{n}_\chi}{dt}\frac{dt}{da_D} = \frac{b\Gamma_\phi \hat{n}_\phi}{\dot{a}_D} = \frac{b\Gamma_\phi \frac{\rho_\phi}{m_\phi} a_D^3}{a_D H_D} \propto \frac{\rho_\phi}{H_D} a_D^2. \tag{3.5}$$

The constants b, Γ_ϕ, and m_ϕ appear in both integrals in Eq. (3.3) and consequently do not affect $\langle E \rangle$. We numerically evaluate Eq. (3.3) to obtain the average energy as a function of the scale factor; this is made even simpler by noting that the contribution of the dark matter to the expansion rate at the time of decay, H_D, is entirely negligible compared to both the scalar and radiation energy densities. The calculation of the average energy then informs how the dark matter equation of state evolves:

$$w_\chi = -\frac{1}{3H\langle E \rangle}\frac{d\langle E \rangle}{dt}. \tag{3.6}$$

The mass of the dark matter particle can be pulled from both the average energy and its derivative, and so w_χ at any given time depends only on the average velocity.

Using Eq. (3.6), we numerically solve the set of equations in Eq. (3.2) with the initial condition $a_i \equiv a(t_i) = 1$, and we assume there is no dark matter in existence prior to this time. Figure 3.1 shows the evolution of the scalar, radiation, and relativistic ($v_D = 0.99$) and nonrelativistic ($v_D = 0.1$) dark matter

energy densities in our model. The energy densities in the figure are given as fractions of the initial critical energy density $\rho_{\mathrm{crit},i}$.

In Fig. 3.1, we have chosen to fix $f = 10^{-7}$, which directly sets the relative abundance of dark matter to radiation during the EMDE to be $\sim 10^{-7}$, and we have chosen a scalar decay rate $\tilde{\Gamma}_\phi \equiv \Gamma_\phi / H_i = 10^{-10}$, which sets $a_{\mathrm{RH}} \equiv \tilde{\Gamma}_\phi^{-2/3} \simeq 5 \times 10^6$. It is worth noting that, by this definition, $a_{\mathrm{RH}} \neq a|_{T=T_{\mathrm{RH}}}$. The numerical solutions to Eq. (3.2) show that by a scale factor of $3a_{\mathrm{RH}}$ enough of the scalar has decayed away that it is a negligible source of radiation. As a result, the radiation energy density then evolves as in the usual radiation-dominated era from a temperature $T(3a_{\mathrm{RH}}) \simeq 0.34 T_{\mathrm{RH}}$ onward. This sets the relation between a_{RH} and T_{RH} to be $a_{\mathrm{RH}}/a_0 = 1.54 (T_0/T_{\mathrm{RH}}) g_{*S}^{-1/3} (0.34 T_{\mathrm{RH}})$, where g_{*S} is the number of relativistic degrees of freedom in the entropy density.

The effects of the dark matter particles' velocities can already been seen in Fig. 3.1. During the EMDE, the energy density of any species, relativistic or nonrelativistic, sourced by scalar decay evolves as $\rho \propto a^{-3/2}$. At the end of the EMDE, when the scalar field is no longer sourcing new particles, the energy densities of the decay products will begin to scale as $\rho \propto a^{-3(w+1)}$. For a scenario in which dark matter is born relativistic, the average value of w_χ during reheating is close to $1/3$, and the dark matter behaves more like radiation. In Fig. 3.1 we can see that, following reheating, the energy density of relativistic dark matter (dotted) redshifts away faster than its nonrelativistic counterpart (dashed). Once the scalar field has decayed completely and there is no creation of new, hot particles, the existing particles' momenta continue to redshift until the average particle is no longer relativistic, and after that, the dark matter density scales as a^{-3}.

Increasing the velocity imparted to the dark matter particles upon their creation increases the time it takes after reheating for the dark matter energy density to begin scaling as a^{-3}, thus increasing the duration of radiation domination for a given value of f. The temperature at matter-radiation equality is $T_{\mathrm{eq}} = 0.795 \pm 0.005$ eV [1], and so a longer radiation-dominated era implies a higher temperature at reheating. For a fixed value of f, the reheat temperature that matches the observed dark matter abundance in a scenario of relativistically produced dark matter is a factor of γ_D greater than that of nonrelativistic dark matter, where γ_D is the Lorentz factor of the relativistic dark matter particle at production. For a given reheat temperature, the value of f required to produce the observed dark matter abundance is

$$f \simeq 2.3 \times 10^{-7} (3\mathrm{MeV}/T_{\mathrm{RH}}) \gamma_D. \tag{3.7}$$

In the absence of annihilations, the dark matter density during the EMDE is also determined by f: if $v_D \ll 1$ then $\rho_\chi/\rho_r \simeq (5/3)f$ [95], whereas if $v_D \simeq 1$ then $\rho_\chi/\rho_r \simeq f$. In the latter case, $\rho_\chi/\rho_r \simeq f$ continues until the dark matter is no longer relativistic or changes in g_* disrupt the a^{-4} scaling of ρ_r. Therefore, for $\gamma_D \gg 1$, obtaining the observed dark matter abundance requires that $\rho_\chi/\rho_r \simeq 2.3 \times 10^{-7}(3\text{MeV}/T_{\rm RH})\gamma_D$ shortly after reheating. This requirement applies regardless of whether or not annihilations alter the dark matter abundance during the EMDE. After reheating, but while the dark matter is still relativistic, the relative dark matter abundance will evolve as

$$\left.\frac{\rho_\chi}{\rho_r}\right|_T \simeq 2.3 \times 10^{-7} \left(\frac{3\text{MeV}}{T_{\rm RH}}\right) \gamma_D \times \left[\frac{g_{*S}\left(T\right)}{g_{*S}\left(0.34T_{\rm RH}\right)}\right]^{4/3} \frac{g_*\left(0.34T_{\rm RH}\right)}{g_*\left(T\right)}, \tag{3.8}$$

in either case.

If dark matter is still relativistic at neutrino decoupling, it could affect the predictions of BBN. Dark matter produced relativistically at reheating would still be relativistic ($\gamma \gtrsim 2$) when $T = 10$ MeV if

$$\gamma_D \gtrsim 2.4 g_{*S}^{1/3}(0.34T_{\rm RH})\frac{T_{\rm RH}}{10\text{MeV}}. \tag{3.9}$$

Relativistic dark matter behaves as an additional radiation component, and can be characterized as a change in the number of effective neutrinos, $\Delta N_{\rm eff}$. The energy density in relativistic particles can be written as

$$\begin{aligned} \rho_r + \rho_{\chi,\rm rel} &= \frac{\pi^2}{30}\left[g_* + \frac{7}{8} \times 2 \times \Delta N_{\rm eff}\left(\frac{T_\nu}{T}\right)^4\right] T^4, \\ \rho_{\chi,\rm rel} &= \frac{\pi^2}{30}\left(\frac{7}{8} \times 2 \times \Delta N_{\rm eff}\right) T_\nu^4, \end{aligned} \tag{3.10}$$

where T_ν is the neutrino temperature, which we assume evolves as a^{-1} after $T = T_\nu = 10$ MeV, when $g_*(10\text{MeV}) = g_{*S}(10\text{MeV}) = 10.75$. Thus, the fractional component of the energy density in dark matter at 10 MeV is related to $\Delta N_{\rm eff}$ by

$$\begin{aligned} f_{10\text{MeV}} \equiv \left.\frac{\rho_\chi}{\rho_r}\right|_{10\text{MeV}} &= \frac{7}{4}\Delta N_{\rm eff}\, g_{*S}^{-1}(10\text{MeV}) \\ &\simeq 0.074 \Delta N_{\rm eff}. \end{aligned} \tag{3.11}$$

Bounds from BBN constrain $N_{\rm eff} = 2.88 \pm 0.54$ at 95% C.L. [113], yielding an upper bound $f_{10\rm MeV} < 0.028$. If the dark matter is still relativistic at BBN, then achieving the observed relic abundance requires $f_{10\rm MeV} \simeq 5 \times 10^{-7} \gamma_D (3\rm MeV$ as given by Eq. (3.8). Therefore, the upper bound on $f_{10\rm MeV}$ translates to a bound $\gamma_D \lesssim 5.4 \times 10^4 (T_{\rm RH}/3\rm MeV) g_{*S}^{1/3} (0.34 T_{\rm RH}$

This upper bound on γ_D implies an upper bound on the value of f in Eq. (3.7) that can result in the observed relic abundance We will see in Section 3.3 that restrictions from small-scale structure on the parameter space of γ_D and $T_{\rm RH}$ provide much stronger bounds. As such, annihilations are still necessary to reduce the dark matter abundance to its required value following reheating without fine-tuning f.

3.1.2 The Adiabatic Cooling of Dark Matter

Given that the momentum of a particle scales as $p \propto a^{-1}$, a particle born from a decay at a scale factor a_D, with a physical velocity v_D, has a velocity at some later time given by

$$v^2(a, a_D) = \frac{v_D^2}{(1 - v_D^2) \left(\frac{a}{a_D}\right)^2 + v_D^2}. \tag{3.12}$$

The average velocity over all the dark matter particles at any given time is then

$$\langle v^2(a) \rangle = \left[\int_1^a v^2(a, a_D) \frac{d\hat{n}_\chi}{da_D} da_D \right] \left[\int_1^a \frac{d\hat{n}_\chi}{da_D} da_D \right]^{-1}, \tag{3.13}$$

which can be evaluated in the same manner as Eq. (3.3).

Figure 3.2 shows the evolution of the average dark matter particle velocity throughout the EMDE until just after reheating; the various curves in Fig. 3.2 represent different values of v_D. We can see that the average velocity is initially dominated by the few particles born immediately with the imparted velocity. The velocity of these particles begins to redshift away, pulling the average down, until a steady state is reached between the redshifting of the velocity of existing particles and the creation of new, hot particles.

In the regime where the average velocity has reached a constant value - deep into the EMDE and well before reheating - we can simplify our calculation of the average velocity even further and analytically solve the integrals of Eq. (3.13). During the EMDE, the energy density of the Universe is dominated by the scalar

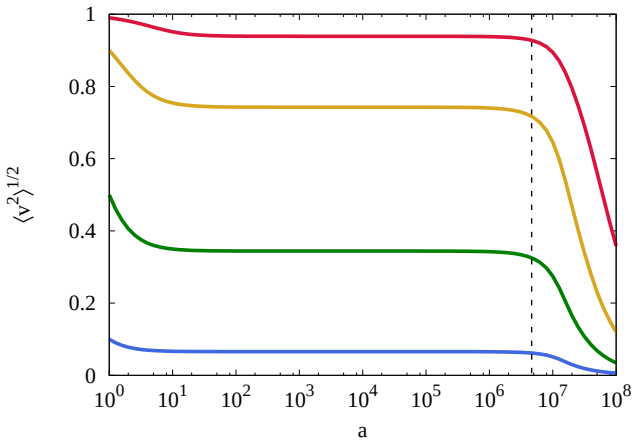

Figure 3.2: The average velocity of the dark matter particles as a function of scale factor a throughout the EMDE for $v_D = 0.1, 0.5, 0.9, 0.99$ (bottom to top). Reheating is marked by the thin vertical dashed line.

field, and our expression in Eq. (3.5) becomes

$$\frac{\rho_\phi}{H_D} a_D^2 \simeq \frac{\rho_{\phi,i} a_D^{-3}}{H_i a_D^{-3/2}} a_D^2 = \frac{\rho_{\phi,i}}{H_i} \sqrt{a_D}. \tag{3.14}$$

Rewriting the expression for v^2 to make its dependence on the integration variable, a_D, more apparent, we have

$$v^2(a, a_D) = \frac{a_D^2}{\left(\frac{a}{X}\right)^2 + a_D^2}, \tag{3.15}$$

where $X \equiv \gamma_D v_D$. And so, deep in the EMDE, our expression for the average velocity, given by Eq. (3.13), takes the form

$$\langle v^2(a) \rangle = \left[\int_1^a \frac{a_D^{5/2}}{\left(\frac{a}{X}\right)^2 + a_D^2} da_D \right] \left[\int_1^a \sqrt{a_D} da_D \right]^{-1}. \tag{3.16}$$

The solution to the integral in the numerator is given by

$$\begin{aligned} \int_1^a \frac{a_D^{5/2} da_D}{\left(\frac{a}{X}\right)^2 + a_D^2} \;=\; & \frac{2}{3}(a^{3/2} - 1) \;+\; \left(\frac{a}{2X}\right)^{3/2} \ln\left(\frac{1 + \sqrt{2X} + X}{1 - \sqrt{2X} + X} \; \frac{a - \sqrt{2aX} + X}{a + \sqrt{2aX} + X} \right) \\ & +\; 2\left(\frac{a}{2X}\right)^{3/2} \left[\tan^{-1}\left(1 - \sqrt{2X}\right) - \tan^{-1}\left(1 + \sqrt{2X}\right) \right. \\ & -\; \left. \tan^{-1}\left(1 - \sqrt{\frac{2X}{a}}\right) + \tan^{-1}\left(1 + \sqrt{\frac{2X}{a}}\right) \right]. \end{aligned} \tag{3.17}$$

The solution to the integral in the denominator is simply

$$\int_1^a \sqrt{a_D} da_D = \frac{2}{3}(a^{3/2} - 1). \tag{3.18}$$

Long after the decays have started ($a \gg 1$), both integrals scale as $a^{3/2}$ and $\langle v^2(a) \rangle$ is constant until just prior to reheating, at which point our approximation in Eq. (3.14) is no longer valid.

The steady state between the cooling of old particles and the creation of new, hot ones is maintained until just before reheating, and the average dark matter velocity at reheating is not reduced significantly from the velocity imparted at the scalar's decay. Relativistic-born dark matter, $v_D = 0.99$, is still considerably relativistic at reheating, $\sqrt{\langle v^2 \rangle} \simeq 0.93$. At reheating, the average dark matter particle is nonrelativistic only if v_D is already largely nonrelativistic: $\sqrt{\langle v^2 \rangle} \lesssim 0.01$ requires $v_D < 0.017$.

If the comoving size of the horizon at reheating, $k_{\rm RH}^{-1} = (a_{\rm RH} H_{\rm RH})^{-1}$, is smaller than the dark matter free-streaming horizon, $k_{\rm fs}^{-1}$, then the random drift of dark matter particles will erase the growth of density perturbations that occurred during the EMDE. Reference [95] found that $k_{\rm RH}/k_{\rm fs} < 1$ required the dark matter velocity at reheating to be $v_{\rm RH} \lesssim 0.06$. Preserving enhanced structure growth requires an even smaller average velocity. Achieving such a small average velocity at reheating would require the dark matter particles to be born with a similarly small velocity.

3.2 Dark Matter Distribution Function

Although the average dark matter particle may have too large a velocity to participate in enhanced structure formation, we would like to investigate what fraction of the dark matter population has a sufficiently low velocity to do so. Instead of considering the average particle velocity at reheating, we will consider what fraction of the dark matter has a velocity at reheating that is less than a percent of the speed of light. To this end, we begin by deriving the dark matter distribution function. At a given time, a, the fraction of dark matter with velocities below a particular threshold equals the fraction of dark matter born before the correspondingly required "birth time," a_D.

From the fact that $v/\sqrt{1-v^2} \propto a^{-1}$, we know that in order for a particle born with velocity v_D to have a velocity less than $v_{\rm RH}$ at reheating, that particle must have been born from decay at a scale factor,

$$a_D < \frac{v_{\rm RH}}{v_D}\sqrt{\frac{1-v_D^2}{1-v_{\rm RH}^2}}a_{\rm RH}. \tag{3.19}$$

Obtaining the distribution function in birth times of the dark matter particles, $f(a_D)$, will then allow us to compute the fraction of dark matter born before this time.

The fraction, ε, of dark matter particles born within a particular interval of scale factor, $a_{D,1} > a_D > a_{D,2}$, is given by

$$\varepsilon_{a_{D,12}} = \int_{a_{D,1}}^{a_{D,2}} f(a_D) da_D. \tag{3.20}$$

This fraction can also be directly computed by

$$\varepsilon_{a_{D,12}} = \frac{\int_{a_{D,1}}^{a_{D,2}} d\hat{n}_\chi}{\int_1^\infty d\hat{n}_\chi} = \frac{\int_{a_{D,1}}^{a_{D,2}} \frac{d\hat{n}_\chi}{da_D} da_D}{\int_1^\infty \frac{d\hat{n}_\chi}{da_D} da_D}. \tag{3.21}$$

Equating the two expressions for $\varepsilon_{a_{D,12}}$ and considering small intervals in the scale factor, we can derive an expression for the distribution function:

$$\begin{aligned} \frac{\int_{a_{D,1}}^{a_{D,2}} d\hat{n}_\chi}{\int_1^\infty d\hat{n}_\chi} &= \int_{a_{D,1}}^{a_{D,2}} f(a_D) da_D \\ &\simeq f(a_D)\Delta a_D, \\ f(a_D) &\simeq \frac{\int_{a_{D,1}}^{a_{D,2}} d\hat{n}_\chi}{\Delta a_D \int_1^\infty d\hat{n}_\chi}. \end{aligned} \tag{3.22}$$

Numerically evaluating Eq. (3.22), we obtain the distribution function of dark matter birth times seen plotted in Fig. 3.3 as $f(a_D/a_{\rm RH}) = a_{\rm RH} f(a_D)$. From Fig. 3.3, one can see that approximately half of the dark matter is born after reheating, $a/a_{\rm RH} > 1$.

From Eq. (3.19) one can find that, even for dark matter particles imparted with a velocity only half of the speed of light, only those born before $a_D \lesssim 0.017 a_{\rm RH}$ will have a velocity at reheating $v_{\rm RH} < 0.01$. Integrating our distribution function over this interval in a_D, we find the fraction of dark matter born before this time to be approximately 0.15%. Figure 3.4 shows the fraction of dark matter that has a velocity below

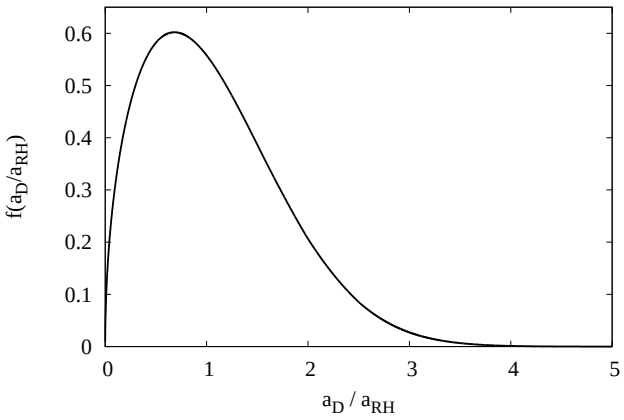

Figure 3.3: The birth time distribution function of dark matter for our model. The peak production of dark matter occurs just prior to reheating and $f(a_D/a_{\rm RH})$ is maximized at $a_D \simeq 0.68 a_{\rm RH}$.

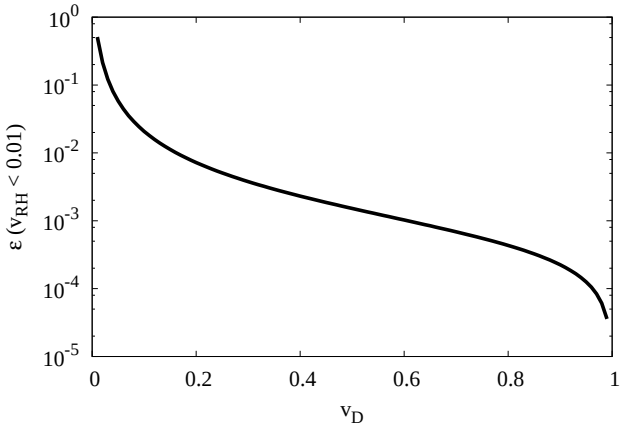

Figure 3.4: Fraction of dark matter whose velocity at reheating is $v_{\rm RH} < 0.01$ as a function of the assumed velocity imparted to the dark matter at its production.

$v = 0.01$ at reheating as a function of the given value of v_D. Even for dark matter born at only one tenth of the speed of light, only $\sim 2\%$ of the dark matter has the required $v_{\rm RH} < 0.01$.

One of the intriguing consequences of an EMDE is that density perturbations in matter grow linearly with scale factor during an EMDE, which is faster than the logarithmic growth expected during the typically assumed radiation-dominated epoch. We now examine what fraction of the dark matter is able to retain an appreciable perturbation enhancement from this linear growth. Since density perturbations grow linearly during the EMDE, a mode that enters the horizon at a scale factor of $0.1 a_{\rm RH}$ will grow by a factor of $\sim$10 during the EMDE, which we will consider "appreciable". The comoving wavelength of such a mode is given

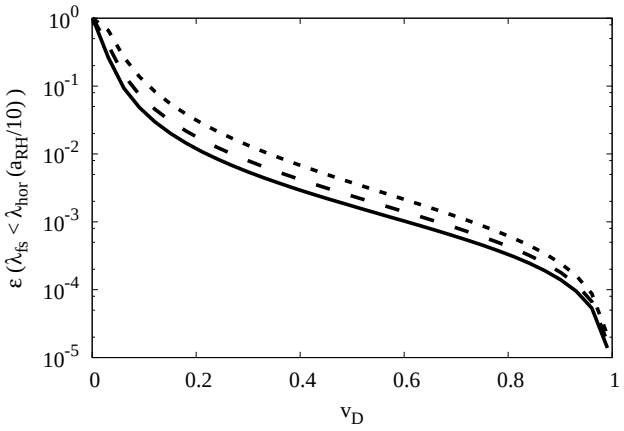

Figure 3.5: Fraction of dark matter whose free-streaming length is smaller than the scale of the perturbation mode that experiences a factor of 10 in growth during the EMDE as a function of the assumed dark matter velocity at production. The different lines represent values of $f = 10^{-7}$ (solid), 10^{-5} (dashed), and 10^{-3} (dotted), or equivalently, $T_{\rm RH} \simeq 3\gamma_D$ MeV, $T_{\rm RH} \simeq 0.03\gamma_D$ MeV, and $T_{\rm RH} \simeq 0.0003\gamma_D$ MeV, respectively, in order to produce the observed relic abundance of dark matter without annihilations.

by the horizon size at this time:

$$\lambda = \lambda_{\rm hor}|_{a_{\rm RH}/10} = \frac{1}{\frac{a_{\rm RH}}{10}\, H\left(\frac{a_{\rm RH}}{10}\right)}. \tag{3.23}$$

Any modes that enter the horizon prior to $0.1a_{\rm RH}$ will experience even more growth. The comoving free-streaming length of a dark matter particle born at a_D is given by

$$\lambda_{\rm fs} = \int_{a_D}^{a_0} v(a) \frac{da}{a^2 H(a)}, \tag{3.24}$$

where a_0 is the value of the scale factor today. Similar to our approach in the previous evaluation, there is a value of a_D for which the dark matter free-streaming length is less than the horizon size at $0.1a_{\rm RH}$ ($\lambda_{\rm fs} < \lambda_{\rm hor}|_{a_{\rm RH}/10}$).

The resulting fraction of dark matter that is born before this time, and thus that preserves a factor of 10 or more growth in perturbation amplitude, is shown in Fig. 3.5. The integral in Eq. (3.24) can be broken into three separate contributing integrals, representing the scalar-, radiation-, and matter-dominated eras (because the dark matter free-streaming length does not change significantly after matter-radiation equality, we neglect dark energy). The contribution coming from the radiation-dominated era is dependent on the duration of the era, which, in our formalism, is set by the relative abundance of dark matter and radiation following

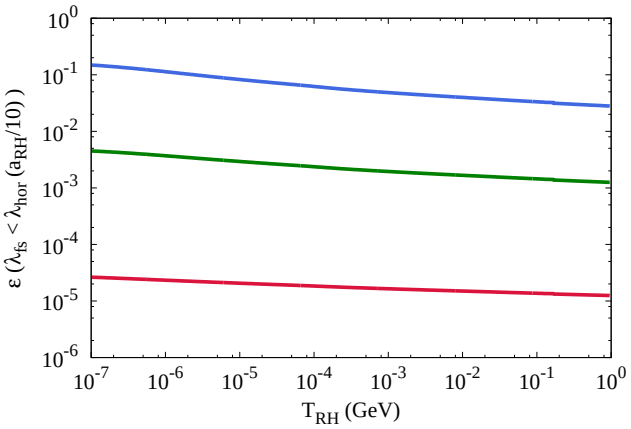

Figure 3.6: Fraction of dark matter whose free-streaming length is smaller than the scale of the perturbation mode that experiences a factor of 10 in growth during the EMDE as a function of the reheat temperature. The different lines represent, from top to bottom, values of $v_D = 0.1$, 0.5, and 0.99.

reheating, and this is directly related to the reheat temperature. The dependence on $T_{\rm RH}$, however, is only logarithmic and large variations in $T_{\rm RH}$ do not result in significant changes in the resulting fraction. Due to the interdependency discussed in Section 3.1 between the parameters f, $T_{\rm RH}$, and v_D required to obtain the appropriate dark matter abundance, we plot the fraction of dark matter able to preserve enhanced structure growth both as a function of v_D for various f in Fig. 3.5 and as a function of $T_{\rm RH}$ for various v_D in Fig. 3.6. Figure 3.6 shows how insensitive the fractional component of dark matter that experiences enhanced structure growth is to the reheat temperature.

Unfortunately, for dark matter particles born relativistically throughout an EMDE, the redshifting of their momentum is not enough to allow an appreciable fraction of the particles to participate in enhanced structure formation. Studies of mixed dark matter, in which there are both cold and warm dark matter components, show that the small-scale matter power spectrum is suppressed by 99% even when up to half of the dark matter is cold [114]. Therefore, the fraction of dark matter that is cold enough to benefit from the growth of perturbations during the EMDE is far too small for these structures to form.

3.3 Lyman-Alpha and MW Satellite Constraints

We have shown that the redshifting of the momentum of dark matter particles prior to reheating does not cool the dark matter enough to preserve the enhanced structure growth on scales that enter the horizon during the EMDE ($\lambda \lesssim 30$ pc for $T_{\rm RH} > 3$ MeV). In this section we consider if the dark matter is too hot, i.e. if its

free-streaming length large enough to prevent the formation of the smallest observed structures. Analysis of $\mathrm{Lyman}-\alpha$ data can be used to probe the matter power spectrum on small scales, $0.5\mathrm{Mpc}/h < \lambda < 20\mathrm{Mpc}/h$ [100, 101, 102], or $12.6h/\mathrm{Mpc} > k > 0.06h/\mathrm{Mpc}$, and we compare the degree of gravitational clustering at these scales in our model to that of the traditional model of cold dark matter. The existence of MW satellite galaxies provides another probe of small-scale structure formation. Suppression of the power spectrum leads to an underabundance of small structures, and the known abundance of substructures in the vicinity of the MW provides a bound on the allowed suppression [103].

3.3.1 Free-Streaming Length

We begin by calculating the physical streaming length today of a particle born at reheating:

$$\lambda_{\mathrm{fs},0}^{\mathrm{phys}} = a_0 \int_{a_{\mathrm{RH}}}^{a_0} v(a) \frac{da}{a^2 H(a)}. \tag{3.25}$$

The choice of $a_D = a_{\mathrm{RH}}$ is beneficial in that the fraction of dark matter born before reheating, found by our previous analysis of the distribution of birth times, is 0.51, and we can say that approximately half of the dark matter will have a free-streaming length above or below our calculated value. Another benefit of this choice is that our calculations of the free-streaming length are made simpler by neglecting the contribution to the free-streaming length coming from the EMDE.

Calculating the free-streaming length using Eq. (3.25) shows that $> 75\%$ of this distance is covered after the dark matter particle has become nonrelativistic, ($\gamma \leq 1.01$). For the highly relativistic initial velocities we would like to consider, the dark matter particles remain relativistic well after reheating, and are still relativistic after changes in the number of relativistic degrees of freedom have ceased. Beginning the integral in Eq. (3.25) at a_*, the value of the scale factor after which g_* remains constant, captures most ($\gtrsim 90\%$) of the free-streaming length and illuminates the important features of this scenario by allowing us to assume that $H \propto a^{-2}$ during radiation domination.

We begin by breaking the integral into two separate contributing integrals, representing the radiation- and matter-dominated eras (again we neglect dark energy) and introducing the variable $Y \equiv (\gamma_D v_D a_D)^2$. The free-streaming length is then

$$\lambda_{\rm fs} = \int_{a_*}^{a_0} \sqrt{\frac{Y}{Y+a^2}} \frac{da}{a^2 H(a)} \simeq \frac{1}{H_* a_*^2} \int_{a_*}^{a_{\rm eq}} \sqrt{\frac{Y}{Y+a^2}}\ da + \frac{1}{H_{\rm eq} a_{\rm eq}^{3/2}} \int_{a_{\rm eq}}^{a_0} \sqrt{\frac{Y}{Y+a^2}} \frac{da}{\sqrt{a}}$$
$$= \frac{\sqrt{Y}}{H_* a_*^2} \ln\left(\frac{a_{\rm eq} + \sqrt{Y + a_{\rm eq}^2}}{a_* + \sqrt{Y + a_*^2}}\right) + \frac{2\sqrt{i\sqrt{Y}}}{H_{\rm eq} a_{\rm eq}^{3/2}} F\left(i \sinh^{-1} \sqrt{\frac{i\sqrt{Y}}{a}}, -1\right)\Bigg|_{a_{\rm eq}}^{a_0}, \tag{3.26}$$

where $F(\phi, m)$ is the elliptic integral of the first kind. By choosing $a_D = a_{\rm RH}$ (contained in the variable Y), the first term in the above expression can be simplified under the assumption that $a_{\rm eq} \gg a_{\rm RH}$, which is reasonable considering that matter-radiation equality occurs at a temperature of $T_{\rm eq} \simeq 0.8$ eV and we require $T_{\rm RH} > 3$ MeV. The expression for the contribution to the physical free-streaming length today coming from the radiation-dominated era then simplifies to

$$\lambda_{\rm fs,0}^{\rm RD} \simeq \frac{\gamma_D v_D a_{\rm RH} a_0}{H_* a_*^2} \ln\left(\frac{a_{\rm eq}}{a_*} \frac{2}{1 + \sqrt{\left(\gamma_D v_D \frac{a_{\rm RH}}{a_*}\right)^2 + 1}}\right);$$
$$= \left(4.66 \times 10^{11} \text{pc}\right) \gamma_D v_D \frac{a_{\rm RH}}{a_0} \left[\ln\left(2\frac{T_*}{T_{\rm eq}}\right) - \ln\left(1 + \sqrt{\left(\gamma_D v_D \frac{a_{\rm RH}}{a_0}\right)^2 \left(\frac{T_*}{T_0}\right)^2 + 1}\right)\right], \tag{3.27}$$

where we have used the fact that g_* remains constant after $T_* = 2 \times 10^{-5}$ GeV to set $a_* T_* = a_{\rm eq} T_{\rm eq} = a_0 T_0$. An important feature of this calculation is that the parameters of our model, the dark matter velocity at its production and the reheat temperature, only enter into this expression through the combination

$$\mu \equiv \frac{\gamma_D v_D a_{\rm RH}}{a_0} = \gamma_D v_D \frac{T_0 g_{*S,0}^{1/3}}{3\left[T g_{*S}^{1/3}\right]_{T=0.34 T_{\rm RH}}}, \tag{3.28}$$

where g_{*S} is the number of relativistic degrees of freedom in the entropy density and again we assume entropy is conserved after $a = 3a_{\rm RH}$. Expressed in terms of the variable μ, the physical free-streaming length

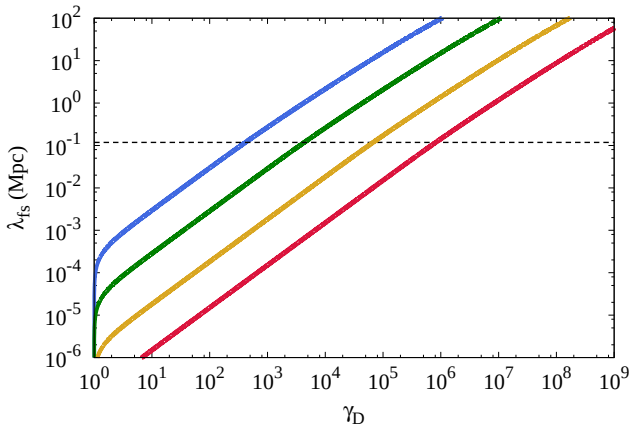

Figure 3.7: The free-streaming length of the dark matter as calculated by Eq. (3.29) as a function of the Lorentz factor at decay, γ_D, for (left to right) $T_{\rm RH} = (3, 30, 300, 3000)$ MeV. The horizontal dashed line marks $\lambda_{\rm fs,0}^{\rm phys} \gtrsim 0.08\ {\rm Mpc}/h$, approximately the lower limit to scales probed by ${\rm Lyman}-\alpha$ observations.

calculated from the contribution from both the radiation- and matter-dominated eras is

$$\lambda_{\rm fs,0}^{\rm phys} = \left(4.66\times10^5{\rm Mpc}\right)\mu\left[\ln\left(2\frac{T_*}{T_{\rm eq}}\right) - \ln\left(1+\sqrt{\mu^2\left(\frac{T_*}{T_0}\right)^2+1}\right)\right] + \left(4.66\times10^5{\rm Mpc}\right)\sqrt{\frac{T_0}{T_{\rm eq}}}\sqrt{2i\mu}\left[F\left(i\sinh^{-1}\sqrt{i\mu}\right) - F\left(i\sinh^{-1}\sqrt{i\mu\frac{T_{\rm eq}}{T_0}}\right)\right]. \quad (3.29)$$

The above equation gives the scale at which the power spectrum of our model begins to differ from that of the standard ΛCDM power spectrum. Figure 3.7 shows the free-streaming length calculated by Eq. (3.29) as a function of the Lorentz factor at decay, γ_D, for different values of the reheat temperature. We define $k_{\rm fs} = (\lambda_{\rm fs,0}^{\rm phys})^{-1}$, and above the horizontal dashed line, the free-streaming length of the dark matter reaches scales probable by the ${\rm Lyman}-\alpha$ forest: $k \lesssim 12.6\ h/{\rm Mpc}, \lambda_{\rm fs,0}^{\rm phys} \gtrsim 0.08\ {\rm Mpc}/h$. Since the free-streaming lengths of our model enter the observable regime, we consider a more precise determination of the effects of the dark matter free-streaming length in the next section.

3.3.2 Transfer Function

We use the Cosmic Linear Anisotropy Solving System (CLASS) [115] to obtain the dark matter transfer function,

$$T^2(k) \equiv \frac{P_{\rm nCDM}(k)}{P_{\rm CDM}(k)}, \tag{3.30}$$

which describes suppression of structure due to non-cold dark matter (nCDM) compared to that of the standard CDM scenario; $P_{\rm nCDM}(k)$ and $P_{\rm CDM}(k)$ are the matter power spectra in each respective case.

Acquiring the power spectrum for our scenario requires us to determine the momentum distribution function of our dark matter model. Shortly after reheating ($a \sim 3a_{\rm RH}$), the scalar field has decayed almost entirely, and essentially no new dark matter particles are being produced. After this point, the distribution of the comoving momenta of the dark matter particles does not change. We scale the comoving momenta of the dark matter particles by the comoving momentum of a particle born at the scale factor that maximizes $f(a_D)$, $a_{\rm max} = 0.68 a_{\rm RH}$, and express our distribution function in terms of

$$q \equiv \frac{ap}{a_{\rm max} p_D} = \frac{a_D}{a_{\rm max}}, \tag{3.31}$$

where p_D is the physical momentum of a particle with velocity v_D. Since we assume that all dark matter particles are produced with the same velocity, the distribution in momentum for particles in our scenario can be entirely determined from the distribution in the particles' scale factor at production, which we have already determined. The two distribution functions can be related through

$$4\pi q^2 f(q) = f(a_D)\frac{da_D}{dq} = 0.68\ f\left(\frac{a_D}{a_{\rm RH}}\right). \tag{3.32}$$

This distribution function is shown in Fig. 3.8, and we also show for comparison the Fermi-Dirac distribution that is maximized at $q = 1$. We can see that, compared to the thermal case, we have a broader distribution function.

With our distribution function $f(q)$, we are able to use CLASS to obtain transfer functions for any combination of the velocity imparted to the dark matter and the reheat temperature by also providing the

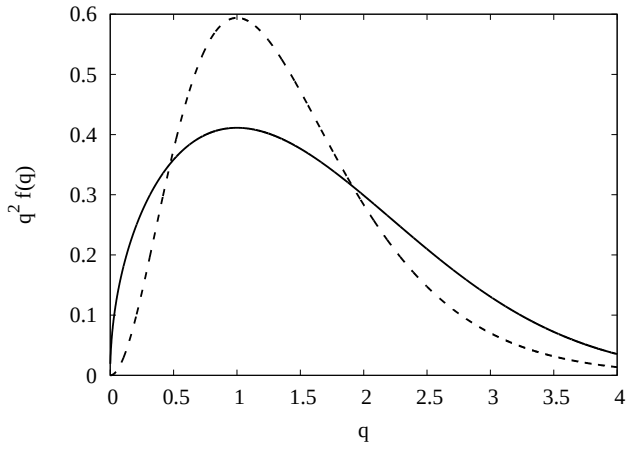

Figure 3.8: The distribution function of dark matter for our model (solid) and a Fermi-Dirac distribution (dashed) for comparison, for relativistic particles, as would be expected in scenarios of WDM.

present-day physical momentum of a dark matter particle with $q = 1$:

$$p_0 = \frac{a_{\rm max} p_D}{a_0} \propto \frac{a_{\rm RH} \gamma_D v_D}{a_0}. \tag{3.33}$$

Again we find that, just as in our calculations of the free-streaming length, the relevant combination of parameters is $\mu = \gamma_D v_D a_{\rm RH}/a_0$. In Figs. 3.9 and 3.10 we show the transfer functions for dark matter produced at different velocities, but in scenarios with the same reheat temperature, 3 MeV. As expected, dark matter particles born at greater velocities result in the suppression of larger scales (smaller k). The vertical dashed lines in Fig. 3.9 mark the free-streaming horizon $k_{\rm fs} = (\lambda_{\rm fs,0}^{\rm phys})^{-1}$ given by Eq. (3.29) for each of the different velocities at production, confirming that it is the scale at which our model begins to show deviation, $T(k) \simeq 0.95$, from the CDM scenario.

Transfer functions in nCDM models, such as this, can be well described by a fitting formula [116]:

$$T(k) = [1 + (\alpha k)^\beta]^\gamma. \tag{3.34}$$

Using $\rm Lyman{-}\alpha$ data, the fitting parameters α, β, and γ can be constrained [116, 117], and the parameters of our model, v_D and $T_{\rm RH}$, can be constrained as well. The typical scale of the suppression is set by α, whereas the general shape is determined by β and γ. When fitting our transfer function at values $T(k) > 0.01$, the overall shape of our transfer function varies little across wide ranges of our parameter space, and β and γ can

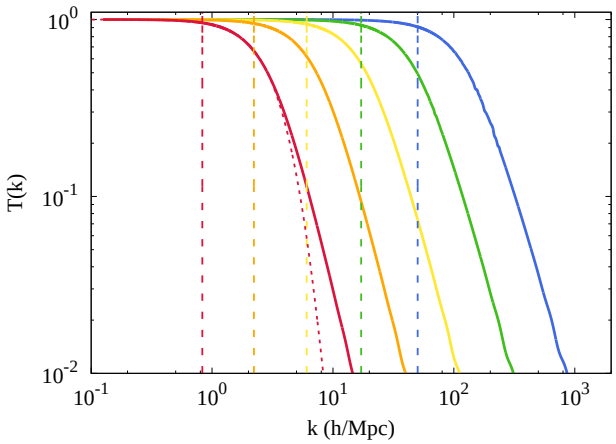

Figure 3.9: The transfer function for several values of the dark matter velocity at production, v_D. Right to left (cool to warm colors), the solid lines represent dark matter produced with increasing Lorentz factor $\gamma_D = 100, 300, 900, 2700, 8100$, respectively. In all cases $T_{\rm RH} = 3$ MeV. Vertical dashed lines represent the scale of the free-streaming horizon calculated using Eq. (3.29). The red dotted line represents the typical transfer function for dark matter with a thermal distribution ($\beta_{\rm WDM} = 2.24$ and $\gamma_{\rm WDM} = -4.46$) with a cutoff parameter $\alpha_{\rm WDM} \simeq 0.16$ Mpc$/h$ in order to match the same half-mode scale $k_{\rm hm}$ as our far left curve with $\alpha = 0.31$ Mpc$/h$.

be expressed as functions of α, as seen in Fig. 3.11. The cutoff parameter α is then our only free parameter, and it can be robustly constrained using $\mathrm{Lyman}-\alpha$ data.

We find typical values of β and γ for our model to be approximately 2.4 and -1.1 respectively, for α near the constrainable regime. These values are noticeably different from those that describe the thermal warm dark matter (WDM) transfer function, $\beta_{\rm WDM} = 2.24$ and $\gamma_{\rm WDM} = -4.46$. If we compare our transfer functions to those of WDM with the same value of the half-mode scale[2] $k_{\rm hm}$, we can see in Figs. 3.9 and 3.10 that the transfer functions in the two models are quite similar. However, due to the difference in the shape parameters of the transfer function fit between the two models, matching their half-mode scales requires the cutoff parameter in the WDM transfer function to be roughly a factor of 2 smaller than that in the corresponding nonthermal transfer function, $\alpha \simeq 2\alpha_{\rm WDM}$. The cutoff in the transfer function of our model is not as sharp as that of WDM, but they only begin to differ significantly at scales at which the power in the nCDM model is already greatly suppressed, $T(k) \lesssim 0.1$.

Reference [117] provided marginalized bounds on all three fitting parameters in Eq. (3.34). The predictable shape of our transfer function determines the values of β and γ as a function of α, as shown

[2]We follow the convention of Ref. [118] and define the half-mode scale via $T(k_{\rm hm}) = 0.5$, noting that this convention is different from the half-mode scale, $k_{1/2}$, defined in Refs. [116] and [117], for which $T^2(k_{1/2}) = 0.5$.

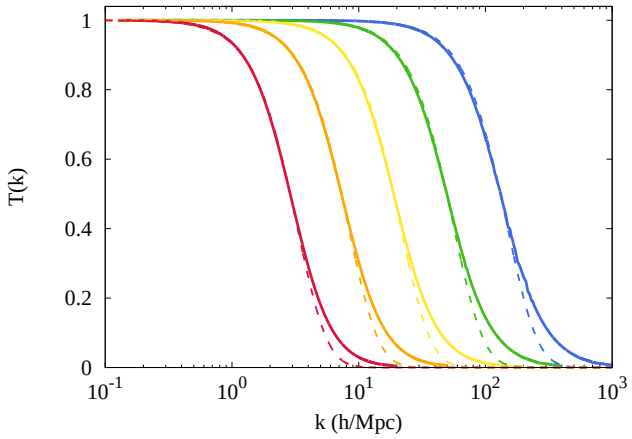

Figure 3.10: The solid lines show the same transfer functions shown in Fig. 3.9. Dashed lines show the thermal WDM transfer functions with matched half-mode scales. Due to the difference in the shape parameters β and γ in the fitting form of Eq. (3.34) between the two models, matching the half-mode scales requires the cutoff parameters, α, to be related by approximately $\alpha \simeq 2\alpha_{\rm WDM}$

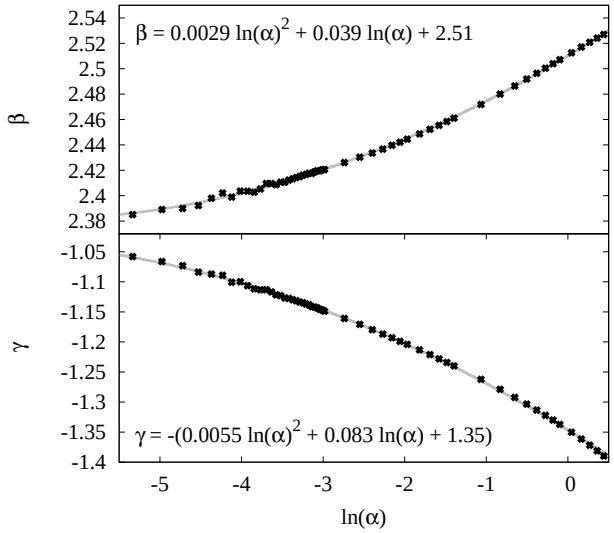

Figure 3.11: The fitted values for the parameters β and γ for transfer functions whose cutoff parameters, α, span from 0.005 to 1.5 Mpc$/h$. In the fitting functions for β and γ, α has units of Mpc$/h$.

in Fig. 3.11, and allows us to obtain a bound on the remaining free parameter, the scale of the cutoff: $\alpha < 0.011\mathrm{Mpc}/h$ (68% C.L.) and $\alpha < 0.026\mathrm{Mpc}/h$ (95% C.L.). Following Ref. [117], these limits have been obtained by performing a comprehensive Markov Chain Monte Carlo (MCMC) analysis of the full parameter space affecting the one-dimensional flux power spectrum, which is the Lyman-α forest physical observable, with a data set consisting of the high-resolution and high-redshift ($4.2 < z < 5.4$) quasar samples from MIKE and HIRES spectrographs [119]. The flux power spectra to be compared against observations are estimated by interpolating in the multidimensional space defined by the sparse grid of precomputed hydrodynamic simulations described in Ref. [117]. Whenever some of the parameters assume values not enclosed by the template of simulations, the corresponding values of the power spectra are linearly extrapolated.

As in the reference analysis from Ref. [117] (but see also, e.g., Refs. [120] and [121]), the other cosmological and astrophysical parameters impacting our likelihood are treated as nuisance parameters to marginalize over. We adopt conservative flat priors on both σ_8, i.e. the normalization of the linear matter power spectrum, and n_{eff}, i.e. the slope of the matter power spectrum at the scale of the Lyman-α forest ($k \sim 1h/\mathrm{Mpc}$), in the intervals $[0.5, 1.5]$ and $[-2.6, -2.0]$, respectively; and on the instantaneous reionization redshift z_{reio} (in the range $[7, 15]$). Concerning the astrophysical parameters, we model the redshift evolution of the temperature of the intergalactic medium as a power law, imposing flat priors on both its amplitude and tilt (once again, see Ref. [117] for further details). Finally, we adopt conservative Gaussian priors on the mean Lyman-α forest fluxes $\langle F(z) \rangle$, with standard deviation $\sigma = 0.04$ [102], and a flat prior on f_{UV}, which is an effective parameter accounting for spatial ultraviolet fluctuations in the ionizing background.

Last but not least, we adopt a flat prior on α in the interval [0, 0.1] Mpc$/h$, while the parameters β and γ are derived analytically, per each MCMC step, according to the expressions reported in Fig. 3.11. For further details on the data set, simulations, and methods that we have used, we address the reader to any of the aforementioned references [117, 120, 121].

For comparison, just as matching the half-mode scale of the thermal WDM transfer function with that of our nonthermal model requires $\alpha \simeq 2\alpha_{\mathrm{WDM}}$, the α_{WDM} value of a 3 keV WDM particle, $\alpha_{\mathrm{WDM}} \simeq 0.015\mathrm{Mpc}/h$ [117], is approximately a factor of 2 smaller than that of our 95% C.L. bound on α. Our limits on γ_D and T_{RH} corresponding to our 68% and 95% C.L. bounds on α are shown in Fig. 3.12. Scenarios in which the dark matter is born at too high of a velocity (large γ_D) or in which the radiation-dominated era is too short (low T_{RH}) are part of the excluded parameter space for our relativistic nonthermal dark matter

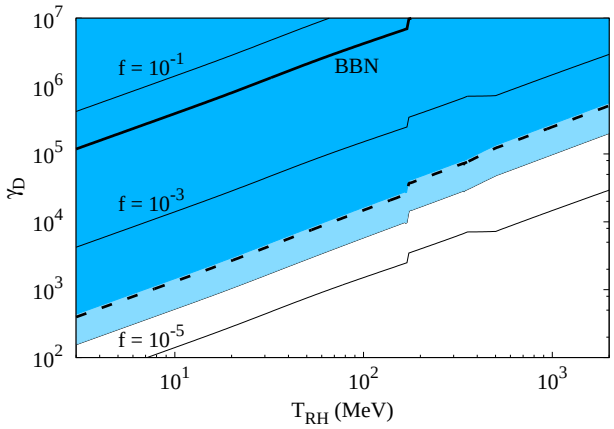

Figure 3.12: Limits on the Lorentz factor γ_D and the reheat temperature. The shaded regions correspond to the 1σ and 2σ bounds, $\alpha = 0.011\mathrm{Mpc}/h$ and $0.026\mathrm{Mpc}/h$, respectively. The thick dashed line represents $k_{\rm fs} = (\lambda_{\rm fs})^{-1} = 12.6h/\mathrm{Mpc}$ as calculated by Eq. (3.29). The discontinuity at $T_{\rm RH} \simeq 170\mathrm{MeV}$ occurs due to the sudden change in g_* during the QCD phase transition. Thin solid lines show the contours of f required to obtain the observed dark matter abundance in the absence of annihilations. The thick solid line shows the bound on γ_D as a function of $T_{\rm RH}$ imposed by BBN, derived in Section 3.1.1.

model. The thin grey lines represent contours of constant f, the fraction of the scalar's energy imparted to the dark matter particle that is required to obtain the correct relic abundance for a given reheat temperature without dark matter annihilations. We can see that, in the absence of annihilations, the allowed values of γ_D are not large enough for the required value of f to be of order unity.

We also show the outline (dashed) of the parameter space in which the free-streaming length, calculated by Eq. (3.29), is naively probable by Lyman-α data, i.e. $k_{\rm fs} < 12.6h/\mathrm{Mpc}$. As can be seen in Fig. 3.12, limiting the free-streaming length provides a bound that is comparable to those obtained from the full consideration of effects to the matter power spectrum; the free-streaming scales of a particle on the boundary of our 68% and 95% C.L. regions are $k_{\rm fs} = 11.4h/\mathrm{Mpc}$ and $28h/\mathrm{Mpc}$, respectively. While examining effects on the matter power spectrum leads to more robust bounds within our parameter space, calculations of the free-streaming length are more readily performed. Fortunately, as both the free-streaming length and the dark matter distribution function depend on the same combination of our parameters, $\gamma_D v_D a_{\rm RH}/a_0$, there is a simple relationship between the scale of suppression, α, and the free-streaming length calculated by Eq. (3.29):

$$\alpha \simeq 0.177 \left(\frac{\lambda_{\rm fs,0}^{\rm phys}}{\mathrm{Mpc}} \right)^{0.908} \frac{\mathrm{Mpc}}{h} \tag{3.35}$$

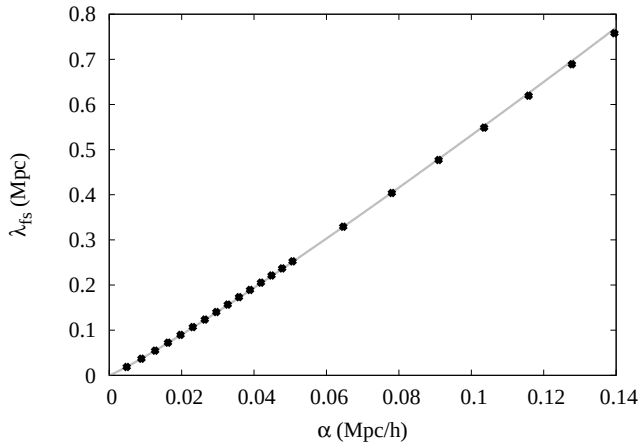

Figure 3.13: A plot of the relationship between the fitting parameter α and the free-streaming length as calculated by Eq. (3.29). Black dots represent points for which we have used our model parameters to calculate the free-streaming length and obtain the transfer function using CLASS. The grey line shows the fit to the data given by Eq. (3.35).

We show this relationship in Fig. 3.13. In our model, the bounds on α can be easily used to limit the free-streaming length, and thereby the parameters γ_D and $T_{\rm RH}$ on which it depends.

3.3.3 Milky-Way Satellites

In addition to structures inferred by Lyman-α data, we can also constrain our model using observed structures in the Milky Way. Simulations of thermal warm dark matter provide an indication of how the suppression expected in the matter power spectrum decreases the abundance of collapsed objects. The subhalo mass function in simulations with WDM characterizes this underabundance [122],

$$\left.\frac{dN}{dM}\right|_{\rm WDM} = \left.\frac{dN}{dM}\right|_{\rm CDM} \left(1 + \delta \frac{M_{\rm hm}}{M}\right)^{-\varepsilon}, \tag{3.36}$$

where M is the subhalo mass, $\delta = 2.7$ and $\varepsilon = 0.99$, and $M_{\rm hm}$ is the mass scale associated with the half-mode scale[3]:

$$M_{\rm hm} = \frac{4\pi}{3} \Omega_{\rm DM}\, \rho_{\rm crit,0} \left(\frac{\pi}{k_{\rm hm}}\right)^3, \tag{3.37}$$

where $\Omega_{\rm DM}$ is the fraction of the critical density in dark matter.

[3]We have verified with the authors of Ref. [122] that they used the same definition of $k_{\rm hm}$ that we have presented here.

Knowing the abundance of satellites of our own galaxy, constraints can be placed on the amount of allowed suppression in the subhalo mass function. Using a probabilistic analysis of the MW satellite population and marginalizing over astrophysical uncertainties, Ref. [103] found an upper limit on $M_{\rm hm}$ in Eq. (3.36), $M_{\rm hm} < 3.1 \times 10^8 M_\odot$ (95% C.L.), which implies that the half-mode scale must satisfy $k_{\rm hm} > 36h/{\rm Mpc}$. This bound on $k_{\rm hm}$ can be used to constrain any dark matter model that has a transfer function comparable to WDM, as we have shown ours to be in Fig. 3.10. Though the transfer function of our model does differ slightly from that of WDM, the differences occur only when the nCDM power spectrum is already greatly suppressed compared to that of CDM, $T(k) \lesssim 0.1$. The fitting form to our transfer function, Eq. (3.34), implies that the half-mode scale is given by:

$$k_{\rm hm} = \frac{1}{\alpha}\left[\left(\frac{1}{2}\right)^{1/\gamma} - 1\right]^{1/\beta}, \tag{3.38}$$

and the constraint $k_{\rm hm} > 36\ h/{\rm Mpc}$ directly translates to $\alpha < 0.026\ {\rm Mpc}/h$, matching our 95% C.L. bound from Lyman-α constraints.

3.4 Discussion

The inclusion of a period of effective matter domination between inflation and BBN is an amply motivated alternative to the standard thermal history of the Universe. If dark matter is produced nonthermally during this era, the viable parameter space for the dark matter annihilation cross section widens greatly, as large ranges of production and annihilation efficiencies can combine to result in the correct relic abundance.

Nonstandard thermal histories could potentially have observable consequences. Unlike the typically assumed period of radiation domination following inflation, in which subhorizon density perturbations grow logarithmically, EMDEs provide an era of linear growth. Linear growth would enhance structure formation on scales that enter the horizon during this era, possibly leading to observable effects. However, in the absence of fine-tuning, it is likely that dark matter produced nonthermally will be imparted with relativistic velocities, and its subsequently large free-streaming length will wipe out this enhancement to structure formation.

By investigating the velocity evolution and distribution of dark matter produced nonthermally from the decay of a massive scalar field, we have confirmed that retaining the linear enhancement to structure growth requires the dark matter to be produced largely nonrelativistic. Despite the early creation of many particles, and their loss of momentum due to adiabatic cooling, the continuous creation of new, hot particles prevents

the average dark matter velocity from decreasing appreciably during the EMDE. The average particle at reheating is nearly as relativistic as those newly produced from decay. And because a majority of the dark matter is created around reheating, essentially negligible fractions of dark matter particles have velocities low enough to preserve enhanced structure formation.

We next investigated the upper limit on the dark matter velocity required to preserve the structures we observe. Dark matter particles born with relativistic velocities have free-streaming lengths that may also washout observed small-scale structures. $\mathrm{Lyman}-\alpha$ forest data provides the best-known probes of inhomogeneity at small scales, and ensuring that structure formation at these scales is not observably suppressed constrains the parameter space of nonthermal dark matter.

Using the software CLASS, we obtained the matter power spectrum resulting from our model of nonthermal dark matter. A transfer function was used to compare our spectrum to that of the standard CDM scenario and showed a cutoff in the power at small scales in our nonthermal scenario similar to that due to WDM. We fit the form of our transfer functions using three free parameters, one of which, α describes the scale of the cutoff in the transfer function and the other two describe its overall shape. The shape of our transfer function varies slightly with the cutoff scale and the two parameters describing its shape are well determined by analytic functions of α.

We obtained limits on the allowed scale of the cutoff in the transfer function by performing a comprehensive MCMC analysis using $\mathrm{Lyman}-\alpha$ observations: $\alpha < 0.011\mathrm{Mpc}/h$ (68% C.L.) and $\alpha < 0.026\mathrm{Mpc}/h$ (95% C.L.). From this constraint, we were able to place limits on the allowed velocity imparted at scalar decay for a given temperature at reheating, summarized in Fig. 3.12. We also found a simple relation between α and the dark matter free-streaming length that allows one to use the limits on α to limit the free-streaming length which can be calculated analytically from γ_D and T_{RH}.

Observations of the abundance of MW satellite galaxies provide another probe of the small-scale power spectrum. Using the halo-mass function obtained from WDM simulations, limits on the cutoff scale can also be placed on the WDM transfer function by requiring consistency between the decreased abundance of collapsed objects expected in WDM scenarios, compared to CDM, and the abundance of satellites observed orbiting the MW. These constraints are applicable to any model of dark matter with a transfer function comparable to that of WDM. Comparison of the parameter values that fit the transfer function of our model to those that fit WDM naively imply marked differences between the two models; however, matching the transfer functions at the same half-mode scale shows the two models to be remarkably similar, differing

significantly only on scales at which the power was already greatly suppressed. In our model, MW satellite considerations provide a practically identical bound on α to those of Lyman-α data.

Using the impact on the matter power spectrum expected in the model of nonthermal dark matter we have presented here, we have constrained the physical parameters of our model: the velocity imparted at the dark matter production, characterized by the Lorentz factor γ_D, and the temperature at reheating, $T_{\rm RH}$. Constraints in this parameter space also inform the allowed value of f, the fraction of the decaying component's energy allocated to the dark matter, that is required to obtain the correct relic abundance in the absence of dark matter annihilations. While naturalness would suggest a value of $f \sim 0.5$, our constraints show that f must be less than $\sim 10^{-4}$, implying that annihilations must be considered to avoid finely tuning f. Our limits within the parameter space of $T_{\rm RH}$ and γ_D can also be equivalently viewed as limits on the scalar decay rate Γ_ϕ [see Eq. (3.1)] and the mass hierarchy between the scalar parent and daughter dark matter particles for a two-body decay ($m_\phi = 2\gamma_D m_\chi$).

There are many opportunities for extensions to our model. We have assumed here that all dark matter particles are born from the decay process with the same velocity, though this need not necessarily be the case. Including a range of possible velocities could tighten or relax our bounds, depending on the exact distribution of the imparted velocity. We have also assumed that any annihilations take place via s-wave processes. If annihilations occur preferentially for faster particles, this could shift the peak of our velocity distribution to lower velocities. Finally, we have only considered the cooling of dark matter due to the redshifting of its momentum. If dark matter is allowed to exchange momentum with Standard Model particles, this could provide an additional mechanism to reduce its momentum and lower the peak velocity of the velocity distribution, perhaps allowing for the formation of microhalos from perturbations that grow linearly during the EMDE. It is this final consideration that we investigate in the next chapter.

CHAPTER 4

Interacting Dark Matter: Impact of Nonthermal Production on the Matter Power Spectrum

As we just saw in Chapter 3, the redshifting of its momentum is insufficient to cool the dark matter enough to allow the preservation of structures formed during the EMDE. We now investigate how effective scattering interactions with the SM could be at further reducing the dark matter velocity. The relatively heavy dark matter particle is born from the decay of the scalar with a large momentum, and through many interactions with SM particles that each change the particle's momentum by a small amount, the dark matter can be brought into kinetic equilibrium with the SM. Once a dark matter particle is coupled to the SM radiation, its momentum will actually decrease slower than a^{-1}, because the SM radiation is continually heated by the decay of the scalar field. This means that, even though scattering can rapidly reduce a dark matter particle's momentum initially after production, for the few earliest born particles which would have redshifted as a^{-1} during the entire EMDE, the end effect of scattering can be to increase their momenta at reheating compared to the noninteracting case. However, if the dark matter is still coupled to the SM particles near the time of reheating, for the large majority of particles born near reheating, their momenta will experience the initial rapid decrease after their production, and their momenta following reheating will be greatly reduced. If the dark matter remains coupled to the SM until after reheating and after production has ceased, its velocity distribution would be indistinguishable from the thermal dark matter scenario. For an appreciable effect to the dark matter velocity distribution, kinetic decoupling must occur near reheating, and we investigate how appreciable this effect can be.

4.1 Interacting Nonthermal Dark Matter

When considering scattering interactions between the dark matter and SM particles, we are interested in the momentum transfer rate between the two sectors. This momentum transfer rate will depend on both the collision rate between dark matter and SM particles and the momentum exchanged in each collision. The collision rate can be given by $\Gamma_{\rm coll} = \langle \sigma_{\rm sc} v \rangle n_r$, where n_r is the number density of relativistic SM particles,

which scales with the radiation temperature as $n_r \propto T^3$, and $\langle \sigma_{\rm sc} v \rangle$ is the velocity-averaged scattering cross section between the dark matter and SM particles. The scattering cross section scales with the radiation temperature differently depending on the dominant scattering channel. For example, for p-wave scattering, the cross section exhibits a $\langle \sigma_{\rm sc} v \rangle \propto T^2$ behavior; we can remain agnostic about the dark matter scattering channel, however, and use the general expression $\langle \sigma_{\rm sc} v \rangle \propto T^n$. Because our dark matter particle is much heavier than the SM particles, each collision will only alter the dark matter particle's momentum by a small amount. In a nonrelativistic treatment, it requires approximately m_χ/T collisions in order to appreciably change a particle's momentum, and the momentum transfer rate will be suppressed relative to the collision rate by a factor of T/m_χ [123]. We will use this approximation to define the momentum transfer rate between the dark matter and SM to be

$$\Sigma \equiv \sigma \left(\frac{T}{T_i} \right)^{4+n}, \tag{4.1}$$

where $T_i = T(a_i)$, and $\sigma = \Sigma(T_i)$. As in previous sections we introduce the dimensionless variable $\tilde{\sigma} \equiv \sigma / H_i$.

The kinetic decoupling of dark matter from the SM radiation occurs when the momentum transfer rate falls below the expansion rate, thus we define the kinetic decoupling temperature, $T_{\rm kd}$, by $\Sigma(T_{\rm kd}) = H(T_{\rm kd})$. Using our momentum transfer rate, we can write an equation for the evolution of the momentum, p, of a single dark matter particle interacting with the SM plasma;

$$\frac{dp}{dt} = -Hp - \Sigma(p - p_{\rm f}) \tag{4.2}$$

where $p_{\rm f}$, the momentum "floor", is the average momentum to which the dark matter equilibrates and depends on the temperature of the SM radiation. We define the temperature of our dark matter to be $T_\chi = (2/3)(\langle p^2 \rangle / 2m_\chi)$ [123]. Thus, when dark matter and the SM are in equilibrium, the dark matter is kept at an average momentum $p_{\rm f} = \sqrt{3 m_\chi T}$. The quantity of interest for much of our analysis, however, will be the dark matter velocity given by $\gamma v = p/m_\chi$. The velocity a dark matter particle maintains while in equilibrium with the SM radiation, $\gamma v = p_{\rm f}/m_\chi = \sqrt{3T/m_\chi}$, will determine its velocity, and thus free-streaming length, following reheating. For a given relation between the time of decoupling and reheating (for a given value of $a_{\rm kd}/a_{\rm RH}$), the momentum following reheating of a dark matter particle that coupled to

the SM radiation will be related to the the value of the momentum floor at which it decoupled, which itself can be related the to momentum floor at reheating for a fixed $a_{\rm kd}/a_{\rm RH}$. The velocity of a dark matter particle following reheating will then depend on the quantity $p_{\rm f,RH}/m_\chi \propto \sqrt{T_{\rm RH}/m_\chi}$. Increasing the temperature at reheating will increase the temperature of the radiation bath throughout the EMDE, and it will increase the velocity of particles that experience coupling. Meanwhile, increasing the dark matter mass, while keeping the momentum to which it couples fixed, implies a decreased dark matter velocity.

Figure 4.1 shows the evolution of the momentum of a 10 GeV dark matter particle produced at a_i for various values of $\tilde{\sigma}$ and a reheat temperature of 3 MeV. For simplicity, we neglect changes in the relativistic degrees of freedom, g_*, prior to $3a_{\rm RH}$. The solid black line shows the momentum of the particle in the absence of interactions. For large enough $\tilde{\sigma}$ dark matter particle's momentum is quickly brought down to the floor, lower than it would other wise be without interactions, but the redshifting behavior of the momentum floor to which it couples ($p_{\rm f} \propto a^{-3/16}$) is much slower than the momentum of a particle with no interactions ($p \propto a^{-1}$). A coupled dark matter particle maintains a much higher momentum during the EMDE than a non-interacting particle. Particles that also decouple during the EMDE not only begin at this higher momentum but can also experience a redshift behavior in their momentum slower than $p \propto a^{-1}$ as well. In Figure 4.1, we already see the hints of this strange behavior; even after the particle has decoupled from the radiation, its momentum does not quite scale as a^{-1}.

To understand this strange behavior, we first rewrite Eq. (4.2) as

$$a\frac{dp}{da} + p\left[1 + \frac{\Sigma}{H}\right] = \frac{\Sigma}{H}p_{\rm f}, \tag{4.3}$$

and examine it in the regime long after kinetic decoupling ($a \gg a_{\rm kd}$), when $\frac{\Sigma}{H} \ll 1$:

$$a\frac{dp^{\rm akd}}{da} + p^{\rm akd} \simeq \frac{\Sigma}{H}p_{\rm f}. \tag{4.4}$$

During the EMDE, $T(a) = T_{\rm kd}(a_{\rm kd}/a)^{3/8}$ and $(\Sigma/H) = (a_{\rm kd}/a)^{3n/8}$, in the absence of changes in the number of relativistic degrees of freedom, where $a_{\rm kd}$ is the scale factor at which $\Sigma = H$. Performing the change of variables

$$h(a) = \left(\frac{a}{a_{\rm kd}}\right)p^{\rm akd} \quad \text{and} \quad y = \frac{a}{a_{\rm kd}}, \tag{4.5}$$

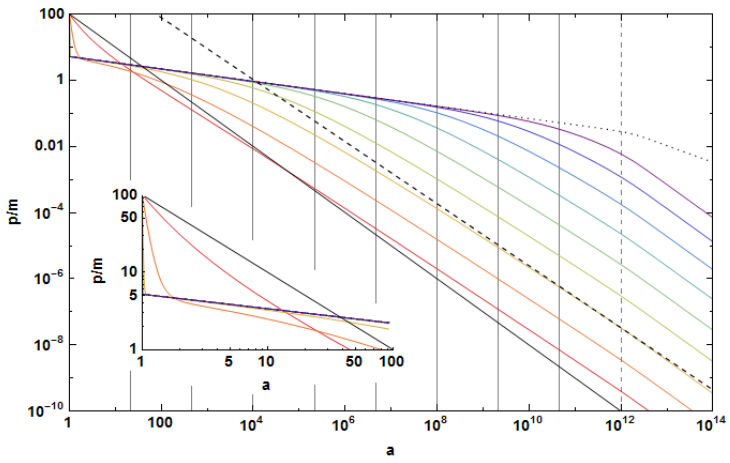

Figure 4.1: The evolution of γv as a function of scale factor for a dark matter particle born at a_i with $\gamma_D = 100$ for $\tilde{\sigma} = 10^{0,1,2,...8}$ (red - purple). Also shown shown is the momentum "floor" $p_{\rm f}$ (black, dotted), the momentum of a particle under no interactions $p(a) = \gamma_D v_D (a_i/a)$ (black, solid), and $p_{\rm RH}(a_{\rm RH}/a)^{15/16}$ (black, dashed) to show that, even after the dark matter has decoupled from the radiation, it does not redshift as $p \propto a^{-1}$. Here $\tilde{\Gamma}_\phi = 10^{-18}$, $n = 2$, $m_\chi = 10$ GeV, and $T_{\rm RH} = 3$ MeV. The scale factor at decoupling, $a_{\rm kd}$, is marked for each case of $\tilde{\sigma}$ by solid vertical lines, with decoupling in the $\tilde{\sigma} = 10^0$ case occurring at $a_{\rm kd} = 1$ and coinciding with the y-axis. The dashed vertical line denotes reheating. Inset: Behavior at very early times showing that, with a large enough value of $\tilde{\sigma}$ ($\gtrsim 10^2$), dark matter couples very quickly to the SM radiation.

and noting that $p_{\rm f} = p_{\rm f,kd}(a_{\rm kd}/a)^{3/16}$ during the EMDE, Eq. (4.4) becomes

$$\frac{dh}{dy} = p_{\rm f,kd}\, y^{(3/8)(n+1/2)}. \tag{4.6}$$

Eq. (4.6) can be solved analytically, and the evolution of the momentum of a dark matter particle long after kinetic decoupling, but sufficiently before reheating, is given by:

$$p^{\rm akd} = C\frac{a_{\rm kd}}{a} + \frac{p_{\rm f,kd}}{1-(3/8)(n+1/2)}\left(\frac{a_{\rm kd}}{a}\right)^{(3/8)(n+1/2)}, \tag{4.7}$$

where C is a constant of integration. For $n \leq 2$ we have that $(3/8)(n+1/2) < 1$, thus the second term in Eq. (4.7) falls off slower than a^{-1} and can come to dominate when $a \gg a_{\rm kd}$. For $n = 2$, as we had in Figure 4.1, the second term scales as $a^{-15/16}$ and dominates the late-time behavior of the particle's momentum, which we highlight by the dashed line.

For a particle which couples very quickly to the SM radiation, the general solution to Eq. (4.2) is

$$p(s) = p_{\rm f} s^{\lambda} e^{s} \Gamma(1-\lambda, s), \tag{4.8}$$

where $s(a) = (8/3n)(a_{\rm kd}/a)^{3n/8}$, $\lambda = 13/(6n)$ during the EMDE, and $\Gamma(x, s)$ is the upper incomplete gamma function. We can use this general solution to determine our integration constant in Eq. (4.7). Long after decoupling, when $a \gg a_{\rm kd}$, the incomplete gamma function behaves as

$$\lim_{s\to 0}\Gamma(1-\lambda, s) = \Gamma(1-\lambda) - \frac{s^{1-\lambda}}{1-\lambda} + \ldots, \tag{4.9}$$

and at late times the solution to Eq. (4.8) becomes

$$p^{\rm akd} = \left[p_{\rm f,kd} \left(\frac{8}{3n}\right)^{13/12} \Gamma(1-\lambda) \right] \frac{a_{\rm kd}}{a} + \frac{p_{\rm f,kd}}{1-(3/8)(n+1/2)} \left(\frac{a_{\rm kd}}{a}\right)^{(3/8)(n+1/2)}. \tag{4.10}$$

All particles produced sufficiently before $a_{\rm kd}$ will follow Eq. (4.10) up until reheating, when we can no longer assume $T \propto a^{3/8}$; after reheating their momentum will begin scaling as $p \propto a^{-1}$, as can be seen in Figure 4.2. Particles born sufficiently after $a_{\rm kd}$ will have never coupled to the radiation and so their momentum will follow the usual a^{-1} scaling. Thus, at reheating there will be a large number of particles that, though born at different times, were able to couple to the radiation and all decoupled at the same time. Thereafter, all the particles born before kinetic decoupling maintain approximately the same momentum. Particles born later will have momenta at reheating that depend on the scale factor at which they were produced, similar to our earlier analysis.

Our analysis in the previous chapter also tells us that most of the dark matter particles are born around reheating. The above calculation was made simple by assuming that decoupling happens well before reheating, and that there is an extended period during which the dark matter is able to experience this "quasi-decoupled" state between decoupling and reheating. This is not true for many of our dark matter particles, and calculating their momenta following reheating is not as straight forward. Additionally, if kinetic decoupling *does* occur long before reheating, only a small fraction of particles are born early enough to couple to the radiation. In this case, the majority of the particles do not couple to the radiation and so maintain their high velocity and long free-streaming length following reheating. The interesting cases will therefore be when the kinetic decoupling of dark matter occurs around reheating when most of the dark matter is being produced, and

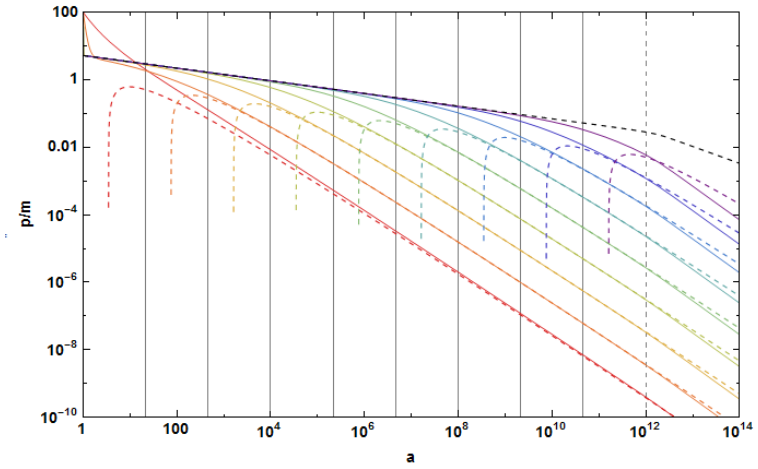

Figure 4.2: The evolution of γv as a function of scale factor for a dark matter particle born at a_i with $\gamma_D = 100$ for $\tilde{\sigma} = 10^{0,1,2,...8}$ (red - purple). Also shown shown is the momentum "floor" $p_{\rm f}$ (black, dotted). Colored dashed lines show the solution to Eq. (4.10) for each of the corresponding $\tilde{\sigma}$'s. Again, $\tilde{\Gamma}_\phi = 10^{-18}$, $n = 2$, $m_\chi = 10$ GeV, and $T_{\rm RH} = 3$ MeV, and vertical line are the same as in Figure 4.1.

determining the momentum of a given particle following reheating will not be as simple as our analytical calculations above when arriving at Eq. (4.10).

However, we can numerically solve Eq. (4.2) under the initial condition $p(a_D) = p_D$ in order to find $p(a, a_D)$. We will again be interested in obtaining a distribution function for the dark matter. If we consider $3a_{\rm RH}$ the point at which further dark matter production is negligible, we can use our previous distribution in the "birth times" of the dark matter, $f(a_D)$, and a numerical solution for $p(a, a_D)$, to find a distribution function for the dark matter momentum following reheating. Once dark matter production is negligible, and once the dark matter is completely decoupled from the radiation, the distribution in the comoving momenta will not change; for the scenarios we wish to consider, the distribution in the comoving momenta will be constant after $10a_{\rm RH}$.

Figure 4.3 shows $p(10a_{\rm RH}, a_D)$ for various values of $\tilde{\sigma}$. The horizontal plateau of each line at lower values of a_D represents the particles born early enough to couple to the radiation and so all have the same momentum at $10a_{\rm RH}$ despite being born at different times. As $\tilde{\sigma}$ increases (red to purple), $a_{\rm kd}$ increases, and so does the maximum value of a_D a particle can have and still fully couple to the radiation. Increasing $\tilde{\sigma}$ also keeps the dark matter coupled to the radiation longer, evolving with $p \propto a^{-3/16}$, delaying the time until it evolves as $a^{-15/16}$ (when $n = 2$), and thus increasing the final value of the momentum the particles will have at $10a_{\rm RH}$.

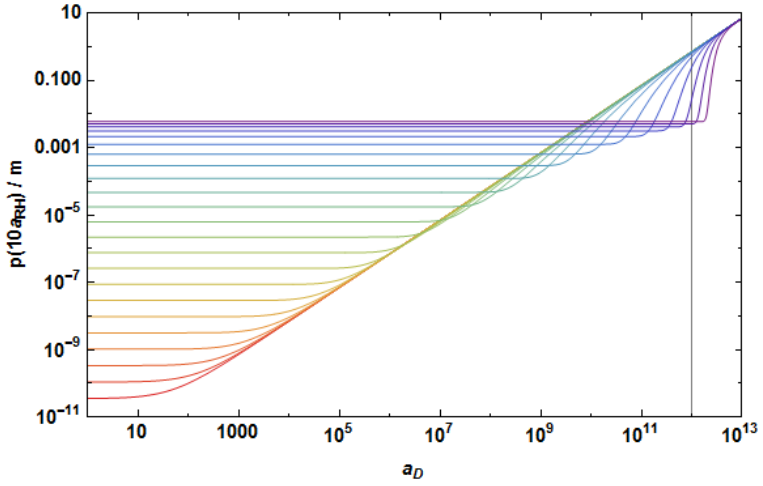

Figure 4.3: The momentum at $10a_{\rm RH}$ of a dark matter particle as a function of it's "birth time" a_D plotted (red to purple) for $\tilde{\sigma} = 10^0, 10^{0.5}, 10^1, 10^{1.5}, ...10^{11}$. Again, $\tilde{\Gamma}_\phi = 10^{-18}$, $n = 2$, $m_\chi = 10$ GeV, and $T_{\rm RH} = 3$ MeV. The vertical line marks $a_D = a_{\rm RH}$.

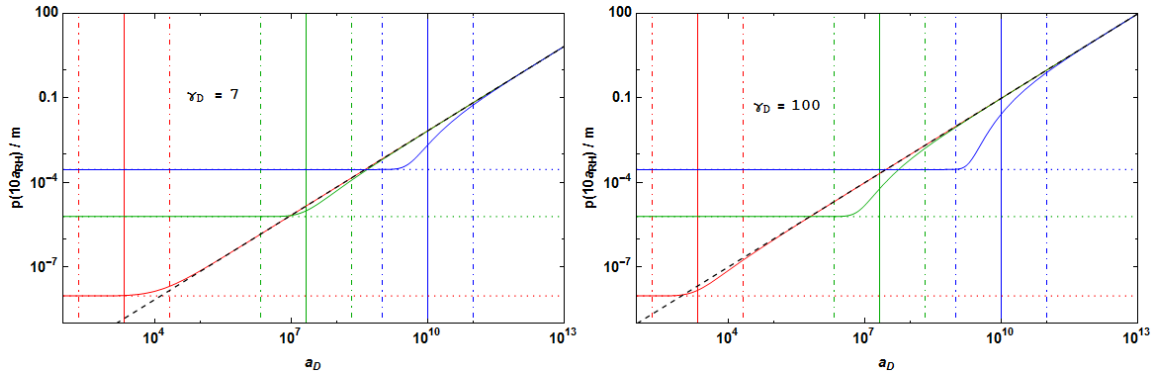

Figure 4.4: Solid lines show $p(10a_{\rm RH}, a_D)$ for $\tilde{\sigma} = 10^{2.5}, 10^{5.5}, 10^{7.5}$ (red, green, blue). Horizontal, dotted lines show the solution to Eq. (4.10) evolved to $10a_{\rm RH}$ for each case. Vertical solid lines mark $a_{\rm kd}$ and vertical dot-dashed lines mark $10a_{\rm kd}$ and $a_{\rm kd}/10$ for each case. The diagonal dashed line shows $p(10a_{\rm RH}, a_D) = (p_D a_D)/(10a_{\rm RH})$, *i.e.* the noninteracting case. The left panel shows scenarios for which $\gamma_D \simeq 7$ ($v_D = 0.99$), the right shows $\gamma_D = 100$. Again, $\tilde{\Gamma}_\phi = 10^{-18}$, $n = 2$, $m_\chi = 10$ GeV, and $T_{\rm RH} = 3$ MeV.

Figure 4.4 highlights in its left panel how the relationship between a_D and $p(10a_{\rm RH})$ is complicated as $a_{\rm kd}$ approaches $a_{\rm RH}$. For $a_{\rm kd} \ll a_{\rm RH}$ ($e.g.$ the red curve in Figure 4.4), our asymptotic behaviors fit well to the full solution of the momentum evolution; particles born early enough to couple to the radiation, have a momentum at $10a_{\rm RH}$ given by Eq. (4.10), the momentum of those born after decoupling is given by the usual a^{-1} scaling, and there is a smooth transition between these regimes. However, as $a_{\rm kd}$ approaches $a_{\rm RH}$, those particles born around $a_{\rm kd}$ deviate from the simple, analytic behaviors. We can begin to understand this deviation by viewing the left panel of Figure 4.5, which shows the momentum evolution for several particles born around $a_{\rm kd}$ for the same three values of $\tilde{\sigma}$ used in Figure 4.4. In the cases where $\tilde{\sigma} = 10^{2.5}$, for particles born before $a_{\rm kd}$, the immediate effect of the dark matter's coupling to the radiation is to decrease the particles' momenta. Following that, however, their momenta redshift increasingly faster than $a^{-3/16}$, but still slower than a^{-1}, before finally settling into the $a^{-15/16}$ scaling. This period of slower-than-a^{-1} redshifting allows them to achieve an higher momentum at $10a_{\rm RH}$ than they otherwise would in the absence of interactions. This is reflected in Figure 4.4 by all particles in the $\tilde{\sigma} = 10^{2.5}$ with $a_D < a_{\rm kd}$ lying on the horizontal plateau and above the black, dashed line representing the noninteracting case. Particles born at $10a_{\rm kd}$ in the $\tilde{\sigma} = 10^{2.5}$ case, do not quite fully couple to the radiation but still experience the $a^{-15/16}$ scaling in their momentum and reach a higher final momentum at $10a_{\rm RH}$ than they would have without interactions. This is shown in in the left panel of Figure 4.4 by particle born at $10a_{\rm kd}$ having a momentum above the dotted red line, and still above the black, dashed line. Particles born sufficiently after $a_{\rm kd}$ never experience enough collisions with the radiation for their momentum to deviate from $p \propto a^{-1}$ and so all lie on the black, dashed line of Figure 4.4. In the cases where $\tilde{\sigma} = 10^{2.5}$, the few particles born early enough to feel the effect of their coupling to the radiation are all slightly warmed due to the interactions.

Contrarily, for the cases in which $\tilde{\sigma} = 10^{7.5}$, some particles end up colder than they other wise would have without interactions. For particles born around $a_{\rm kd}$, the initial decrease in the particles' momenta is the dominant effect. There is not enough time before reheating for the slower-than-a^{-1} redshifting in their momenta to overcome this initial decrease and they are colder at $10a_{\rm RH}$ than in the noninteracting case. This is reflected in Figure 4.4 by the region in which the blue curve falls below the black, dashed line. Because we will be interested in cases where $a_{\rm kd} \sim a_{\rm RH}$, we will be dealing with $p(10a_{\rm RH}, a_D)$ relations of the type illustrated by the blue curve of Figure 4.4: early-born particles which couple to the radiation will be warmer compared to the noninteracting case, while later-born particles that are able to couple to the radiation can end up colder (below the black, dashed line).

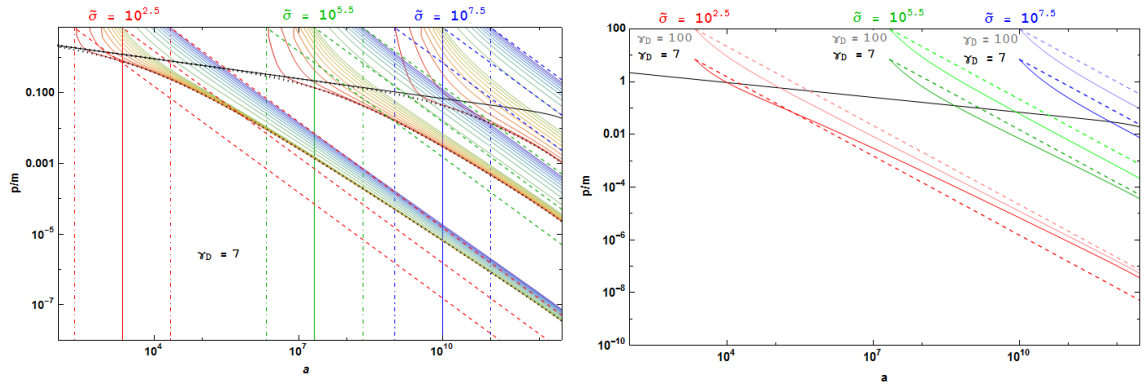

Figure 4.5: Left: The three sets of red to purple lines show, for the three cases $\tilde{\sigma} = 10^{2.5}, 10^{5.5}$, and $10^{7.5}$, the evolution of γv as a function of scale factor for dark matter particles born between $a_{\rm kd}/10 < a_D < 10a_{\rm kd}$ with $v_D = 0.99$. In dotted black is the evolution of γv for a dark matter particles born a_i. In solid black is the momentum of the "floor" $p_{\rm f}$. Vertical solid lines mark $a_{\rm kd}$ and vertical dot-dashed lines mark $10a_{\rm kd}$ and $a_{\rm kd}/10$ for each case $\tilde{\sigma} = 10^{2.5}, 10^{5.5}$, and $10^{7.5}$ (red, green, blue), as in Figure 4.4. Colored dashed lines show the evolution of γv in the noninteracting case for $a_D = a_{\rm kd}/10, a_{\rm kd}$, and $10a_{\rm kd}$. Right: For the three cases $\tilde{\sigma} = 10^{2.5}, 10^{5.5}$, and $10^{7.5}$ (red, green, blue) the evolution of γv as a function of scale factor for dark matter particles born at $a_{\rm kd}$ with $\gamma_D = 7$ (solid) and $\gamma_D = 100$ (dashed). Again, $\tilde{\Gamma}_\phi = 10^{-18}$, $n = 2$, $m_\chi = 10$ GeV, and $T_{\rm RH} = 3$ MeV.

The right panels of Figures 4.4 and 4.5 illustrate how the relativistic nature of dark matter can further complicate the relationship between a_D and $p(10a_{\rm RH})$. Highly relativistic dark matter particles require an even longer period between decoupling and reheating for the "quasi-decoupling" behavior to become the dominant effect in determining the particles' momenta following reheating. While illuminating, our above analytical calculations break down in the regimes of most interest to our investigations: dark matter produced highly relativistic from decay that kinetically decouples from SM radiation near reheating. With a numerical solution of $p(a, a_D)$, however, we can obtain the distribution function in dark matter momentum following reheating from the distribution of birth times of the dark matter particles for those interesting scenarios when $a_{\rm kd} \sim a_{\rm RH}$.

All of our examples in the figures above present our calculations for a single set of values for the dark matter mass, $m_\chi = 10$ GeV, and the temperature at reheating, $T_{\rm RH} = 3$ MeV. Changing either of these quantities changes the momentum to which the dark matter equilibrates and the velocity it possesses at reheating. As mentioned earlier, increasing the temperature at reheating will increase the velocity of particles which experienced coupling with the radiation, while increasing the dark matter mass will decrease the velocity. We will continue with our fiducial example throughout our analysis and remark on how changing the ratio between the dark matter mass and reheat temperature will affect our results.

4.2 Dark Matter Distribution Function

As we previously mentioned, once dark matter production is negligible, and once the dark matter is completely decoupled from the radiation, the distribution in the comoving momenta will not change. We know from the previous chapter that dark matter production becomes negligible after $3a_{\rm RH}$; the point at which dark matter is completely decoupled from the radiation depends on the value of $\tilde{\sigma}$. For any of the following scenarios we will consider, the dark matter will fully decouple from SM radiation before $10a_{\rm RH}$ and we will consider the distribution in the comoving dark matter momentum fixed beyond that point. While we could easily establish the distribution in dark matter momentum following reheating as:

$$f(p(10a_{\rm RH})) = f(a_D)\frac{da_D}{dp(10a_{\rm RH})}, \tag{4.11}$$

the numerical relation we would find between $p(10a_{\rm RH})$ and a_D by solving Eq. (4.2) is not exactly valid for those particles that coupled to the radiation. The horizontal plateau in Figure 4.3 suggests all particles born early enough to couple to the radiation will have the *exact* same momentum following reheating, $p_{\rm min} \equiv p(a_i, 10a_{\rm RH})$. More realistically however, the dark matter is reaching kinetic equilibrium with a radiation bath whose particles, though characterized by a single temperature, have a distribution of momenta, and so the momenta of coupled particles will also have a distribution (whose average value is $p_{\rm min}$). We assume for these particles that have thermalized a Maxwell-Boltzmann distribution:

$$f(p(10a_{\rm RH})) \propto \exp\left[-\frac{p^2(10a_{\rm RH})}{2m_\chi T}\right] = \exp\left[-\frac{3\,p^2(10a_{\rm RH})}{2\,p_{\rm min}^2}\right]. \tag{4.12}$$

This distribution function will be normalized to the fraction of dark matter particles born early enough for their momentum to be appreciably affected by interactions. We will consider this to be those particles whose momenta are brought down within $p < 2p_{\rm min}$. For those particles with momentum after reheating $p \gg p_{\rm min}$, their momenta are given by the numerical relation between $p(10a_{\rm RH})$ and a_D found by solving Eq. (4.2). There is still, however, a relatively large number of particles with momenta $p \gtrsim 2p_{\rm min}$, which creates a sharp upturn in the distribution function near this value of the momentum when using the numerical relation between $p(10a_{\rm RH})$ and a_D at these lower momenta values. In order to smooth our distribution function, we artificially redistribute these particles into a thermal tail matched onto the distribution function for particles for which $p(10a_{\rm RH}) \gg p_{\rm min}$. Adding this smoothed distribution function for unthermalized particles to our

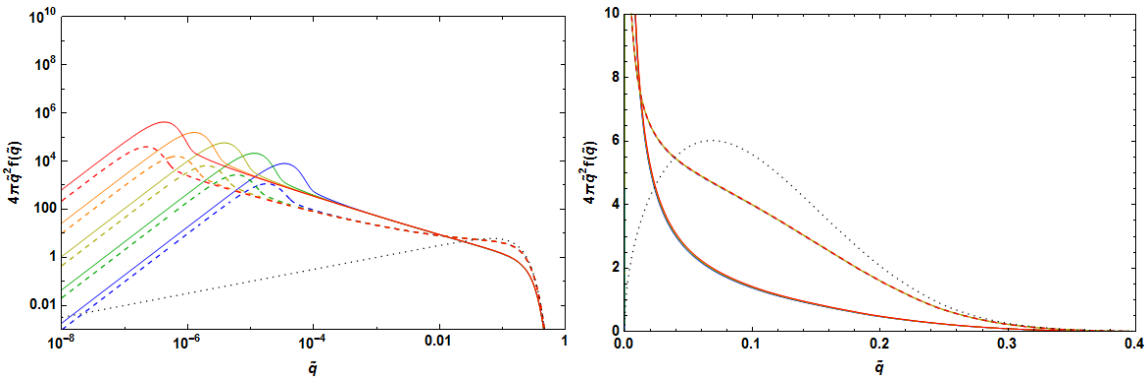

Figure 4.6: $f(\tilde{q})$ for the noninteracting case (black, dotted) and the interacting cases with $\tilde{\sigma} = 10^{10}$ (solid) and $\tilde{\sigma} = 10^{9}$ (dashed) with $\gamma_D = 100, 300, 900, 2700, 8100$ (blue to red). Here, $n = 2$ and $m_\chi/T_{\rm RH} \simeq 3300$.

Maxwell Boltzmann distribution for thermalized particle, we obtain the full momentum distribution function for a scenario of interacting nonthermal dark matter.

As in the previous chapter, we will scale the comoving momenta of the dark matter particles by the comoving momentum of a particular particle. In this case, we will consider a particle that has momentum p_D at $10a_{\rm RH}$, so that when we examine the distribution function at $10a_{\rm RH}$, we have

$$\tilde{q} = \frac{ap}{10a_{\rm RH}p_D} = \frac{10a_{\rm RH}p(10a_{\rm RH})}{10a_{\rm RH}p_D} = \frac{p(10a_{\rm RH})}{p_D}. \tag{4.13}$$

Using this we have the distribution function:

$$f(\tilde{q}) = f(p(10a_{\rm RH}))\frac{dp(10a_{\rm RH})}{dq}. \tag{4.14}$$

In Figure 4.6 we show how the distribution functions $f(\tilde{q})$ compare for the interacting (with $\tilde{\sigma} = 10^9$ and 10^{10}) and noninteracting cases. The value of $p_{\rm min}$ decreases with decreasing $\tilde{\sigma}$, and so our distribution functions for the $\tilde{\sigma} = 10^9$ cases peak at lower values of $\tilde{q}$ than in the $\tilde{\sigma} = 10^{10}$ cases with the same velocity at production. Increasing the velocity at production increases p_D and also lowers the value of $\tilde{q}$ at which the distribution function peaks. In both presented cases, interactions between the dark matter and SM radiation lead to a significantly colder momentum distribution. Once again we point out that these distribution functions represent a single value for the ratio of $T_{\rm RH}/m_\chi = 0.0003$. Increasing this ratio will increase the dark matter velocity following reheating, increasing the value of $\tilde{q}$ at which the distribution function peaks.

4.3 Free-Streaming Lengths

Once more we calculate the physical free-streaming length today of a particle born at reheating:

$$\lambda_{\mathrm{fs},0}^{\mathrm{phys}} = a_0 \int_{a_{\mathrm{RH}}}^{a_0} v(a) \frac{da}{a^2 H(a)}. \tag{4.15}$$

The free-streaming length in our interacting cases can be computed analytically just as we did in Chapter 3 by focusing on the distance covered by a streaming particle after changes in the relativistic degrees of freedom have ceased. This allows us to assume $H \propto a^{-2}$ during radiation domination, and we break up the free-streaming integral in to two parts, representing the radiation- and matter-dominated eras, that can be solved analytically.

Previously, in Chapter 3, the variable Y was defined to be $Y \equiv (\gamma_D v_D a_D)^2$, which is the comoving momentum of a particle, scaled by its mass, and is constant following the dark matter's production in the noninteracting case; the velocity evolution of the particle is then given by the relationship $\gamma v = \sqrt{Y}/a$. In our interacting cases, the comoving momentum of a dark matter particle is not constant until after the dark matter has kinetically decoupled and so we replace the variable Y with a new variable $Z \equiv [p(10a_{\mathrm{RH}})10a_{\mathrm{RH}}/m]^2$ such that the velocity evolution of a particle after $10a_{\mathrm{RH}}$ in the interacting case is given by the relationship $\gamma v = \sqrt{Z}/a$. The value of $p(10a_{\mathrm{RH}})$ will change according to the particle under consideration; in our previous analysis we chose to consider the median particle ($a_D = a_{\mathrm{RH}}$), but we will remain ambiguous about the value of $p(10a_{\mathrm{RH}})$ for now. The free-streaming length in the noninteracting scenario is then:

$$\begin{aligned}
\lambda_{\mathrm{fs}} = \int_{a_*}^{a_0} \sqrt{\frac{Z}{Z+a^2}} \frac{da}{a^2 H(a)} &\simeq \frac{1}{H_* a_*^2} \int_{a_*}^{a_{\mathrm{eq}}} \sqrt{\frac{Z}{Z+a^2}}\ da + \frac{1}{H_{\mathrm{eq}} a_{\mathrm{eq}}^{3/2}} \int_{a_{\mathrm{eq}}}^{a_0} \sqrt{\frac{Z}{Z+a^2}} \frac{da}{\sqrt{a}} \\
&= \frac{\sqrt{Z}}{H_* a_*^2} \ln\left(\frac{a_{\mathrm{eq}} + \sqrt{Z + a_{\mathrm{eq}}^2}}{a_* + \sqrt{Z + a_*^2}} \right) + \frac{2\sqrt{i\sqrt{Z}}}{H_{\mathrm{eq}} a_{\mathrm{eq}}^{3/2}} F\left(i \sinh^{-1} \sqrt{\frac{i\sqrt{Z}}{a}}, -1 \right) \Bigg|_{a_{\mathrm{eq}}}^{a_0},
\end{aligned} \tag{4.16}$$

where we remind the reader that, just as in Eq. (3.26), a_* is the value of the scale factor after which g_* remains constant, and $F(\phi, m)$ is the elliptic integral of the first kind. The first term in the above expression can be simplified under the assumption that $a_{\mathrm{eq}} \gg 10a_{\mathrm{RH}}$, which is reasonable considering that matter-radiation equality occurs at a temperature of $T_{\mathrm{eq}} \simeq 0.8$ eV and we still require $T_{\mathrm{RH}} > 3$ MeV. The dark matter velocity

and the reheat temperature enter into this expression through the combination

$$\nu \equiv \frac{p(10a_{\rm RH})}{m}\frac{10a_{\rm RH}}{a_0} = \frac{p(10a_{\rm RH})}{m}\frac{10\,T_0 g_{*S,0}^{1/3}}{3\left[T g_{*S}^{1/3}\right]_{T=0.34T_{\rm RH}}}, \tag{4.17}$$

where, again, we assume entropy is conserved after $a = 3a_{\rm RH}$. Particles that fully coupled to the radiation will have a velocity following reheating that is entirely determined by the momentum floor to which they coupled and related to the quantity $p_{\rm f,RH}/m_\chi \propto \sqrt{T_{\rm RH}/m_\chi}$ as discussed earlier. The velocity of particles that never coupled to the radiation is related to their velocity at production just as in the previous chapter. For particles that experience scattering interactions but do not fully couple to the radiation, the value of the particles' velocities following reheating will depend on the dark matter velocity at production and the ratio $m_\chi/T_{\rm RH}$, which determines how affected the particles are by interactions. When decoupling occurs near reheating, many particles fall into this last intermediate regime.

Expressed in terms of the new variable ν, the physical free-streaming length calculated from the contribution from both the radiation- and matter-dominated eras is

$$\begin{aligned}\lambda_{\rm fs,0}^{\rm phys} = &\left(4.66\times10^5{\rm Mpc}\right)\nu\left[\ln\left(2\frac{T_*}{T_{\rm eq}}\right) - \ln\left(1+\sqrt{\nu^2\left(\frac{T_*}{T_0}\right)^2+1}\right)\right] \\ &+ \left(4.66\times10^5{\rm Mpc}\right)\sqrt{\frac{T_0}{T_{\rm eq}}}\sqrt{2i\nu}\left[F\left(i\sinh^{-1}\sqrt{i\nu}\right) - F\left(i\sinh^{-1}\sqrt{i\nu\frac{T_{\rm eq}}{T_0}}\right)\right],\end{aligned} \tag{4.18}$$

which is exactly the form of Eq. (3.29) but with $\mu \to \nu$. In the previous chapter, we calculated the free-streaming length of the median dark matter particle ($a_D = a_{\rm RH}$) to represent the scales at which we expected to see suppressed structure growth. We will see that, in our interacting case, the median value of the dark matter momentum following reheating may not be as good a representation for determining the scale at which we expect to begin seeing deviations from ΛCDM in the matter power spectrum. In the next section we compute the transfer function for a more precise determination of the effects of the dark matter free-streaming length.

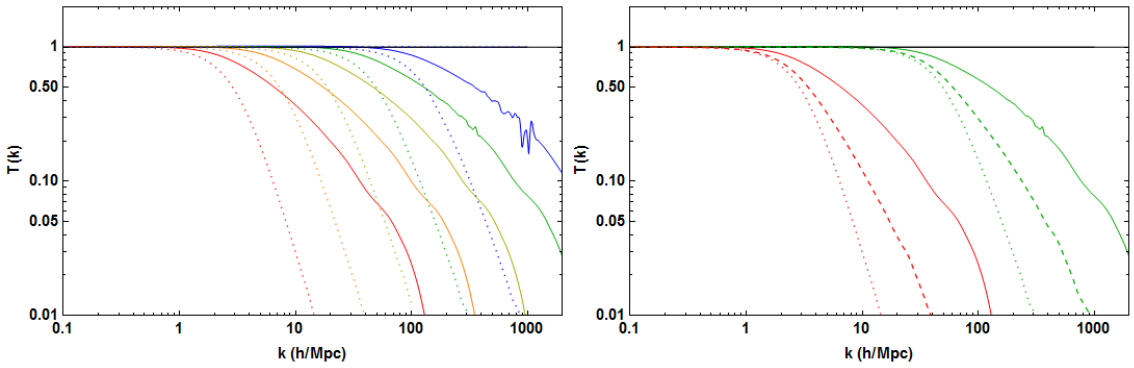

Figure 4.7: The transfer function for $T_{\rm RH} = 3$ MeV and several values of the dark matter velocity at production, v_D. Left: Colored lines represent (cool to warm) dark matter produced with increasing Lorentz factor $\gamma_D = 100, 300, 900, 2700, 8100$, respectively. Solid lines show the transfer functions in the interacting case with $\tilde{\sigma} = 10^{10}$ while dotted lines show the transfer functions in the noninteracting case (same as in Figure 3.9). Right: Transfer function for dark matter produced with γ_D =100 and 2700 (green and red) for $\tilde{\sigma} = 10^{10}$ (solid), $\tilde{\sigma} = 10^{9}$ (dashed), and the noninteracting case (dotted). Again, $n = 2$ and $m_\chi/T_{\rm RH} \simeq 3300$.

4.4 Transfer Functions

We use the Cosmic Linear Anisotropy Solving System (CLASS) [115] to obtain the dark matter transfer function,

$$T^2(k) \equiv \frac{P_{\rm nCDM}(k)}{P_{\rm CDM}(k)}, \tag{4.19}$$

which describes suppression of structure due to non-cold dark matter (nCDM) compared to that of the standard CDM scenario. With our distribution function $f(\tilde{q})$, we are able to use CLASS to obtain transfer functions for any combination of the velocity imparted to the dark matter and the reheat temperature by also providing the present-day physical momentum of a dark matter particle with $\tilde{q} = 1$:

$$p_0 = p(10a_{\rm RH})\frac{10a_{\rm RH}}{a_0}. \tag{4.20}$$

The value of $p(10a_{\rm RH})$ encodes the effect of both the velocity imparted to the dark matter and the reduction of that velocity due to scattering interactions. In Figure 4.7 we show the transfer functions for dark matter produced at different velocities, but in scenarios with the same mass, 10 GeV, and reheat temperature, 3 MeV.

As we expected, scattering interactions cool the dark matter and lead to less suppression of structure growth compared to the noninteracting scenario. As well, we can confirm from Figure 4.7 that a larger

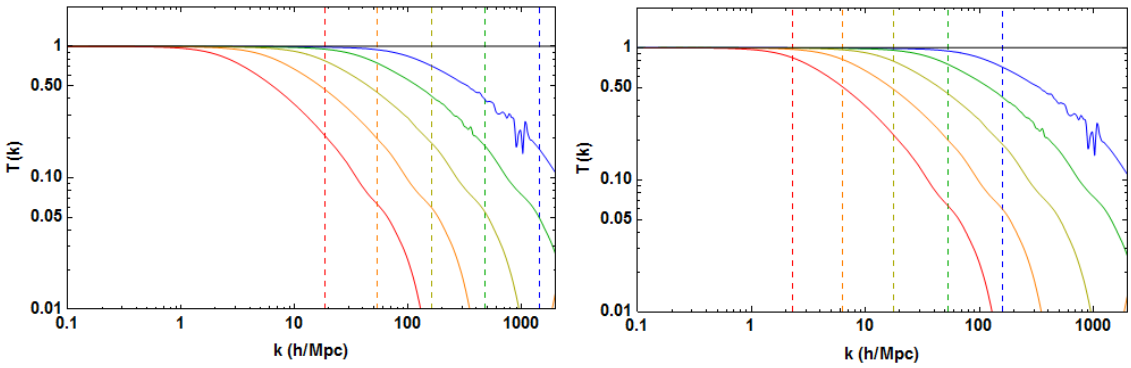

Figure 4.8: The transfer function for $T_{\rm RH} = 3$ MeV and several values of the dark matter velocity at production, v_D. The color of the lines represent (cool to warm) dark matter produced with increasing Lorentz factor $\gamma_D = 100, 300, 900, 2700, 8100$, respectively. Left: Vertical dashed lines represent the scale of the free-streaming horizon calculated using Eq. (4.18) and the *median* momentum following reheating. Right: Vertical dashed lines represent the scale of the free-streaming horizon calculated using Eq. (4.18) and the *mean* momentum following reheating. Again, $n = 2$ and $m_\chi/T_{\rm RH} \simeq 3300$.

value of the momentum transfer rate leads to less suppression between interacting cases. Also notable in the transfer functions of the interacting cases is a small feature - a slight dip at approximately $T(k) = 0.1$. (The small, sharp deviations seen in the blue and green curves throughout Figures 4.7 through 4.9 are an unphysical consequence of numerical interpolation.) Though an interesting consequence of the new shape of our momentum distribution function, $T(k) \lesssim 0.1$ already represents a great suppression of power in the nCDM model, making distinguishing such an effect extremely unlikely. We also point out that, compared to the noninteracting case, the scale at which the transfer functions in the interacting case begin to deviate from CDM is pushed higher values of k and the rate at which it falls off after that point, is much slower.

In Figure 4.8 we show effect of considering the mean or median particle as the representative particle of the dark matter free-streaming length. The left panel shows, as vertical dashed lines, the free-streaming scale $k_{\rm fs} = (\lambda_{\rm fs,0}^{\rm phys})^{-1}$ given by Eq. (4.18) of a particle with the median momentum following reheating. The right panel shows the free-streaming scale as determined by the mean dark matter momentum. Clearly, in this case the mean particle momentum is a better predictor of scale at which the nCDM power spectrum begin to deviate from ΛCDM. Unlike in our previous analysis, the mean and median of the interacting dark matter's momentum distribution function can be significantly different. The median momentum in the interacting cases falls below that of the mean dark matter particle, and so the median appears to underestimate how much suppression is caused by the particles that reside in the hot tail of the momentum distribution function.

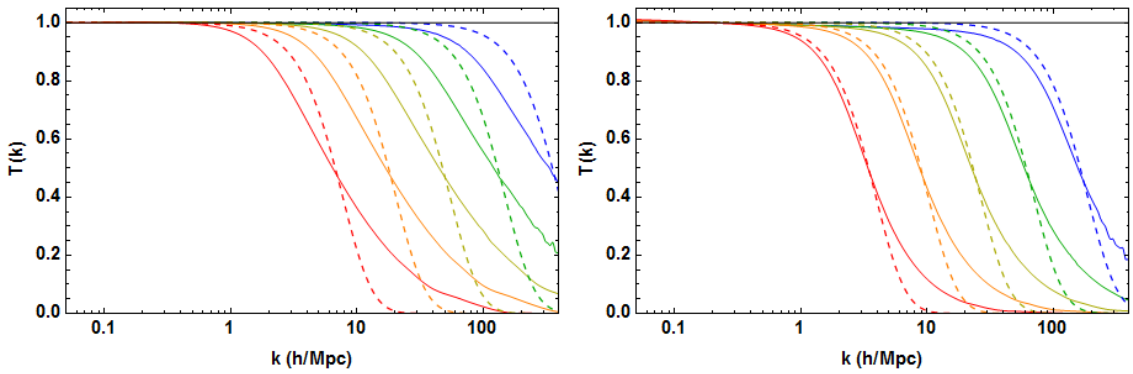

Figure 4.9: The transfer functions (solid) for $T_{\rm RH} = 3$ MeV and several values of the dark matter velocity at production, v_D. The color of the lines represent (cool to warm) dark matter produced with increasing Lorentz factor $\gamma_D = 100, 300, 900, 2700, 8100$, respectively. In the left panel $\tilde{\sigma} = 10^{10}$ and in the right $\tilde{\sigma} = 10^{9}$. Dashed lines show the thermal WDM transfer functions with matched half-mode scales. Again, $n = 2$ and $m_\chi/T_{\rm RH} \simeq 3300$.

In Figure 4.9 we can see more even clearly the effect that the interactions have on the shape of the dark matter transfer functions. Previously, the transfer functions of our noninteracting nonthermal dark matter scenario and those of thermal WDM transfer functions with the same half-mode scale only began to differ significantly in shape at scales at which the power in the nCDM model was already greatly suppressed ($T(k) \lesssim 0.1$). Figure 4.9 shows that the transfer functions of thermal WDM can be vastly different in shape from the interacting nonthermal transfer functions. Comparing the left and right panels, which show the transfer functions in the $\tilde{\sigma} = 10^{10}$ and $\tilde{\sigma} = 10^{9}$, respectively, we can see that the difference in transfer function shape is exacerbated for increasing values of $\tilde{\sigma}$. Given this noticeable discrepancy it would be unwise to apply constraints on the half-mode scale obtained by simulations of WDM. Using thermal WDM transfer functions with the same half-mode scale to represent our scenario would underestimate suppression on scales above the half-mode; in the $\tilde{\sigma} = 10^{10}$ case this underestimation could be severe. In addition, the transfer function of the interacting case differs significantly from the noninteracting case. Therefore, obtaining robust bounds on these interacting cases would require another full analysis in which we fit the form of the transfer function by Eq. (3.34) and constrain the parameter space of α, β, and γ.

4.5 Discussion

We can still estimate how interactions will change the bounds on nonthermal dark matter production by considering when the dark matter free streaming scale, $k_{\rm fs} = (\lambda_{\rm fs,0}^{\rm phys})^{-1}$, is naively probable by Lyman$-\alpha$

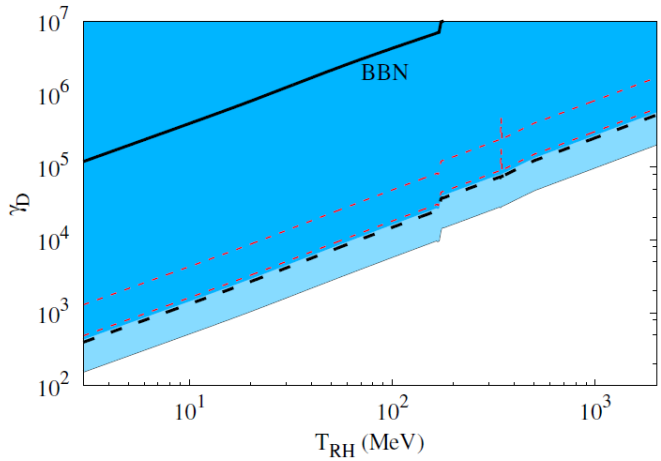

Figure 4.10: Limits on the Lorentz factor γ_D and the reheat temperature. The shaded regions correspond to the 1σ and 2σ bounds, $\alpha = 0.011\text{Mpc}/h$ and $0.026\text{Mpc}/h$, respectively for the noninteracting scenario. The black dashed line represents $k_{\text{fs}} = (\lambda_{\text{fs}})^{-1} = 12.6h/\text{Mpc}$ as calculated by Eq. (3.29). The red dashed lines represents $k_{\text{fs}} = (\lambda_{\text{fs}})^{-1} = 12.6h/\text{Mpc}$ in the interacting as calculated by Eq. (4.18) using the mean dark matter momentum following reheating, for $\tilde{\sigma} = 10^{10}$ (top) and $\tilde{\sigma} = 10^{9}$ (bottom), and $m_\chi/T_{\text{RH}} \simeq 3300$. The discontinuity at $T_{\text{RH}} \simeq 170\text{MeV}$ occurs due to the sudden change in g_* during the QCD phase transition. The thick solid line shows the bound on γ_D as a function of T_{RH} imposed by BBN, derived in Section 3.1.1.

data. As we saw in Chapter 3, constraining the free-streaming scale to lie above $k \gtrsim 12.6\ h/\text{Mpc}$ gave a good estimate of the bounds one could expect to be able to put on the parameter space of γ_D and T_{RH}. In Chapter 3, the scale at which the nonthermal dark matter power spectrum began to deviate from that of CDM was represented by the free-streaming scale of the dark matter particle with the median momentum following reheating. The scale at which this occurs in the case of interacting nonthermal dark matter is better represented by the free-streaming scale of the particle with the mean momentum following reheating. Using Eq. (4.18) and the mean dark matter momentum once the particles have fully kinetically decoupled to calculate k_{fs} in the interacting case, we can present tentative bounds on γ_D and T_{RH} for a given value of the momentum transfer rate. Since our interacting transfer functions lie below those of the noninteracting case at scales below the half-mode scale, it is likely that these bounds are more lenient.

Our final figure, Figure 4.10, shows these bounds for the interacting case along side those derived in the noninteracting case in Section 3.3.2. For the scenario in which $\tilde{\sigma} = 10^9$, the transfer functions only differed slightly from those of the noninteracting case (especially for $T(k) > 0.5$), and our bounds on the parameter space of γ_D and T_{RH} are, expectedly, not that different between the two cases. For the scenario in which $\tilde{\sigma} = 10^{10}$, however, the scattering interactions appreciably cooled the dark matter and could tentatively relax the restrictions on γ_D and T_{RH}.

Once more we remark on the fact that these results represent a fiducial example with a fixed ratio $T_{\rm RH}/m_\chi \simeq 0.0003$. Since we show our constraints as a function of the reheat temperature, along our boundary lines in Figure 4.10 for the interacting cases, the dark matter mass is increasing with reheat temperature in order to keep this ratio fixed. As we know, increasing the ratio $T_{\rm RH}/m_\chi$ will increase the dark matter velocity at decoupling and therefore its velocity following reheating. Thus we expect increasing this ratio will tighten our bounds, drawing them closer to those of the noninteracting case; similarly, decreasing this ratio could further relax our constraints. Just as interactions have little effect on our bounds for dark matter that decouples too early ($a_{\rm kd} \lesssim 0.73 a_{\rm RH}$), we expect changing this ratio to have little effect on the bounds in these cases. However, the effect could be significant for dark matter that decouples a bit later ($a_{\rm kd} \sim 2.5 a_{\rm RH}$).

Thus, we can see that scattering interactions between dark matter and SM radiation particles could, indeed, substantially cool dark matter particles produced nonthermally with large momenta. However, in order to cool enough of the particles to have a discernable effect on the matter power spectrum, the kinetic decoupling of the dark matter particles must occur near reheating, when most of the particles are being produced. For reference, $a_{\rm kd} \simeq 0.73 a_{\rm RH}$ ($\simeq 2.5 a_{\rm RH}$) for the case in which $\tilde{\sigma} = 10^9$ ($= 10^9$). Though certainly as specialized scenario, it does show that allowing a method by which the dark matter can rapidly lose momenta opens the parameter space for the allowed velocity at its production. Unfortunately, it does not appear that this effect is significant enough to allow for the preservation of micro halos that formed from perturbation that grow during the EMDE.

CHAPTER 5
Conclusion

Less than 5% of the current energy content of the Universe is contained in "ordinary" matter, $i.e.$ in Standard Model (SM) particles; the remaining 95% exists in the forms of what we call dark matter and dark energy. Observable only through its gravitational interactions, what we know most conclusively about dark matter is that it is not composed of SM particles. All we know about dark energy is that its energy density is not detectably diluted by the expansion of the Universe. Adequate explanations of the nature and origin of both dark matter and dark energy require the introduction of new, beyond-SM physics. A promising regime to search for new physics is in high-energy, extreme environments like that of the early Universe. We investigated how a particular theory of dark energy behaves in the early Universe and how the production method of dark matter in the early Universe could effect the formation of structure we see today.

In chameleon gravity, a theory of modified gravity aimed to explain dark energy, there exists a light scalar field that couples to the trace of the stress-energy tensor in such a way that its mass depends on the ambient matter density, and the field is screened in local, high-density environments. Recently it was shown that, for the runaway potentials commonly considered in chameleon theories, the field's coupling to matter and the hierarchy of scales between Standard Model particles and the energy scale of such potentials result in catastrophic effects in the early Universe when these particles become nonrelativistic. Perturbations with trans-Planckian energies are excited, and the theory suffers a breakdown in calculability at the relatively low temperatures of BBN. We considered a chameleon field in a quartic potential and showed that the scale-free nature of this potential allows the chameleon to avoid many of the problems encountered by runaway potentials. We began with a classical treatment of the chameleon field following inflation, showing that the quartic chameleon oscillates around the minimum of its effective potential, contrary to runaway potential models in which the field became stuck far from its minimum due to Hubble friction. A quantum treatment of the quartic chameleon's dynamics showed that its oscillations caused rapid changes in its effective mass and perturbations were excited via quantum particle production. While quantum correction to the field's evolution

must be taken into account, high-energy perturbations are only generated at comparably high temperatures and the quartic chameleon is able remain a well-behaved effective field theory at nucleosynthesis.

The inclusion of a period of (effective) matter domination following inflation and prior to the onset of radiation domination has interesting and observable consequences for structure growth. During this early matter-dominated era (EMDE), the Universe was dominated by massive particles, or an oscillating scalar field, that decayed into Standard Model particles, thus reheating the Universe. This decay process could also have been the primary source of dark matter. In the absence of fine-tuning between the masses of the parent and daughter particles, both dark matter particles and Standard Model particles would be produced with relativistic velocities. We investigated the effects of the nonthermal production of dark matter particles with relativistic velocities on the matter power spectrum by determining the resulting velocity distribution function for the dark matter. We found that the vast majority of dark matter particles produced during the EMDE are still relativistic at reheating, so their free streaming erases the perturbations that grow during the EMDE. The free streaming of the dark matter particles can also prevent the formation of satellite galaxies around the Milky Way and the structures observed in the Lyman-α forest. For a given reheat temperature, these observations put an upper limit on the velocity of the dark matter particles at their creation.

We then considered whether these constraints could be relaxed by including scattering interactions between the dark matter and SM particles. Following our analyses in the case of noninteracting dark matter, we obtained the dark matter momentum distribution function resulting from the inclusion of scattering interactions with SM radiation. We compare this scenario to both our previous nonthermal dark matter production results, as well as to the CDM scenario by contrasting the effects the scattering interactions have on the resulting matter power spectrum. We found that our constraints on nonthermal dark matter production could, in fact, be relaxed by as much as an order of magnitude in the Lorentz factor of the dark matter particles at their production, but only when the kinetic decoupling of dark matter occurs at or around reheating.

BIBLIOGRAPHY

[1] N. Aghanim et al. Planck 2018 results. VI. Cosmological parameters. 2018.

[2] S. Perlmutter et al. Measurements of Ω and Λ from 42 high redshift supernovae. *Astrophys. J.*, 517: 565–586, 1999. doi: 10.1086/307221.

[3] Adam G. Riess et al. Observational evidence from supernovae for an accelerating universe and a cosmological constant. *Astron. J.*, 116:1009–1038, 1998. doi: 10.1086/300499.

[4] Graeme E. Addison, Gary Hinshaw, and Mark Halpern. Cosmological constraints from baryon acoustic oscillations and clustering of large-scale structure. *Mon. Not. Roy. Astron. Soc.*, 436:1674–1683, 2013. doi: 10.1093/mnras/stt1687.

[5] F. Zwicky. Die Rotverschiebung von extragalaktischen Nebeln. *Helvetica Physica Acta*, 6:110–127, January 1933.

[6] Vera C. Rubin and Jr. Ford, W. Kent. Rotation of the Andromeda Nebula from a Spectroscopic Survey of Emission Regions. *Astrophys. J. Suppl.*, 159:379, February 1970. doi: 10.1086/150317.

[7] Kevork N. Abazajian et al. The Seventh Data Release of the Sloan Digital Sky Survey. *Astrophys. J. Suppl.*, 182:543–558, 2009. doi: 10.1088/0067-0049/182/2/543.

[8] P. A. R. Ade et al. Planck 2015 results. XIII. Cosmological parameters. *Astron. Astrophys.*, 594:A13, 2016. doi: 10.1051/0004-6361/201525830.

[9] Eiichiro Komatsu et al. Results from the Wilkinson Microwave Anisotropy Probe. *PTEP*, 2014: 06B102, 2014. doi: 10.1093/ptep/ptu083.

[10] Shin'ichi Nojiri and Sergei D. Odintsov. Unified cosmic history in modified gravity: from F(R) theory to Lorentz non-invariant models. *Phys. Rept.*, 505:59–144, 2011. doi: 10.1016/j.physrep.2011.04.001.

[11] Thomas P. Sotiriou and Valerio Faraoni. f(R) Theories Of Gravity. *Rev. Mod. Phys.*, 82:451–497, 2010. doi: 10.1103/RevModPhys.82.451.

[12] Antonio De Felice and Shinji Tsujikawa. f(R) theories. *Living Rev. Rel.*, 13:3, 2010. doi: 10.12942/lrr-2010-3.

[13] Israel Quiros. Selected topics in scalar–tensor theories and beyond. *Int. J. Mod. Phys.*, D28(07): 1930012, 2019. doi: 10.1142/S021827181930012X.

[14] Jerome Martin. Quintessence: a mini-review. *Mod. Phys. Lett.*, A23:1252–1265, 2008. doi: 10.1142/S0217732308027631.

[15] David Kirkman, David Tytler, Nao Suzuki, John M. O'Meara, and Dan Lubin. The Cosmological baryon density from the deuterium to hydrogen ratio towards QSO absorption systems: D/H towards Q1243+3047. *Astrophys. J. Suppl.*, 149:1, 2003. doi: 10.1086/378152.

[16] Richard H. Cyburt. Primordial nucleosynthesis for the new cosmology: Determining uncertainties and examining concordance. *Phys. Rev.*, D70:023505, 2004. doi: 10.1103/PhysRevD.70.023505.

[17] Shadab Alam et al. The clustering of galaxies in the completed SDSS-III Baryon Oscillation Spectroscopic Survey: cosmological analysis of the DR12 galaxy sample. *Mon. Not. Roy. Astron. Soc.*, 470 (3):2617–2652, 2017. doi: 10.1093/mnras/stx721.

[18] Clifford M. Will. The Confrontation between General Relativity and Experiment. *Living Rev. Rel.*, 17: 4, 2014. doi: 10.12942/lrr-2014-4.

[19] Mustapha Ishak. Testing General Relativity in Cosmology. *Living Rev. Rel.*, 22(1):1, 2019. doi: 10.1007/s41114-018-0017-4.

[20] Paulo C. C. Freire, Norbert Wex, Gilles Esposito-Farese, Joris P. W. Verbiest, Matthew Bailes, Bryan A. Jacoby, Michael Kramer, Ingrid H. Stairs, John Antoniadis, and Gemma H. Janssen. The relativistic pulsar-white dwarf binary PSR J1738+0333 II. The most stringent test of scalar-tensor gravity. *Mon. Not. Roy. Astron. Soc.*, 423:3328, 2012. doi: 10.1111/j.1365-2966.2012.21253.x.

[21] Alain Riazuelo and Jean-Philippe Uzan. Cosmological observations in scalar - tensor quintessence. *Phys. Rev.*, D66:023525, 2002. doi: 10.1103/PhysRevD.66.023525.

[22] Alain Coc, Keith A. Olive, Jean-Philippe Uzan, and Elisabeth Vangioni. Big bang nucleosynthesis constraints on scalar-tensor theories of gravity. *Phys. Rev.*, D73:083525, 2006. doi: 10.1103/PhysRevD.73.083525.

[23] Justin Khoury and Amanda Weltman. Chameleon fields: Awaiting surprises for tests of gravity in space. *Phys. Rev. Lett.*, 93:171104, 2004. doi: 10.1103/PhysRevLett.93.171104.

[24] Justin Khoury and Amanda Weltman. Chameleon cosmology. *Phys. Rev.*, D69:044026, 2004. doi: 10.1103/PhysRevD.69.044026.

[25] Junpu Wang, Lam Hui, and Justin Khoury. No-Go Theorems for Generalized Chameleon Field Theories. *Phys. Rev. Lett.*, 109:241301, 2012. doi: 10.1103/PhysRevLett.109.241301.

[26] Paul Hamilton, Matt Jaffe, Philipp Haslinger, Quinn Simmons, Holger Müller, and Justin Khoury. Atom-interferometry constraints on dark energy. *Science*, 349:849–851, 2015. doi: 10.1126/science.aaa8883.

[27] K. Li et al. Neutron Limit on the Strongly-Coupled Chameleon Field. *Phys. Rev.*, D93(6):062001, 2016. doi: 10.1103/PhysRevD.93.062001.

[28] H. Lemmel, Ph. Brax, A. N. Ivanov, T. Jenke, G. Pignol, M. Pitschmann, T. Potocar, M. Wellenzohn, M. Zawisky, and H. Abele. Neutron Interferometry constrains dark energy chameleon fields. *Phys. Lett.*, B743:310–314, 2015. doi: 10.1016/j.physletb.2015.02.063.

[29] Alexander D. Rider, David C. Moore, Charles P. Blakemore, Maxime Louis, Marie Lu, and Giorgio Gratta. Search for Screened Interactions Associated with Dark Energy Below the 100 μm Length Scale. *Phys. Rev. Lett.*, 117(10):101101, 2016. doi: 10.1103/PhysRevLett.117.101101.

[30] Attaallah Almasi, Philippe Brax, Davide Iannuzzi, and René I. P. Sedmik. Force sensor for chameleon and Casimir force experiments with parallel-plate configuration. *Phys. Rev.*, D91(10):102002, 2015. doi: 10.1103/PhysRevD.91.102002.

[31] Clare Burrage, Edmund J. Copeland, and James A. Stevenson. A Proposed Experimental Search for Chameleons using Asymmetric Parallel Plates. *JCAP*, 1608(08):070, 2016. doi: 10.1088/1475-7516/2016/08/070.

[32] G. Rybka, M. Hotz, L. J. Rosenberg, S. J. Asztalos, G. Carosi, C. Hagmann, D. Kinion, K. van Bibber, J. Hoskins, C. Martin, P. Sikivie, D. B. Tanner, R. Bradley, and J. Clarke. Search for Chameleon Scalar Fields with the Axion Dark Matter Experiment. *Physical Review Letters*, 105(5):051801, July 2010. doi: 10.1103/PhysRevLett.105.051801.

[33] Jason H. Steffen, Amol Upadhye, Al Baumbaugh, Aaron S. Chou, Peter O. Mazur, Ray Tomlin, Amanda Weltman, and William Wester. Laboratory constraints on chameleon dark energy and power-law fields. *Phys. Rev. Lett.*, 105:261803, 2010. doi: 10.1103/PhysRevLett.105.261803.

[34] V. Anastassopoulos et al. Search for chameleons with CAST. *Phys. Lett.*, B749:172–180, 2015. doi: 10.1016/j.physletb.2015.07.049.

[35] G. Cantatore, A. Gardikiotis, D. H. H. Hoffmann, M. Karuza, Y. K. Semertzidis, and K. Zioutas. Recent Progress with the KWISP Force Sensor. In *Proceedings, 11th Patras Workshop on Axions, WIMPs and WISPs (Axion-WIMP 2015): Zaragoza, Spain, June 22-26, 2015*, 2015. URL `https://inspirehep.net/record/1399180/files/arXiv:1510.06312.pdf`.

[36] S. Baum, G. Cantatore, D. H. H. Hoffmann, M. Karuza, Y. K. Semertzidis, A. Upadhye, and K. Zioutas. Detecting solar chameleons through radiation pressure. *Phys. Lett.*, B739:167–173, 2014. doi: 10.1016/j.physletb.2014.10.055.

[37] Bhuvnesh Jain, Vinu Vikram, and Jeremy Sakstein. Astrophysical Tests of Modified Gravity: Constraints from Distance Indicators in the Nearby Universe. *Astrophys. J.*, 779:39, 2013. doi: 10.1088/0004-637X/779/1/39.

[38] Harry Wilcox et al. The XMM Cluster Survey: Testing chameleon gravity using the profiles of clusters. *Mon. Not. Roy. Astron. Soc.*, 452(2):1171–1183, 2015. doi: 10.1093/mnras/stv1366.

[39] Harry Wilcox, Robert C. Nichol, Gong-bo Zhao, David Bacon, Kazuya Koyama, and A. Kathy Romer. Simulation tests of galaxy cluster constraints on chameleon gravity. 2016. doi: 10.1093/mnras/stw1617.

[40] Philippe Brax, Carsten van de Bruck, Sebastien Clesse, Anne-Christine Davis, and Gregory Sculthorpe. Early Modified Gravity: Implications for Cosmology. *Phys. Rev.*, D89(12):123507, 2014. doi: 10.1103/PhysRevD.89.123507.

[41] Daniel Boriero, Subinoy Das, and Yvonne Y. Y. Wong. How CMB and large-scale structure constrain chameleon interacting dark energy. *JCAP*, 1507(07):033, 2015. doi: 10.1088/1475-7516/2015/07/033.

[42] Adrienne L. Erickcek, Neil Barnaby, Clare Burrage, and Zhiqi Huang. Catastrophic Consequences of Kicking the Chameleon. *Phys. Rev. Lett.*, 110:171101, 2013. doi: 10.1103/PhysRevLett.110.171101.

[43] Adrienne L. Erickcek, Neil Barnaby, Clare Burrage, and Zhiqi Huang. Chameleons in the Early Universe: Kicks, Rebounds, and Particle Production. *Phys. Rev.*, D89(8):084074, 2014. doi: 10.1103/PhysRevD.89.084074.

[44] Steven S. Gubser and Justin Khoury. Scalar self-interactions loosen constraints from fifth force searches. *Phys. Rev.*, D70:104001, 2004. doi: 10.1103/PhysRevD.70.104001.

[45] Antonio Padilla, Emma Platts, David Stefanyszyn, Anthony Walters, Amanda Weltman, and Toby Wilson. How to Avoid a Swift Kick in the Chameleons. *JCAP*, 1603(03):058, 2016. doi: 10.1088/1475-7516/2016/03/058.

[46] Gianfranco Bertone and Dan Hooper. History of dark matter. *Rev. Mod. Phys.*, 90(4):045002, 2018. doi: 10.1103/RevModPhys.90.045002.

[47] D. S. Akerib et al. Results of a Search for Sub-GeV Dark Matter Using 2013 LUX Data. *Phys. Rev. Lett.*, 122(13):131301, 2019. doi: 10.1103/PhysRevLett.122.131301.

[48] E. Aprile et al. Dark Matter Search Results from a One Ton-Year Exposure of XENON1T. *Phys. Rev. Lett.*, 121(11):111302, 2018. doi: 10.1103/PhysRevLett.121.111302.

[49] Xiangyi Cui et al. Dark Matter Results From 54-Ton-Day Exposure of PandaX-II Experiment. *Phys. Rev. Lett.*, 119(18):181302, 2017. doi: 10.1103/PhysRevLett.119.181302.

[50] Alejandro Ibarra, Anna S. Lamperstorfer, and Joseph Silk. Dark matter annihilations and decays after the AMS-02 positron measurements. *Phys. Rev.*, D89(6):063539, 2014. doi: 10.1103/PhysRevD.89.063539.

[51] M. Ackermann et al. Limits on Dark Matter Annihilation Signals from the Fermi LAT 4-year Measurement of the Isotropic Gamma-Ray Background. *JCAP*, 1509:008, 2015. doi: 10.1088/1475-7516/2015/09/008.

[52] M. Ackermann et al. Searching for Dark Matter Annihilation from Milky Way Dwarf Spheroidal Galaxies with Six Years of Fermi Large Area Telescope Data. *Phys. Rev. Lett.*, 115(23):231301, 2015. doi: 10.1103/PhysRevLett.115.231301.

[53] Wei Liu, Xiao-Jun Bi, Su-Jie Lin, and Peng-Fei Yin. Constraints on dark matter annihilation and decay from the isotropic gamma-ray background. *Chin. Phys.*, C41(4):045104, 2017. doi: 10.1088/1674-1137/41/4/045104.

[54] A. Albert et al. Searching for Dark Matter Annihilation in Recently Discovered Milky Way Satellites with Fermi-LAT. *Astrophys. J.*, 834(2):110, 2017. doi: 10.3847/1538-4357/834/2/110.

[55] M. Ackermann et al. The Fermi Galactic Center GeV Excess and Implications for Dark Matter. *Astrophys. J.*, 840(1):43, 2017. doi: 10.3847/1538-4357/aa6cab.

[56] Steen Hannestad. What is the lowest possible reheating temperature? *Phys. Rev.*, D70:043506, 2004. doi: 10.1103/PhysRevD.70.043506.

[57] M. Kawasaki, Kazunori Kohri, and Naoshi Sugiyama. MeV scale reheating temperature and thermalization of neutrino background. *Phys. Rev.*, D62:023506, 2000. doi: 10.1103/PhysRevD.62.023506.

[58] Kazuhide Ichikawa, Masahiro Kawasaki, and Fuminobu Takahashi. Constraint on the Effective Number of Neutrino Species from the WMAP and SDSS LRG Power Spectra. *JCAP*, 0705:007, 2007. doi: 10.1088/1475-7516/2007/05/007.

[59] Lev Kofman, Andrei D. Linde, and Alexei A. Starobinsky. Towards the theory of reheating after inflation. *Phys. Rev.*, D56:3258–3295, 1997. doi: 10.1103/PhysRevD.56.3258.

[60] Rouzbeh Allahverdi, Robert Brandenberger, Francis-Yan Cyr-Racine, and Anupam Mazumdar. Reheating in Inflationary Cosmology: Theory and Applications. *Ann. Rev. Nucl. Part. Sci.*, 60:27–51, 2010. doi: 10.1146/annurev.nucl.012809.104511.

[61] M. S. Turner. *Phys. Rev.*, D28:1243, 1983.

[62] G.D. Coughlan, W. Fischler, Edward W. Kolb, S. Raby, and G.G. Ross. Cosmological problems for the polonyi potential. *Physics Letters B*, 131(1):59 – 64, 1983. ISSN 0370-2693. doi: https://doi.org/10.1016/0370-2693(83)91091-2. URL http://www.sciencedirect.com/science/article/pii/0370269383910912.

[63] B. de Carlos, J. A. Casas, F. Quevedo, and E. Roulet. Model independent properties and cosmological implications of the dilaton and moduli sectors of 4-d strings. *Phys. Lett.*, B318:447–456, 1993. doi: 10.1016/0370-2693(93)91538-X.

[64] Tom Banks, David B. Kaplan, and Ann E. Nelson. Cosmological implications of dynamical supersymmetry breaking. *Phys. Rev.*, D49:779–787, 1994. doi: 10.1103/PhysRevD.49.779.

[65] Tom Banks, M. Berkooz, and P. J. Steinhardt. The Cosmological moduli problem, supersymmetry breaking, and stability in postinflationary cosmology. *Phys. Rev.*, D52:705–716, 1995. doi: 10.1103/PhysRevD.52.705.

[66] Tom Banks, M. Berkooz, S. H. Shenker, Gregory W. Moore, and P. J. Steinhardt. Modular cosmology. *Phys. Rev.*, D52:3548–3562, 1995. doi: 10.1103/PhysRevD.52.3548.

[67] Bobby Samir Acharya, Gordon Kane, and Eric Kuflik. Bounds on scalar masses in theories of moduli stabilization. *Int. J. Mod. Phys.*, A29:1450073, 2014. doi: 10.1142/S0217751X14500730.

[68] John T. Giblin, Gordon Kane, Eva Nesbit, Scott Watson, and Yue Zhao. Was the Universe Actually Radiation Dominated Prior to Nucleosynthesis? *Phys. Rev.*, D96(4):043525, 2017. doi: 10.1103/PhysRevD.96.043525.

[69] Gordon Kane, Kuver Sinha, and Scott Watson. Cosmological Moduli and the Post-Inflationary Universe: A Critical Review. *Int. J. Mod. Phys.*, D24(08):1530022, 2015. doi: 10.1142/S0218271815300220.

[70] Yue Zhang. Long-lived Light Mediator to Dark Matter and Primordial Small Scale Spectrum. *JCAP*, 1505(05):008, 2015. doi: 10.1088/1475-7516/2015/05/008.

[71] Asher Berlin, Dan Hooper, and Gordan Krnjaic. PeV-Scale Dark Matter as a Thermal Relic of a Decoupled Sector. *Phys. Lett.*, B760:106–111, 2016. doi: 10.1016/j.physletb.2016.06.037.

[72] Asher Berlin, Dan Hooper, and Gordan Krnjaic. Thermal Dark Matter From A Highly Decoupled Sector. *Phys. Rev.*, D94(9):095019, 2016. doi: 10.1103/PhysRevD.94.095019.

[73] Jeff A. Dror, Eric Kuflik, Brandon Melcher, and Scott Watson. Concentrated dark matter: Enhanced small-scale structure from codecaying dark matter. *Phys. Rev.*, D97(6):063524, 2018. doi: 10.1103/PhysRevD.97.063524.

[74] Tommi Tenkanen and Ville Vaskonen. Reheating the Standard Model from a hidden sector. *Phys. Rev.*, D94(8):083516, 2016. doi: 10.1103/PhysRevD.94.083516.

[75] Tommi Tenkanen. Standard model Higgs field and hidden sector cosmology. *Phys. Rev.*, D100(8):083515, 2019. doi: 10.1103/PhysRevD.100.083515.

[76] Daniel J. H. Chung, Edward W. Kolb, and Antonio Riotto. Production of massive particles during reheating. *Phys. Rev.*, D60:063504, 1999. doi: 10.1103/PhysRevD.60.063504.

[77] Gian Francesco Giudice, Edward W. Kolb, and Antonio Riotto. Largest temperature of the radiation era and its cosmological implications. *Phys. Rev.*, D64:023508, 2001. doi: 10.1103/PhysRevD.64.023508.

[78] N. Fornengo, A. Riotto, and S. Scopel. Supersymmetric dark matter and the reheating temperature of the universe. *Phys. Rev.*, D67:023514, 2003. doi: 10.1103/PhysRevD.67.023514.

[79] C. Pallis. Massive particle decay and cold dark matter abundance. *Astropart. Phys.*, 21:689–702, 2004. doi: 10.1016/j.astropartphys.2004.05.006.

[80] Graciela Gelmini, Paolo Gondolo, Adrian Soldatenko, and Carlos E. Yaguna. The Effect of a late decaying scalar on the neutralino relic density. *Phys. Rev.*, D74:083514, 2006. doi: 10.1103/PhysRevD.74.083514.

[81] Graciela B. Gelmini and Paolo Gondolo. Neutralino with the right cold dark matter abundance in (almost) any supersymmetric model. *Phys. Rev.*, D74:023510, 2006. doi: 10.1103/PhysRevD.74.023510.

[82] Leszek Roszkowski, Sebastian Trojanowski, and Krzysztof Turzyński. Neutralino and gravitino dark matter with low reheating temperature. *JHEP*, 11:146, 2014. doi: 10.1007/JHEP11(2014)146.

[83] Marco Drewes. On finite density effects on cosmic reheating and moduli decay and implications for Dark Matter production. *JCAP*, 1411(11):020, 2014. doi: 10.1088/1475-7516/2014/11/020.

[84] Gordon L. Kane, Piyush Kumar, Brent D. Nelson, and Bob Zheng. Dark matter production mechanisms with a nonthermal cosmological history: A classification. *Phys. Rev.*, D93(6):063527, 2016. doi: 10.1103/PhysRevD.93.063527.

[85] Manuel Drees and Fazlollah Hajkarim. Dark Matter Production in an Early Matter Dominated Era. *JCAP*, 1802(02):057, 2018. doi: 10.1088/1475-7516/2018/02/057.

[86] Debaprasad Maity and Pankaj Saha. Connecting CMB anisotropy and cold dark matter phenomenology via reheating. *Phys. Rev.*, D98(10):103525, 2018. doi: 10.1103/PhysRevD.98.103525.

[87] Debaprasad Maity and Pankaj Saha. CMB constraints on dark matter phenomenology via reheating in Minimal plateau inflation. *Phys. Dark Univ.*, 25:100317, 2019. doi: 10.1016/j.dark.2019.100317.

[88] Nicolás Bernal, Catarina Cosme, and Tommi Tenkanen. Phenomenology of Self-Interacting Dark Matter in a Matter-Dominated Universe. *Eur. Phys. J.*, C79(2):99, 2019. doi: 10.1140/epjc/s10052-019-6608-8.

[89] Nicolás Bernal, Catarina Cosme, Tommi Tenkanen, and Ville Vaskonen. Scalar singlet dark matter in non-standard cosmologies. *Eur. Phys. J.*, C79(1):30, 2019. doi: 10.1140/epjc/s10052-019-6550-9.

[90] Manuel Drees and Fazlollah Hajkarim. Neutralino Dark Matter in Scenarios with Early Matter Domination. *JHEP*, 12:042, 2018. doi: 10.1007/JHEP12(2018)042.

[91] Debtosh Chowdhury, Emilian Dudas, Maíra Dutra, and Yann Mambrini. Moduli Portal Dark Matter. *Phys. Rev.*, D99(9):095028, 2019. doi: 10.1103/PhysRevD.99.095028.

[92] Alessandro Di Marco, Gianfranco Pradisi, and Paolo Cabella. Inflationary scale, reheating scale, and pre-BBN cosmology with scalar fields. *Phys. Rev.*, D98(12):123511, 2018. doi: 10.1103/PhysRevD.98.123511.

[93] JiJi Fan and Matthew Reece. In Wino Veritas? Indirect Searches Shed Light on Neutralino Dark Matter. *JHEP*, 10:124, 2013. doi: 10.1007/JHEP10(2013)124.

[94] Timothy Cohen, Mariangela Lisanti, Aaron Pierce, and Tracy R. Slatyer. Wino Dark Matter Under Siege. *JCAP*, 1310:061, 2013. doi: 10.1088/1475-7516/2013/10/061.

[95] Adrienne L. Erickcek and Kris Sigurdson. Reheating Effects in the Matter Power Spectrum and Implications for Substructure. *Phys. Rev.*, D84:083503, 2011. doi: 10.1103/PhysRevD.84.083503.

[96] JiJi Fan, Ogan Özsoy, and Scott Watson. Nonthermal histories and implications for structure formation. *Phys. Rev.*, D90(4):043536, 2014. doi: 10.1103/PhysRevD.90.043536.

[97] Adrienne L. Erickcek. The Dark Matter Annihilation Boost from Low-Temperature Reheating. *Phys. Rev.*, D92(10):103505, 2015. doi: 10.1103/PhysRevD.92.103505.

[98] Adrienne L. Erickcek, Kuver Sinha, and Scott Watson. Bringing Isolated Dark Matter Out of Isolation: Late-time Reheating and Indirect Detection. *Phys. Rev.*, D94(6):063502, 2016. doi: 10.1103/PhysRevD.94.063502.

[99] Carlos Blanco, M. Sten Delos, Adrienne L. Erickcek, and Dan Hooper. Annihilation Signatures of Hidden Sector Dark Matter Within Early-Forming Microhalos. 2019.

[100] Matteo Viel, George D. Becker, James S. Bolton, and Martin G. Haehnelt. Warm dark matter as a solution to the small scale crisis: New constraints from high redshift Lyman-α forest data. *Phys. Rev.*, D88:043502, 2013. doi: 10.1103/PhysRevD.88.043502.

[101] Julien Baur, Nathalie Palanque-Delabrouille, Christophe Yèche, Christophe Magneville, and Matteo Viel. Lyman-alpha Forests cool Warm Dark Matter. *JCAP*, 1608(08):012, 2016. doi: 10.1088/1475-7516/2016/08/012.

[102] Vid Iršič et al. New Constraints on the free-streaming of warm dark matter from intermediate and small scale Lyman-α forest data. *Phys. Rev.*, D96(2):023522, 2017. doi: 10.1103/PhysRevD.96.023522.

[103] Ethan O. Nadler, Vera Gluscevic, Kimberly K. Boddy, and Risa H. Wechsler. Constraints on Dark Matter Microphysics from the Milky Way Satellite Population. *Astrophys. J.*, 878(2):L32, 2019. doi: 10.3847/2041-8213/ab1eb2. [Astrophys. J. Lett.878,32(2019)].

[104] Philippe Brax, Carsten van de Bruck, Anne-Christine Davis, Justin Khoury, and Amanda Weltman. Detecting dark energy in orbit - The Cosmological chameleon. *Phys. Rev.*, D70:123518, 2004. doi: 10.1103/PhysRevD.70.123518.

[105] David F. Mota and Camilla A. O. Schelpe. Evolution of the Chameleon Scalar Field in the Early Universe. *Phys. Rev.*, D86:123002, 2012. doi: 10.1103/PhysRevD.86.123002.

[106] Amol Upadhye, Wayne Hu, and Justin Khoury. Quantum Stability of Chameleon Field Theories. *Phys. Rev. Lett.*, 109:041301, 2012. doi: 10.1103/PhysRevLett.109.041301.

[107] E. G. Adelberger, Blayne R. Heckel, Seth A. Hoedl, C. D. Hoyle, D. J. Kapner, and A. Upadhye. Particle Physics Implications of a Recent Test of the Gravitational Inverse Sqaure Law. *Phys. Rev. Lett.*, 98:131104, 2007. doi: 10.1103/PhysRevLett.98.131104.

[108] Robert R. Caldwell and Steven S. Gubser. Brief history of curvature. *Phys. Rev.*, D87(6):063523, 2013. doi: 10.1103/PhysRevD.87.063523.

[109] N. D. Birrell and P. C. W. Davies. *Quantum Fields in Curved Space*. Cambridge Monographs on Mathematical Physics. Cambridge University Press, 1984.

[110] Karsten Jedamzik, Martin Lemoine, and Jerome Martin. Collapse of Small-Scale Density Perturbations during Preheating in Single Field Inflation. *JCAP*, 1009:034, 2010. doi: 10.1088/1475-7516/2010/09/034.

[111] Richard Easther, Raphael Flauger, and James B. Gilmore. Delayed Reheating and the Breakdown of Coherent Oscillations. *JCAP*, 1104:027, 2011. doi: 10.1088/1475-7516/2011/04/027.

[112] Gordon Blackadder and Savvas M. Koushiappas. Dark matter with two- and many-body decays and supernovae type Ia. *Phys. Rev.*, D90(10):103527, 2014. doi: 10.1103/PhysRevD.90.103527.

[113] Cyril Pitrou, Alain Coc, Jean-Philippe Uzan, and Elisabeth Vangioni. Precision big bang nucleosynthesis with improved Helium-4 predictions. *Phys. Rept.*, 754:1–66, 2018. doi: 10.1016/j.physrep.2018.04.005.

[114] Alexey Boyarsky, Julien Lesgourgues, Oleg Ruchayskiy, and Matteo Viel. Lyman-alpha constraints on warm and on warm-plus-cold dark matter models. *JCAP*, 0905:012, 2009. doi: 10.1088/1475-7516/2009/05/012.

[115] Julien Lesgourgues and Thomas Tram. The Cosmic Linear Anisotropy Solving System (CLASS) IV: efficient implementation of non-cold relics. *JCAP*, 1109:032, 2011. doi: 10.1088/1475-7516/2011/09/032.

[116] Riccardo Murgia, Alexander Merle, Matteo Viel, Maximilian Totzauer, and Aurel Schneider. "Non-cold" dark matter at small scales: a general approach. *JCAP*, 1711:046, 2017. doi: 10.1088/1475-7516/2017/11/046.

[117] Riccardo Murgia, Vid Iršič, and Matteo Viel. Novel constraints on noncold, nonthermal dark matter from Lyman-α forest data. *Phys. Rev.*, D98(8):083540, 2018. doi: 10.1103/PhysRevD.98.083540.

[118] Aurel Schneider, Robert E. Smith, Andrea V. Macciò, and Ben Moore. Non-linear evolution of cosmological structures in warm dark matter models. *MNRAS*, 424(1):684–698, Jul 2012. doi: 10.1111/j.1365-2966.2012.21252.x.

[119] Matteo Viel, George D. Becker, James S. Bolton, and Martin G. Haehnelt. Warm dark matter as a solution to the small scale crisis: New constraints from high redshift Lyman-α forest data. *Phys. Rev.*, D88:043502, 2013. doi: 10.1103/PhysRevD.88.043502.

[120] Maria Archidiacono, Deanna C. Hooper, Riccardo Murgia, Sebastian Bohr, Julien Lesgourgues, and Matteo Viel. Constraining Dark Matter-Dark Radiation interactions with CMB, BAO, and Lyman-α. *JCAP*, 1910(10):055, 2019. doi: 10.1088/1475-7516/2019/10/055.

[121] Riccardo Murgia, Giulio Scelfo, Matteo Viel, and Alvise Raccanelli. Lyman-α forest constraints on Primordial Black Holes as Dark Matter. *Phys. Rev. Lett.*, 123(7):071102, 2019. doi: 10.1103/PhysRevLett.123.071102.

[122] Mark R. Lovell, Carlos S. Frenk, Vincent R. Eke, Adrian Jenkins, Liang Gao, and Tom Theuns. The properties of warm dark matter haloes. *Mon. Not. Roy. Astron. Soc.*, 439:300–317, 2014. doi: 10.1093/mnras/stt2431.

[123] Torsten Bringmann and Stefan Hofmann. Thermal decoupling of WIMPs from first principles. *JCAP*, 0704:016, 2007. doi: 10.1088/1475-7516/2007/04/016,10.1088/1475-7516/2016/03/E02. [Erratum: JCAP1603,no.03,E02(2016)].